Evidence for deliberate burial of the dead by *Homo naledi*

Lee R Berger[1,2,3]*,Tebogo Makhubela[2,4]*, Keneiloe Molopyane[2], Ashley Krüger[5], Patrick Randolph-Quinney[2,6], Marina Elliott, [2,7], Becca Peixotto[2,8], Agustín Fuentes[9], Paul Tafforeau[10], Vincent Beyrand[2,10], Kathleen Dollman[10], Zubair Jinnah[2,11], Angharad Brewer Gillham[12], Kenneth Broad[13], Juliet Brophy[2, 14], Gideon Chinamatira[15], Paul H. M. Dirks[2,16], Elen Feuerriegel[2,17], Alia Gurtov[18], Nompumelelo Hlophe[19], Lindsay Hunter[20], Rick Hunter[2], Kudakwashe Jakata[15], Corey Jaskolski[21], Hannah Morris[2,22], Ellie Pryor[23], Maropeng Ramaphela[2], Eric Roberts[2,15], Jacqueline S. Smilg[2], Mathabela Tsikoane[2], Steven Tucker[2], Dirk van Rooyen[2], Kerryn Warren[24], Colin D. Wren[25], Marc Kissel[26], Penny Spikins[27], John Hawks[2,18]*

[1]The National Geographic Society, 1145 17th St NW, Washington DC, 20036

[2]Centre for the Exploration of the Deep Human Journey, School of Anatomical Sciences, University of the Witwatersrand; Private Bag 3, Wits 2050, South Africa

[3] The Carnegie Institution for Science, 5241 Broad Branch Road NW Washington D.C. 20015

[4]Department of Geology, University of Johannesburg, Johannesburg, PO Box 524, Auckland Park, 2006

[5]Department of Palaeobiology, Swedish Museum of Natural History, Box 50007, SE-104 05, Stockholm, Sweden

[6] Department of Applied Sciences, Faculty of Health and Life Sciences, Northumbria University, UK

[7]Department of Archaeology, Simon Fraser University, 8888 University Drive, Burnaby, BC, V5A 1S6, Canada

[8]The American University, 4400 Massachusetts Ave NW, Washington, D.C., DC 20016, USA

[9]Department of Anthropology, Princeton University; 123 Aaron Burr Hall, Princeton USA 08455

[10]European Synchrotron Radiation Facility, 71 Avenue des Martyrs, CS-40220 38043 Grenoble cedex 09, France

[11]School of GeoSciences, University of the Witwatersrand, Private Bag 3, Wits 2050, South Africa

[12]Frontiers Media Limited, New Broad Street House, 35 New Broad St, London EC2M 1NH, United Kingdom

[13]Rosenstiel School of Marine, Atmospheric, and Earth Science, 4600 Rickenbacker Causeway Miami, FL 33149

[14]Department of Geography and Anthropology, Louisiana State University, Baton Rouge, LA 70803, USA

[15]Evolutionary Studies Institute, University of the Witwatersrand, Private Bag 3, Wits 2050, South Africa

[16]Department of Geoscience, James Cook University, Townsville, Qld 4811, Australia

[17]Primate Evolutionary Biomechanics Laboratory, Department of Anthropology, Box 353100, University of Washington, Seattle, WA 98195-3100, USA

[18]Department of Anthropology, University of Wisconsin-Madison, Madison, WI 53593, USA

[19]Department of Anthropology, 4352 TAMU College Station, TX 77843-4352, USA

[20]Center for Academic Research & Training in Anthropogeny, UC San Diego, 9500 Gilman Drive #0140, La Jolla, CA 92093-0140, USA

[21]Synthetaic, 1309 Milwaukee St, Delafield, WI, USA

[22]ICON & Warnell School of Forestry, University of Georgia, Athens, GA 30602, USA

[23]School of Earth and Environmental Sciences, Main Building, Park Place, Cardiff**,** CF10 3AT, United Kingdom

[24]Human Evolution Research Institute, 3rd Floor Beattie Building, University of Cape Town, Cape Town, South Africa

[25]Department of Anthropology, University of Colorado Colorado Springs; Colorado Springs, 80918, USA

[26]Department of Anthropology, Appalachian State University; 348 Anne Belk Hall 224

Boone, NC, USA 28608

[27]Department of Archaeology, University of York; The King's Manor, York, UK, YO1 7EP

* Corresponding Authors

Abstract

Recent excavations in the Rising Star Cave System of South Africa have revealed burials of the extinct hominin species *Homo naledi*. A combination of geological and

anatomical evidence shows that hominins dug holes that disrupted the subsurface stratigraphy and interred the remains of *H. naledi* individuals, resulting in at least two discrete features within the Dinaledi Chamber and the Hill Antechamber. These are the most ancient interments yet recorded in the hominin record, earlier than evidence of *Homo sapiens* interments by at least 100,000 years. These interments along with other evidence suggest that diverse mortuary practices may have been conducted by *H. naledi* within the cave system. These discoveries show that mortuary practices were not limited to *H. sapiens* or other hominins with large brain sizes.

Introduction

Burials have been recognized in the archaeological record as pits within the earth that were intentionally dug to inter the remains of the dead (Pearson, 1999; Pettitt and Anderson, 2020). Burials are one of many kinds of mortuary practices, which are diverse across human societies and have meanings and functions that are in many cases related to their forms (Metcalf and Huntington, 1991; Robben, 1991). Late Pleistocene modern humans and Neandertals had varied mortuary practices including burials. They interred bodies within anthropogenic pits, natural depressions, and rock niches, in varied postures, sometimes alone and sometimes with multiple bodies together (Martinón-Torres et al., 2021; Tillier, 2022; Maureille, 2022).

It can be challenging to test whether ancient remains were part of a burial due to the varied forms of burials and subsequent diagenesis of sediments. The oldest known human burial in Africa was at Panga ya Saidi cave in Kenya, dating back to 78.3 ± 4.1 ka, where the partial skeleton of a child was intentionally buried in a pit dug within the earth, with precise

articulation and excellent anatomical association of skeletal elements indicating *in-situ* decomposition of the body (Martinón-Torres et al., 2021). In that case the burial pit was delimited, and the burial fill mixture of ferruginous silt and sand was found to be different from the sediment layer where the pit was excavated, but similar to the two overlying layers (Martinón-Torres et al., 2021).

Here we describe burials from the Rising Star cave system (Berger et al., 2015; Dirks et al., 2015; Fig. 1) containing bodies of *Homo naledi* individuals. We uncovered and partially excavated two delimited burial features on the floor of the Dinaledi Chamber (Dirks et al., 2015; Fig. 1) and extracted *en bloc* a delimited burial feature from the floor of the Hill Antechamber (Elliott et al., 2021; Fig. 1). Analysis of the stratigraphy, textures, geochemical composition and granulometry of the sediments around and within the burial features on the Dinaledi Chamber floor suggests that the two burials occur in pits that were intentionally dug.

Results

Dinaledi Feature 1

The Dinaledi Feature 1 (Figs. 2 & 3) was uncovered in 2018 in an excavation unit within the Dinaledi Chamber immediately to the north of our 2013–2014 excavation area that produced abundant skeletal remains of *H. naledi* (Fig. 4). Within this new excavation, at a depth of 8 cm, a concentration of bones and accompanying soil disturbance forms a roughly oval-shaped distribution. On three sides away from the earlier excavation, this oval is clearly delimited from surrounding sediment in which few small bone fragments occur. On the fourth side, the space between this feature and the earlier excavation area included three long bone fragments. The feature measures approximately 50 cm in total length and 25 cm in breadth

(Fig. 1). This area of the chamber floor has a slope of ~11 degrees from magnetic North to South, and the feature itself is on a horizontal level beneath this sloping surface. We excavated 108 skeletal specimens from directly above or within the feature as we exposed its horizontal extent; all are anatomically consistent with *H. naledi* (SI 2.1). During this excavation, we recognized that the developing evidence was suggestive of a burial, due to the spatial configuration of the feature and the evidence that the excavated material seemed to come from a single body. We halted further excavation and left the feature with identifiable skeletal remains in place across its surface. At the southernmost extent of the feature, we excavated a profile that reveals a remaining depth of skeletal material of 3cm in this location; we do not know whether this depth is consistent across the remainder of the feature.

A combination of stratigraphic, anatomical, and taphonomic evidence supports this feature as a burial. The key observations are (1) the difference in sediment composition within the feature compared to surrounding sediment; (2) the disruption of stratigraphy; (3) the anatomical coherence of the skeletal remains; (4) the matrix-supported position of some skeletal elements; and (5) the compatibility of non-articulated material with decomposition and subsequent collapse.

The feature intrudes into the unlithified mud clast breccia (Fig. 3a-c, Supplementary Table 1) of sub-unit 3b deposits, the fossil-bearing sub-unit in the Dinaledi Chamber (Dirks et al., 2017; Wiersma et al., 2020; Robbins et al., 2021). The angular mud clasts found in this subunit are fragments of the laminated orange-red mud facies from Unit 1 deposits (Fig. 3d) (Wiersma et al., 2020). These angular mud clasts were incorporated into the unlithified mud clast breccia in a mostly chaotic and unstructured way, without any observable microstratigraphy (Fig. 3c). However, the abundance of laminated orange-red mud clasts with grain sizes >2 cm around Feature 1 seems to be related to a laterally continuous layer where

these clasts emanate (Fig. 3b). This layer was not noted during our previous excavations where the clasts were reported (Dirks et al., 2015, 2017), but it is continuous in the profile immediately to the east of the feature; it is disrupted in the sediment profile at the southern extent of the feature (Fig. 3b). Some orange-red clasts are visible within the exposed south face of the feature and isolated clasts occur within the feature itself. We carried out petrographic analysis of sediment from within the feature as well as surrounding it and compared with sediments from other parts of the Rising Star cave (SI 1). The bulk chemistry results of the sediments were evaluated using principal components analysis (PCA). The PCA yields three principal components (Fig. 5). Principal component 1 (PC1) explains 51% of the total variation in the major element chemistry with a dominance in the positive axis of Ti, Al, K and Ba vs Ca and Mg in the negative direction (Figs. 5 and 6). The dominance of Al and K is consistent with the clay-rich mudstone sediments across the Rising Star cave (Dirks et al., 2015, 2017; Wiersma et al., 2020). Sediments in the Lesedi chamber and other areas in the Dinaledi Subsystem have higher negative loadings in PC1 indicating more calcite cementation whereas sediments from the Dinaledi Chamber do not exhibit pronounced negative loadings (Ca and Mg) in PC1 which supports their uncalcified nature (Fig. 6). PC2 describes only 8% variability with a dominance of Si, P and S in the positive direction vs all other elements, but mainly Mn and Fe in the negative axis (Figs. 5 and 7). PC2 distinctly delineates fossil-bearing sediments from sterile sediments based on the positive loadings of P and S, which we assume to be proxies of the fossil bones (Fig. 7). For example, around the Dinaledi Feature 1, PC2 shows that the floor sediment collected during the excavation that uncovered the feature has sterile areas with no positive loadings of P and S, and fossil-bearing areas have positive loadings of P and S (Figs. 3 and 7). While different from surrounding sediment on PC2, the infill of the feature resembles the composition of other parts of the Dinaledi Subsystem and Lesedi Chamber where remains of *H. naledi* have been

unearthed (Fig. 7). Sediments around the feature known to be sterile (group SA samples, Figure S1a) do not show convincing positive loadings of P and S, but sediments inside and below the feature (group SB and SE samples, Figure S1) as well as between Features 1 and 2 (group SC samples) show convincing positive loadings of P and S. PC3 also explains 8% variability with dominance of Mn, Na, Ba, Fe and Si in the positive domain vs mainly Ti, Al, Ca, Mg and K in the negative direction (Figs. 5 and 8). The PC3 positive loadings seem to be indicators of secondary processes that promote the breakdown of LORM to form UMCB. This is based on the pervasive deposition of Mn and Fe as Mn-Fe-oxihydroxide by microbial activity during the autochthonous transformation of LORM to UMCB (Wiersma et al., 2020).

The skeletal representation and spatial relationship of elements indicate that Feature 1 contains predominantly the remains of a single body including the eighty-three identifiable bone fragments and teeth that we recovered above and within the exposed circumference of the feature. Some of these were in direct contact with underlying fossil material, while others were above the feature separated by up to 5 cm of sediment. The excavated hominin remains (SI 2.1) include a fragmentary adult left hemi-mandible with associated dentition, partial adult right femur, fragments of both left and right humeri, left and right ulnae, left and right radii, vertebral and rib fragments, ischium fragment, and some cranial fragments. Three of the fragments that we excavated directly above and in contact with Feature 1 represent two elements of at least one additional individual: an immature proximal right femur and shaft fragment compatible with an immature femur, and a fragment of an immature proximal left humerus. Although some skeletal material is obscured by sediment, many elements remaining within the unexcavated portion of the feature are identifiable (Fig. 1d, Fig. 9). None of the visible material duplicates elements already recovered from the feature. Fragments of a right hemi-mandible are present that are consistent with the excavated left hemi-mandible. Much

of a cranial vault is also present. Some elements visible on the surface of Feature 1 are in articulation and most are near related anatomical elements (Fig. 9; see Materials and Methods).

The spatial arrangement of the skeletal remains is consistent with primary burial of a fleshed body, covered in sediment, followed by decomposition and post-depositional collapse. Some elements remain in a vertical or sub-vertical orientation reflective of decomposition with matrix support (Bolter et al., 2018). Such matrix-supported elements predominantly occur near the edge of the feature. A portion of ribcage is visible with some ribs oriented near vertical, others broken and collapsing along a craniocaudal axis, all apparently constrained by matrix support along the edge of the feature (Fig. 1d). Near the south end of the feature, cranial fragments are supported by matrix in sub-vertical orientations (Fig. 1d; Fig. 9). The decompositional collapse of the structures making up the thorax and pelvis, and void-space resulting from this and the decomposition of the soft tissues, would have brought overlying sediment into spaces. This process may have allowed the extraneous bone fragments from at least one other individual into the feature from overlying sediment. We also cannot exclude that some physical disturbance may have resulted from *H. naledi* activity within the chamber subsequent to the burial, such as digging nearby burials, or trampling. Such disturbance may also explain the breakage and spatial displacement of the two halves of the mandible.

The decomposition and dissociation of this body are consistent with an original burial environment substantially like the current sedimentary conditions in the chamber (Dirks et al., 2015). The feature includes angular laminated orange-red mud clasts that are inconsistent with saturation of the sediment by water after interment (Dirks et al., 2015, 2017; Wiersma et al., 2020). Without a water-saturated environment, the decomposition of soft tissue resulted in

voids, into which the bones comprising anatomical units (head, torso, limbs) could collapse, resulting in displacement of fragments and joint articulations. By contrast, the decomposition of a body within a natural depression on the cave floor results in a different pattern of displacement. The matrix-supported elements at the edges of this burial, the evidence of disruption of the laminated orange-red mud clast layer, and the inclusion of mud clasts within the skeletal remains are also consistent with deposition of the body within a pit dug by *Homo naledi* and covered rather than exposed upon the cave floor within a natural depression.

At the western extreme of the excavation unit containing Dinaledi Feature 1, a second concentration of bone is visible, which we have designated Dinaledi Feature 2 (Fig. 1), separated from Dinaledi Feature 1 by approximately 20 cm of sterile soil. This feature enters the west wall of the excavation unit and we do not know its full extent. The small number of elements recovered from Feature 2 are compatible with a single individual being present and its visible form is consistent with that described for Feature 1. We have left Feature 2 otherwise undisturbed for future investigation.

Hill Antechamber Feature

The Hill Antechamber feature was uncovered during excavations conducted in 2017. The excavations were of a debris cone situated in the northeast part of the chamber, near the base of the vertical entrance (termed “the Chute”) used by our team to access the Dinaledi Subsystem (Fig. 10). At a depth 20 cm below datum, and 5 cm below the sloping surface, the team encountered a localized accumulation of bone fragments and skeletal elements across a roughly triangular space some 38 cm by 48 cm. Due to the fragile state of the material, the team excavated around the edges of this bone concentration, pillaring it to a depth of

approximately 20 cm. To remove it safely through the Chute, the team separated the feature into one larger and two smaller subsections, each of which was encased within a plaster jacket for removal. The two smaller subsections were scanned on a micro-computed tomography (micro-CT) scanner (see Materials and Methods). The largest subsection was too large for this micro-CT unit and so we obtained a clinical CT scan of this specimen with 0.5 mm voxel size (see Materials and Methods).

From the CT scans of the feature, we identified a minimum of 90 skeletal elements and 51 dental elements. The dental elements include at least 30 teeth from a single individual, which we have designated as Individual 1. All maxillary teeth of this individual are spatially contiguous, in correct occlusal order, and are consistent with being positioned within what was once a complete maxilla that either has degraded or does not present a contrast in density with surrounding sediment (Fig. 10). The mandibular teeth of Individual 1 are in two disjunct parts; the left mandibular dentition and right I_1, I_2, P_3, and P_4 are in correct order and *in situ* within a mandibular fragment that is approximately 1 cm from occlusion with the left maxillary dentition; the right mandibular molars are in near occlusion with the right maxillary molars, making clear that the mandible of this individual was in articulation with the skull when these teeth arrived at their current positions. The third molars of Individual 1 are partial crowns without roots consistent with a late juvenile developmental stage (Bolter et al., 2018). At least fourteen teeth represent a second late juvenile individual designated Individual 2. These teeth are localized within the feature, all within a 10-cm area, but are not in any anatomical order. The identifiable elements are all maxillary teeth. Based on the incomplete roots of the canines, premolars, and second molars, Individual 2 was a slightly younger juvenile than Individual 1, at or shortly after second molar eruption. Four additional teeth represent a third individual designated Individual 3. Individual 3's remains preserve left and

right permanent maxillary canines, a right permanent mandibular canine, and a probable mandibular incisor, all localized within an 8-cm area. Nearly translucent objects that may be developing crowns of a much younger individual are identified as probable Individual 4.

The identifiable postcranial elements in the feature are nonduplicative and consistent with a single individual. Based on the spatial distribution of the remains we deem it most likely associated with the Individual 1 skull. Many elements are in articulation or sequential anatomical position, including a substantially articulated right foot, ankle, and adjacent lower limb bones, two series of partial ribs, a partial right hand, and ulna and radius. Other elements attributable to this skeleton are in anatomical proximity; for example, most left hand elements are within a 7cm radius of each other, fragments of right tibia and fibula are adjacent to each other and the right ankle, and elements of the left foot are localized within a small radius. Elements with thin cortical bone such as vertebral bodies, tarsals, and pelvic elements are less evident in the CT data; this may either reflect a lack of density contrast with surrounding sediment or the postdepositional degradation of these elements similar to the excavated material from the Dinaledi Chamber (Dirks et al., 2015). In addition to these identifiable elements, a number of small unidentifiable diaphyses can be seen in the northwest corner of the feature; these are consistent with a young immature individual and may be attributable to Individual 4. Synchrotron scanning of these specimens is planned as part of future work.

The configuration of the skeletal remains in this feature is consistent with the body of Individual 1 being in a flexed position at the time of interment, with the right foot and right hand near or at their current spatial positions. The proximity and anatomical attitude of the left humerus, radius, and ulna, and left hand and wrist material is consistent with flexion of the left upper limb. Based on their current position, we conclude that the decomposition of muscle and integument created a void space into which the elements collapsed, with further

spatial displacement following loss of connective tissues within the joints, suggesting the limb was resting at a somewhat higher level during the early post-mortem period. Collectively, the remains of the torso and upper limbs of Individual 1 now lie in a relatively flat plane that represents their collapsed state. These are separated from the lower limb and right foot by sediment that must have been in place prior to decompositional slumping of the upper body. The absence of such a matrix layer (i.e., if the burial was configured as an open pit) would have ensured that the torso and limb groups would have settled in a single layer at the base of the cut (Mickleburgh and Wescott, 2018). Instead, the vertical separation between lower limb and upper body material is indicative of sedimentary matrix support. Decompositional slumping of the body and/or subsequent matrix compression has resulted in post-depositional fracturing visible on all identifiable rib bones. The upper limb elements exhibit multiple transverse and step fractures consistent with the effects of post-depositional matrix compression and other effects from the burial environment or our movement of the specimen. The maxillary dentition, with the mandible in or near articulation, is presently in a semi-inverted position, located above several rib shafts and near the right hand. This position is consistent with the displacement of the skull from a higher position, following decomposition of the nuchal musculature and cervical connective tissue, allowing the head to disarticulate from the axial skeleton, accompanied by rolling, inversion, and some horizontal displacement.

This feature presents clear sedimentary evidence that a pit was dug through existing stratigraphy (Fig. 10, SI 3.1). The present floor of the Hill Antechamber is a steep slope of approximately 30 degrees from the passages in the north wall toward the two narrow passageways leading to the Dinaledi Chamber. The Hill Antechamber feature was excavated at the top of this slope, near the northeast wall. As in the Dinaledi Chamber, the floor of the

Hill Antechamber is composed of subunit 3b unlithified mud clast breccia, including laminated orange-red mud clasts. The excavation profiles at the east and south edges of the feature show distinct layering of orange-red mud clasts parallel to the current chamber floor. The CT data show that these layers of clasts are interrupted within the feature; the feature exhibits two clast-rich zones. A bowl-shaped concave layer of clasts and sediment-free voids makes up the bottom of the feature. At the south end of the feature this clast layer slopes in the opposite direction as the chamber floor. The right foot and lower limb material is supported by this concave layer, sloping southwest-to-northeast approximately 15 degrees. Above the foot is additional sediment with a high density of clasts and small air pockets or voids, separating it from the upper limb and torso material. This skeletal material slopes at 10 degrees northeast-southwest, opposite the slope of the foot and leg, and different from the 30 degree slope of the chamber floor. The texture and internal stratigraphy of this sediment infill is not compatible with slow incremental deposition or the percolation of small particles around and into skeletal remains that were once exposed on the antechamber floor (Fig. 10). The combination of these lines of evidence indicates that a pit was dug into existing strata, and then a body was placed into it and buried prior to the decomposition of soft tissue.

In their current situation it is not possible to inspect the surfaces of the Hill Antechamber bones for other signs of taphonomic modification, and so we cannot rule out further involvement of hominins in the removal of the skull or disarticulation of the remains. It is worth noting that the amplitude of movement away from the original anatomical position will depend upon the position of the remains when deposited, and the available space in which any movement can take place; such spaces can be created by the decomposition of surrounding soft tissues in cases of interment in sediment, and the amplitude of movement represents the extent to which a bone can move in any of the possible directions. Primary

dispositions (especially burials) tend to place bones in a relatively stable position, and thus there will be little if any movement of individual bones or elements following the loss of soft tissue. When disposition occurs where bones are placed in an unstable position they will move in accordance with gravity and the shape of the surrounding space once soft tissue is lost (Roksandic, 2002). As such, the spatial distribution and alignment of the Hill Antechamber remains are consistent with decompositional processes taking place after their deposition into a sedimentary-filled pit feature (Mickleburgh and Wescott, 2018).

In addition to the skeletal remains, the feature contains a single stone artifact in close contact with the articulated hand and wrist material (SI 3; Figs. 11 and 12). It is emplaced within the feature at an angle of 25 degrees from horizontal in a southeast-northwest slope, in a different orientation from with any of the skeletal material or the slope of the chamber floor, and it does not rest upon the bowl-shaped bottom of the feature. We obtained a high-resolution scan of this artifact from the European Synchotron Research Facility; it is described in Supplementary Information 3.

Discussion

These burial features meet evidentiary standards used for recognizing burials of *H. sapiens* (Martinón-Torres et al., 2021). The recognition of burials in these chambers within the cave system prompts us to evaluate the broader array of *H. naledi* remains for evidence of mortuary activities. Our 2013–2014 excavation was localized between 1 and 2 meters to the southwest of Dinaledi Feature 1 (Fig. 1c). Within an excavation area of 80 cm by 80 cm we recovered remains attributable to a minimum of 5 individuals, with many elements highly fragmented and others in articulation with matrix support preserving anatomical regions (Berger et al., 2015). Our study of the spatial distribution of this material identifies

concentrations that are spatially identifiable, although with substantial commingling and loss of anatomical ordering of much of the material (Kruger, 2017) (Figs. 4 and 13). A parsimonious explanation for this configuration of skeletal remains is that these remains may be a palimpsest of burials that have sequentially disrupted each other. In this hypothesis, early burials were disturbed when pits were dug for subsequent burials. Other occurrences of remains outside of the Dinaledi Chamber and Hill Antechamber (Hawks et al., 2017; Brophy et al., 2021) are discussed as possible evidence of mortuary practices in SI 4.2. Instances where parts of individuals occur in remote narrow passages cannot be explained as a result of carnivore or water transport (Elliott et al., 2021; Brophy et al., 2021), making it necessary to consider that *H. naledi* may have placed these partial remains in these locations, possibly representing a form of funerary caching. It is possible that *H. naledi* used certain parts of the cave system for burials and other mortuary practices in contrast to other kinds of behaviors, and further exploration of the cave system may assess that hypothesis.

The existence of diverse practices in the placement or interment of individuals within the Rising Star cave system is similar to the diverse practices noted within other sites of multiple burials of *H. sapiens* including Qafzeh Cave and Skhūl Cave (Tillier, 2022). Based on current dates associated with the Dinaledi and Hill Antechamber remains of *H. naledi*, this complex treatment of the dead of *H. naledi* may pre-date the earliest evidence of burials by *H. sapiens* in Africa by as much 160,000 thousand years or more (Martinón-Torres et al., 2021). The Rising Star burials are, however, younger than the mortuary behavior by early Neandertals found at Sima de los Huesos, Spain at ~430,000 years (Sala et al., 2022; Arsuaga et al., 2014).

Some authors have argued that mortuary behavior is unlikely for *H. naledi*, due to its small brain size (Val, 2016). The evidence demonstrates that this complex cultural behavior

was not a simple function of brain size. While we cannot at this time exclude *H. naledi* as part of the ancestral makeup of humans, its overall morphology suggests that its common ancestors with today's humans and Neandertals go back a million years or more (Dembo et al., 2016; Argue et al., 2017; Caparros and Prat, 2021; Thackeray, 2015). This raises the possibility that burial or other mortuary behavior may have arisen much earlier than present evidence for them, or that such behaviors evolved convergently in minds different from our own. Understanding such behaviors will require comparative study of all hominin lineages in which they occur.

Materials and Methods

Fossil material and its location

The features and fossils described here have been found within naturally formed chambers of the Rising Star Cave System (Fig. 1), two of which are sub-chambers of the Dinaledi Subsystem known as the Hill Antechamber U.W. 107 and Dinaledi Chamber U.W. 101 (Figure S2-5) (Elliott et al., 2021). We also discuss material recovered from the Lesedi Chamber U.W. 102 (Figure S6) (Hawks et al., 2017) and a fourth locality in a remote passage of the Dinaledi Subsystem, U.W. 110 (Figure S5) (Brophy et al., 2021) in the University of the Witwatersrand's fossil locality catalogue system (Zipfel and Berger, 2009). An augmented virtual reality flythrough of the cave is provided as Movie S1 that allows a detailed examination of the Hill antechamber and Dinaledi Subsystem.

The features described here have been excavated to varying extents ranging from partial exposure to total excavation and extraction from the cave. It is important to note that once it was recognized during excavations that some of the fossil bones were contained in

discrete features that appeared to be pits dug into the floor of the cave, the decision was made to preserve a significant portion of these features for future studies. This was done in order to preserve evidence for developing additional hypotheses as well as to await the development of anticipated advances in analytical technologies. The Hill Antechamber feature is fragile and where we exposed its surface it had already experienced significant deterioration. We therefore extracted the entire feature in three parts by exposing the sediments surrounding its edges and then encasing all contents in three plaster jackets, one large and two smaller encasements. This was done so that the resulting sections would be small enough to be brought through the narrow confines of the Chute during ascent from the Hill Antechamber. This material was CT scanned and the larger block designated for synchrotron scanning. The material remains in these plaster jackets in order to protect them from the environment and allow the application of technology to examine them *in situ*.

Fossil material excavated prior to the 2017 discovery of Feature 1 in the Dinaledi Chamber were typically extracted entirely from their original context using methods described in Excavation Methods below or in papers describing these fossils (Berger et al., 2015; Dirks et al., 2015; Hawks et al., 2017; Brophy et al., 2021; Elliott et al., 2021). Images and notes for this work have either been published or are held by the University Curator of Collections at the University of the Witwatersrand, Johannesburg, South Africa. All sediments recovered from these excavations have been catalogued and preserved and are held on-site at the Rising Star site and are available for study.

The fossil remains described here, and from all previous excavations are available for study by application to the Fossil Access Committee of the University of the Witwatersrand through the Curator of Collections. 3D shape files of more identifiable material may be downloaded at https://Morphosource.org under a Creative Commons License by attribution.

Dinaledi Chamber excavation

The Dinaledi Chamber is the location of our excavations from 2013 to 2016. During the course of these excavations, our team collected skeletal material from across the present-day surface of the chamber and opened an excavation unit that finally reached 80 cm by 80 cm to a depth of 20 cm, and a small sondage to a total depth of 70 cm at its center (Fig. 4). This excavation yielded abundant skeletal remains of *Homo naledi*. The remains of at least five individuals are commingled in this excavation unit. Many of the skeletal elements were articulated at the time of excavation or fragmented and disarticulated near each other. The overall distribution of the remains within this excavation unit exhibited clear horizontal and vertical spatial clustering, calculated using a 3D density-based clustering algorithm (Kruger et al., 2016) (Fig. 13). The presence of more steeply angled fossils, such as a near vertical femur fragment, and orientations at every direction suggests skeletal materials were also buried and have not been substantially moved through post-depositional soil movement. In comparison, the surface material tends to be at shallower angles corresponding to the shallow slopes of the chamber floor (Fig. 4b). Our work to associate skeletal remains with each other to reconstruct individuals has continued (Huber, 2011). The sondage was largely sterile, but in its lowest level produced a single baboon molar crown. The excavation and sondage were central to the dating of the *H. naledi*-bearing deposit (Girardeau-Montaut, 2011); uranium-series-ESR combined dating on *H. naledi* teeth from this excavation unit provided a maximum age of 335,000 years, while the baboon tooth from a depth of 45–50 cm, around 25–30 cm below the *H. naledi* material, yielded US-ESR age estimates of 723 ± 181 ka and 635 ± 148 ka under two different uranium uptake scenarios (Dirks et al., 2017; Wiersma et al., 2020).

The stratigraphy noted within the 2013–2016 excavation unit and sondage was described by Dirks et al. (2015). They interpreted the brown sediment comprising the floor of the cave as one stratigraphic unit divided into two sub-units, sub-unit 3a and 3b. Sub-unit 3b is the fossil-bearing stratigraphic sub-unit present across much of the present-day floor surface, while sub-unit 3a is stratigraphically below 3b, devoid of *H. naledi* material. Both sub-unit 3a and 3b contain angular clay clasts of a reddish-orange color. These clasts are interpreted as deriving from sub-units 1a and 1b, which occur in some places near the cave wall and in remnants adhering to the cave walls or in dolomite pockets. The erosion of these sub-units resulted in redeposition of clasts into the Unit 3 sediments.

In November, 2018, our team initiated renewed.,/ investigation of the Dinaledi Chamber. At that time it was apparent that fossil discoveries in the Lesedi Chamber, Hill Antechamber, and distal fissure network of the Dinaledi Subsystem had each presented situations in which skeletal remains of single individuals were localized. These situations appeared to contrast with the commingled assemblage of skeletal remains in the initial Dinaledi Chamber excavation unit. We opened two new 50 cm by 50 cm excavation units within the Dinaledi Chamber, flanking the previous excavation area on the northwest corner (S950W550) and southeast corner (S1050W500). Our goals were (1) to test whether other portions of the floor of the Dinaledi Chamber have similar subsurface concentrations of *H. naledi* skeletal material as found in the previous excavation unit; (2) to assess whether subsurface skeletal material bears any relation to remains that were recovered from the present-day surface; and (3) to further understand the stratigraphic situation in the chamber.

The excavation of the southeast unit continued in 5 cm levels until a depth of 20 cm was reached, bringing its base into line with the original excavation unit. This yielded 58 fossil specimens, mostly fragmentary including cranial fragments and long bone fragments,

although a few complete pedal elements and four teeth or teeth germs consistent with a single juvenile *H. naledi* individual were also found. The skeletal material in this unit was localized near the boundary with the larger excavation unit from the earlier excavations, across the complete range of depths. Elements within an anatomical region were in some cases clustered spatially, such as the three teeth from an immature individual. However, the evidence does not make clear whether all this material may represent a single individual, and also whether it may comprise one or more parts of the more complex array of remains from the original excavation unit.

The northwest unit (S950W550) presented a more definitive picture. This unit has a large rock jutting into its southwestern corner, which may be a projection of the chamber's bedrock floor. At 10 cm below surface, long bone elements including a partial right femur, partial tibia shaft, and partial humerus shaft were exposed across the unit just east of the rock within a single horizontal level. At the same level on the northernmost part of the unit, a semi-circular concentration of skeletal material appeared, extending into the north wall of the unit. This concentration of bone was not in direct contact with the three long bone fragments.

At this stage we elected to open an additional 50 cm unit to the north of this one, to investigate the extent of the bone concentration. In level 2 of this unit (S900W550), between 5 and 10 cm in depth, poorly preserved bone material was exposed including a left demi-mandible with premolars and molars, a partial tibia shaft, and other long bone fragments. Below this, we encountered a northward continuation of the bone concentration from the adjoining unit. We exposed the horizontal extent of this feature (Dinaledi Feature 1) at the same level as in the adjacent S950W550 unit. During this phase of excavation, we collected bone fragments and elements that excavation exposed; these specimens are listed in SI 2.1.

After the pause in excavation, we returned to the Dinaledi Chamber to sample sediment within and around Feature 1. Our aim was to better characterize the local sediment profile and provide material for analysis of the sediment composition. We cleaned a profile at the south end of the feature, without disrupting any of the remaining skeletal material.

At this time, we also worked to identify skeletal material exposed on the surface of the feature. Many of the remaining elements are partially obscured by sediment and we have not removed sediment for the purpose of identification. At the southern end of the exposed feature are cranial vault fragments consistent with a single partially crushed cranium. Vault fragments at the edge of the feature are in angled positions supported by underlying matrix. Near this and extending into the center of the feature are vertebral remains, including two vertebral bodies in articulation. A partial ribcage is present at the west center of the feature, with rib elements remaining *in situ* in a vertical or near-vertical position supported by matrix. Toward the east within the feature are visible long bone shafts that correspond in size to femur or tibia. A partial fibula shaft is also exposed in this part of the feature. Toward the north of these hindlimb fragments are identifiable portions of the right mandibular body, including at least four premolar and molar teeth in place (Fig. 9).

We compared the remaining *in situ* identifiable material to the skeletal material excavated from the feature to evaluate their compatibility, finding that all material is compatible with a single adult individual with the exception of three fragments of immature elements. Most of the identifiable elements within Feature 1 were positioned in ways that follow anatomical logic for a whole body with arms and legs flexed into a compact orientation. Large fragments of cranial vault are localized near the south end of the feature and are matrix-supported. Above this fragmented vault were upper limb elements. Lower limb elements remain in the central portion of the feature, below and to the east of a partial

ribcage with matrix-supported rib fragments. The fragments of the mandible are separated from the position of the vault, with the fragments of right mandibular corpus and associated teeth in roughly the center of the feature and a fragment of left mandibular corpus above and separated from the concentration of bone, near its north end. One zygomatic fragment and small (<20mm) fragments of vault are also in this area. Without fully excavating the feature, it is difficult to test hypotheses about the original position and subsequent decompositional collapse of the skeleton. We can tentatively suggest that the body was in a tightly flexed position with the head higher toward the south end of the feature and arms flexed near the face. From this position, the mandible disarticulated and collapsed into the center of the thorax. It is possible that the further fragmentation of the mandible may reflect disturbance of the body after decomposition. It is also possible that small fragments may have been part of the sediment load above the burial and pertain to other individuals.

Hill Antechamber excavation

The Hill Antechamber U.W. 107 is the portion of the Dinaledi Subsystem nearest to the present-day entrance access into the subsystem (Elliott et al., 2021). This space is accessible today via the ca. 12 m vertical passage known as the Chute, which descends into its northern edge. There are two exit avenues, both narrow (< 0.5 m) passageways that lead in parallel to the Dinaledi Chamber; there are also small (< 0.2 m) fissure passages exiting this chamber to the west and north. The floor of the Hill Antechamber forms a ca. 30 degree slope with the highest point near the Chute and lowest point at the southwest edge of the chamber (Figure S3). Our team recovered one tooth and a small number of bone fragments from the floor surface of the Hill Antechamber in 2013; these are included in the sample published in Berger et al. (2015).

In 2017 the team began work in the Hill Antechamber with the goal of understanding the interaction of *Homo naledi* with the Chute. At that point we had collected more than 1500 fossil specimens of *Homo naledi* from the Dinaledi Subsystem, and all but a handful of these came from the Dinaledi Chamber. The largest concentration of bone at that point had been excavated in a single 80 cm square unit within the Dinaledi Chamber, approximately 12 meters from the Chute (Figure S14). The closest point of the Dinaledi Chamber to the Chute is ca.8 meters, and at least 5 meters of that distance is through one of the narrow (< 0.5 m) passages. We considered the hypothesis that *Homo naledi* skeletal material may have been deposited into the Chute, either fleshed or unfleshed, accumulating at the base of the Chute in sufficient quantity for gravity to bring portions into the Dinaledi Chamber. Under this hypothesis, we predicted that the sloping floor of the Hill Antechamber should correspond to a talus deposit including *Homo naledi* body parts and possibly other material including artifacts. The distance and physical constraints of this part of the subsystem made it hard to understand how a substantial concentration of *Homo naledi* skeletal material, including articulated limbs, could occur in the subsurface of the Dinaledi Chamber at such a distance from the Chute. We also considered the hypothesis that living individuals of *Homo naledi* had entered the subsystem via the Chute. This hypothesis would help to explain the concentration of material within the Dinaledi Chamber but did not make any clear prediction about the subsurface content of the Hill Antechamber.

In September 2017, we established a datum for the subsystem near the northeast extreme of the Hill Antechamber and established a grid based on a local north extended throughout the subsystem (Figure S2). This local north diverges from magnetic north by 35 degrees NW; maps here are presented relative to magnetic north. The grid system was projected into the spaces with laser level and laser rangefinding equipment. The spatial

location of each fossil fragment was recorded from measurements prior to recovery, with scaled photographs taken *in situ*. Photography for photogrammetry was carried out approximately daily and sometimes at shorter intervals. Metashape 1.8.1 Standard (Agisoft) was used to generate 3D models of the excavation from these series of photographs. The resulting 3D models were correlated with 3D point cloud data generated by a Faro laser instrument.

We initiated fieldwork in the Hill Antechamber with a surface search, which identified additional small fossil fragments. Within the Antechamber, the team opened three 50 cm excavation units. One of these at grid unit N100W50 was a half unit against the north wall of the Antechamber. This unit produced only a small number of unidentifiable fossil fragments. A second unit, at N50W100 was the nearest full 50 cm square to the base of the Chute. It is this second unit that produced the Hill Antechamber feature. The third unit, S150W150, was lower on the slope near the opening to the parallel narrow passages that lead to the Dinaledi Chamber. This area was covered with flat rocks (Figure S15). After documenting and lifting of the rocks, excavation in this unit revealed some skeletal material, including a partial maxillary dentition of an adult individual of *H. naledi* and fragments of cranial and postcranial skeletal material, including some attributable to tibiae or femora. It is unclear if the rocks are associated with the presence of the underlying skeletal material. In addition to these three excavation units, the team investigated a small pocket of sediment on the north wall of the chamber, and excavated the thin layer of sediment upon the flowstone shelf at the base of the Chute. No skeletal material came from these two areas.

Excavation of the Hill Antechamber units followed methodology previously described for work in the Rising Star cave system (Berger et al., 2015; Hawks et al., 2017). No metal instruments were used for excavation. On the highly sloped units in the Hill Antechamber we

595 proceeded with a terraced approach to bring the excavation surface down in horizontal steps of 5 cm. During the excavation of the unit at N50W100, we encountered a substantial area of fragmented and powdery bone material beginning at a depth 5 cm below surface, near the north end of the unit (Figure S16). Leaving this material in place, we continued to excavate within the designated unit to reveal its extent. As we exposed this material further toward the 600 south, we found that it included some more complete fossil elements and extended across more than half the horizontal area of the 50 cm x 50 cm unit. At this stage we decided to delineate the edge of this feature and excavate more deeply around it to form a pedestal that could be removed *en bloc* from the cave system for further work in the laboratory (Figure S17). The material extended to the east and south edges of the N50W100 square, and so we 605 opened half of the neighboring grid squares at N50W50 and S50W100, and the northwest quadrant of S50W50 to fully expose the boundaries of the feature. By the end of excavation in March 2018, an area of 75 cm x 75 cm was excavated down to a horizontal level 40.5 cm below datum, leaving the bone-containing feature as a pedestal. Only a small number of fossil elements and fragments occurred within the surrounding excavated area.

610 All material and people entering and exiting the Dinaledi Subsystem must pass through the constraints of the Chute, which places a severe size limit on any excavated blocks of material. The overall size of the Hill Antechamber feature was incompatible with removal from the subsystem in a single block. We therefore planned for a segmentation of the feature into a minimal number of pieces. The contour of the surface of the feature presented an upper 615 surface dense with bone elements and bone material through most of the western two-thirds, while the eastern third of the feature lacked any bone at this level and presented deeper, less uniform bone material (Figure S18). This suggested a division of the feature to separate the eastern portion would be most appropriate. We applied a plaster jacket to the east wall of the

feature and allowed it to solidify. We then excavated into the feature gradually to separate this portion from the overall mass, using toothpicks to confine its lower and western boundaries. Once separated, this block (U.W. 101-2074) measured 9 by 23 by 9 cm. We followed a similar approach to remove a second somewhat larger block that partially underlay the first. The resulting block, U.W. 101-2075, measured 21 by 26 by 11.5 cm. Finally, we jacketed the top and sides of the remaining mass of the feature (Figure S19 jacketed block). We used two thin metal sheets to separate the feature from the underlying sediment, then inverted it, applied a rigid plastic sheet to the bottom surface, and covered this bottom with plaster. The resulting mass, designated as U.W. 101-2076*, measured 40 cm by 49 cm by 19 cm at its maximum dimensions. We wrapped all plaster jacketed masses in bubble wrap and additional padding, placing them in waterproof cave haul bags. The team brought them out of the cave system without incident (Figure S20).

In the lab we prioritized the plaster-jacketed masses for imaging. The smaller jacketed masses, U.W. 101-2074 and U.W. 101-2075, were suitable for imaging with the Nikon Metrology XTH 225/320 microtomography (microCT) scanner housed at the Evolutionary Studies Institute of the University of the Witwatersrand. These were scanned at a voxel size of 72 microns. The larger jacketed mass, U.W. 101-2076, was not suitable for scanning with this instrument, and so we obtained a clinical CT from a Siemens Somatom Definition AS 40 (Erlangen, Germany) with larger gantry size in the Charlotte Maxeke Johannesburg Academic Hospital (CMJAH), with a 0.5mm voxel size. We segmented these models with a combination of manual and density threshold segmentation strategies.

A possible stone artefact was recognized on the clinical CT (Figure S21; SI 3.2). It was then scanned as a focused target at the European Synchrotron Radiation Facility (ESRF) in Grenoble France. This scan was performed using propagation phase-contrast on the

beamline BM18, using an isotropic voxel size of 16.22um and a propagation distance of 6m. The average detected energy was 156 keV, obtained by filtering the white beam of the BM18 tripole wiggler with 2.62mm of molybdenum. We used an indirect X-ray detector based on a LuAG:Ce scintillator of 2mm thickness, coupled to a PCO edge 4.2 CLHS camera through a Hasselblad 120mm macro objective.

Analytical and computational methods used for studying sediments

We used x-ray diffraction (XRD) and x-ray fluorescence (XRF), respectively, to study the mineralogy and chemistry of the samples. To study the textures, we used scanning electron microscopy (SEM) on the sediments mounted in epoxy resin to create polished blocks. On the SEM, backscattered electron (BSE) imaging was used to observe the textures of the sediments and energy dispersive spectroscopy (EDS) was used for semi-quantitative chemical mapping and spot analysis of the observed mineral grains. The methodologies, software, and measurement parameters/conditions for XRD, XRF and SEM were as used for Dirks et al. (2015) at the Spectrum Analytical Facility of the University of Johannesburg (UJ). The XRF results were treated with Principal Component Analysis (PCA) computed using the MATLAB Statistics and Machine Learning Toolbox PCA function *pca* on 12 major elements (Al, Ba, Ca, Fe, K, Mg, Mn, Na, P, S, Si, Ti). PCA is the standard method for unmixing mixed variables. The output of the function *pca* includes the principal component loads, the scores, and the variances. The data correlations were implemented using the function *corrplot* which uses Pearson's correlation coefficient. The particle-size distribution (PSD) was carried out at the Department of Metallurgy at UJ using the Microtrac S3500 laser-diffraction particle size analyzer. The obtained results were reduced using GRADISTAT, the grain size and statistics package (Blott and Pye, 2001), and selecting the Folk and Ward

Method to obtain the mean grain size, sorting, skewness and kurtosis in addition to the percentages of clay, silt and sand in each sample.

Acknowledgements

Permits to conduct research in the Rising Star Cave system are provided by the South African National Research Foundation (LRB). Permission to work in the Rising Star cave is given by the LRB Foundation for Research and Exploration. We would like to thank the University of the Witwatersrand's Primate Fossil Access Committee for allowing access to the original material for study and the University Curator and Assistant Curator of Collections for assisting with logistics in studying the material. We would like to thank the Department of Diagnostic Radiology at the Charlotte Maxeke Academic Hospital for allowing access to their clinical CT scanner. We acknowledge the European Synchotron Research Facility for providing access to facilities including the BM18 beamline. We would like to thank Paloma de la Pena and Matthew Caruana for discussions related to the lithic associated with the Hill Antechamber burial. The Authors would like to acknowledge the funders of the various expeditions that recovered the fossil material and information, including 3d scanning and the production of AVR material described in this paper including the National Geographic Society (LRB, CJ, KB), the Lyda Hill Foundation (LRB) and the National Research Foundation of South Africa (LRB). Laboratory work and travel was funded by the National Geographic Society (LRB, ME, AK, CJ, KB), the Lyda Hill Foundation (LRB, ME, AK) the Centre for Excellence in PalaeoSciences at the University of the Witwatersrand (now GENUS) (AK), the Fulbright Scholar Program (JH), and National

Research Foundation of South Africa (TVM), University of Johannesburg Research Council (TVM), Spectrum Analytical Facility at University of Johannesburg (TVM).

Author and article information

Author contributions

Conceptualization: LRB, JH

Methodology: LRB, JH, TM, ZJ, ME, PRQ, BC, GC, KJ, CJ, KB, AK, CW

Investigation: LRB, TM, KM, AK, PRQ, ME, BP, AF, PT, VB, KD, ZJ, ABG, JB, GC, PHMD, EF, AG, NH, LH, RH, KJ, HM, EP, MR, ER, JSS, MT, ST, DVR, KW, MK, PS, JH

Visualization: LRB, TM, KM, AK, PRQ, ME, BP, PT, VB, KD, ZJ, ABG, KB, GC, EF, AG, NH, LH, RH, KJ, CJ, MR, HM, JSS, MT, ST, DVR, KW, CW, JH

Funding acquisition: LRB, ME, AK, CJ, KB, TVM

Project administration: LRB

Writing – original draft: JH, LRB

Writing – review & editing: LRB, TM, KM, AK, PRQ, ME, BP, AF, PT, VB, KD, ABG, KB, JB, GC, PHMD, EF, AG, NH, LH, RH, KJ, CJ, HM, EP, MR, ER, JSS, MT, ST, DVR, KW, CW, MK, PS, JH

Competing interests

The authors declare that they have no competing interests with the production or publication of this research.

Provenience

All fossil and archaeological material studied in this work was recovered by the authors. Details of their context are presented within this paper. The materials are curated at the University of the Witwatersrand. All materials and scans are available for study through application to the Primate Fossil Access Committee of the University of the Witwatersrand. 3D shape files and images of HAA1 are available via Creative Commons License by Attribution on https://Morphosource.org. Movies and Augmented Virtual Reality data are available for download via Figshare.

Additional files

Supplementary Movies

SM1. Augmented Virtual Reality of the Hill Antechamber and the Dinaledi Chamber

SM2. HAA1 visualization movie

SM3. Hill Antechamber Block movie

Supplementary Information (SI) file contents

Supplementary Information 1: Petrography and geochemistry of sediments

Supplementary Information 1.1: Unlithified Mud Clast Breccia (UMCB) in passages of the Dinaledi Subsystem compared to UMCB on the Dinaledi floor

Supplementary Information 1.2. Grain size analysis of sediments around Feature 1 and the Lesedi Chamber

Supplementary Information 2: Hominin skeletal material and element representation

Supplementary Information 2.1: Identification and assessment of skeletal remains from Dinaledi Feature 1

Specimen list

Supplementary Information 2.2. Identification and assessment of skeletal remains from Dinaledi Feature 2

Supplementary Information 3: Hill Antechamber Feature and Artefact

Supplementary Information 3.1. Stratigraphic situation of the Hill Antechamber feature

Supplementary Information 3.2: Description of the Hill Antechamber Artefact 1 associated with the Hill Antechamber Feature

Supplementary Information 4: Materials and Methods

Supplementary Information 4.1: Previous Excavations in the Dinaledi Chamber

Supplementary Information 4.2. Previous work in other parts of the cave system

Supplementary Table 1.

Supplementary Table 2.

Supplementary Figures

References

Argue, D., Groves, C. P., Lee, M. S., & Jungers, W. L. (2017). The affinities of Homo floresiensis based on phylogenetic analyses of cranial, dental, and postcranial characters. *Journal of human evolution*, *107*, 107-133.

Arsuaga, J. L., Martínez, I., Arnold, L. J., Aranburu, A., Gracia-Téllez, A., Sharp, W. D., ... & Carbonell, E. (2014). Neandertal roots: Cranial and chronological evidence from Sima de los Huesos. *Science*, *344*(6190), 1358-1363.

Berger, L. R., Hawks, J., de Ruiter, D. J., Churchill, S. E., Schmid, P., Delezene, L. K., ... & Zipfel, B. (2015). Homo naledi, a new species of the genus Homo from the Dinaledi Chamber, South Africa. *elife*, *4*, e09560.

Blott, S.J. and Pye, K. (2001) GRADISTAT: a grain size distribution and statistics package for the analysis of unconsolidated sediments. *Earth Surface Processes and Landforms* 26, 1237-1248.

Bolter, D. R., Hawks, J., Bogin, B., & Cameron, N. (2018). Palaeodemographics of individuals in Chamber using dental remains. *South African Journal of Science*, *114*(1-2), 1-6.

Brophy, J. K., Elliott, M. C., De Ruiter, D. J., Bolter, D. R., Churchill, S. E., Walker, C. S., ... & Berger, L. R. (2021). Immature hominin craniodental remains from a new locality in the Rising Star Cave System, South Africa. *PaleoAnthropology*, 2021 (1) 1-14.

Caparros, M., & Prat, S. (2021). A Phylogenetic Networks perspective on reticulate human evolution. *Iscience*, *24*(4), 102359.

Dembo, M., Radovčić, D., Garvin, H. M., Laird, M. F., Schroeder, L., Scott, J. E., ... & Collard, M. (2016). The evolutionary relationships and age of Homo naledi: An assessment using dated Bayesian phylogenetic methods. *Journal of Human Evolution*, *97*, 17-26.

Dirks, P. H., Berger, L. R., Roberts, E. M., Kramers, J. D., Hawks, J., Randolph-Quinney, P. S., ... & Tucker, S. (2015). Geological and taphonomic context for the new hominin species Homo naledi from the Dinaledi Chamber, South Africa. *Elife*, *4*, e09561.

Dirks, P. H., Roberts, E. M., Hilbert-Wolf, H., Kramers, J. D., Hawks, J., Dosseto, A., ... & Berger, L. R. (2017). The age of Homo naledi and associated sediments in the Rising Star Cave, South Africa. *Elife*, *6*, e24231.

Girardeau-Montaut, D. (2011). Cloudcompare-open source project. *OpenSource Project*, *588*(6).

Huber, D. (2011, January). The ASTM E57 file format for 3D imaging data exchange. In *Three-Dimensional Imaging, Interaction, and Measurement* (Vol. 7864, pp. 88-96). SPIE. Available from: https://www-spiedigitallibrary-org.ezp.sub.su.se/conference-proceedings-of-spie/7864/78640A/The-ASTM-E57-file-format-for-3D-imaging-data-exchange/10.1117/12.876555.short

Elliott, M., Makhubela, T., Brophy, J., Churchill, S., Peixotto, B., Feuerriegel, E., ... &

Berger, L. (2021). Expanded Explorations of the Dinaledi Subsystem, Rising Star Cave System, South Africa. *Paleoanthropology*, 2021(1), 15-22.

Hawks, J., Elliott, M., Schmid, P., Churchill, S. E., Ruiter, D. J. D., Roberts, E. M., ... & Berger, L. R. (2017). New fossil remains of Homo naledi from the Lesedi Chamber, South Africa. *Elife*, *6*, e24232.

Kruger, A. (2017). *Site formation processes at Rising Star: Taphonomy and 3D spatial analyses of the Homo naledi assemblage* (Doctoral dissertation, University of the Witwatersrand, Faculty of Science, School of Geosciences).

Kruger, A., Randolph-Quinney, P., & Elliott, M. (2016). Multimodal spatial mapping and visualisation of Dinaledi Chamber and Rising Star Cave. *South African journal of science*, *112*(5-6), 1-11.

Martinón-Torres, M., d'Errico, F., Santos, E., Álvaro Gallo, A., Amano, N., Archer, W., ... & Petraglia, M. D. (2021). Earliest known human burial in Africa. *Nature*, *593*(7857), 95-100.

Knüsel, C. J., & Schotsmans, E. M. (Eds.). (2022). *The Routledge Handbook of Archaeothanatology: Bioarchaeology of Mortuary Behaviour*. Routledge.

Maureille, B. (2022). The earliest European burials. In Metcalf, P., & Huntington, R. (1991). *Celebrations of death: The anthropology of mortuary ritual*, (pp. 140-158). Cambridge University Press.

Mickleburgh, H. L., & Wescott, D. J. (2018). Controlled experimental observations on joint disarticulation and bone displacement of a human body in an open pit: implications for funerary archaeology. *Journal of Archaeological Science: Reports*, *20*, 158-167.

Pearson, M.P. (1999). The archaeology of death and burial. Texas A&M University Press, *College Station*.

Pettitt, P., & Anderson, J. R. (2020). Primate thanatology and hominoid mortuary archeology. *Primates*, *61*(1), 9-19.

Robben, A. C. (Ed.). (1991). *Death, mourning, and burial: A cross-cultural reader*. John Wiley & Sons.

Robbins, J. L., Dirks, P. H., Roberts, E. M., Kramers, J. D., Makhubela, T. V., Hilbert-Wolf, H. L., ... & Berger, L. R. (2021). Providing context to the Homo naledi fossils: Constraints from flowstones on the age of sediment deposits in Rising Star Cave, South Africa. *Chemical Geology*, *567*, 120108.

Roksandic, M., Haglund, W. D., & Sorg, M. H. (2002). Position of skeletal remains as a key to understanding mortuary behavior. *Advances in forensic taphonomy: method, theory, and archaeological perspectives*, 99-117.

Sala, N., Pantoja-Pérez, A., Gracia, A., & Arsuaga, J. L. (2022). Taphonomic-forensic analysis of the hominin skulls from the Sima de los Huesos. *The Anatomical Record*. https://doi.org/10.1002/ar.24883

Francis Thackeray, J. (2015). Estimating the age and affinities of Homo naledi. *South African Journal of Science*, *111*(11-12), 1-2.

Tillier, A. M. (2022). Early Primary Burials: Evidence from Southwestern Asia. In *The Routledge Handbook of Archaeothanatology* (pp. 124-139). Routledge.

Val, A. (2016). Deliberate body disposal by hominins in the Dinaledi Chamber, Cradle of Humankind, South Africa?. *Journal of Human Evolution*, *96*, 145-148.

Wiersma, J. P., Roberts, E. M., & Dirks, P. H. (2020). Formation of mud clast breccias and the process of sedimentary autobrecciation in the hominin-bearing (Homo naledi) Rising Star Cave system, South Africa. *Sedimentology*, *67*(2), 897-919.

Zipfel, B., & Berger, L. R. (2009). New Cenozoic fossil-bearing site abbreviations for collections of the University of the Witwatersrand. *Palaeontologica Africana*, *44*, 77-81.

Figures

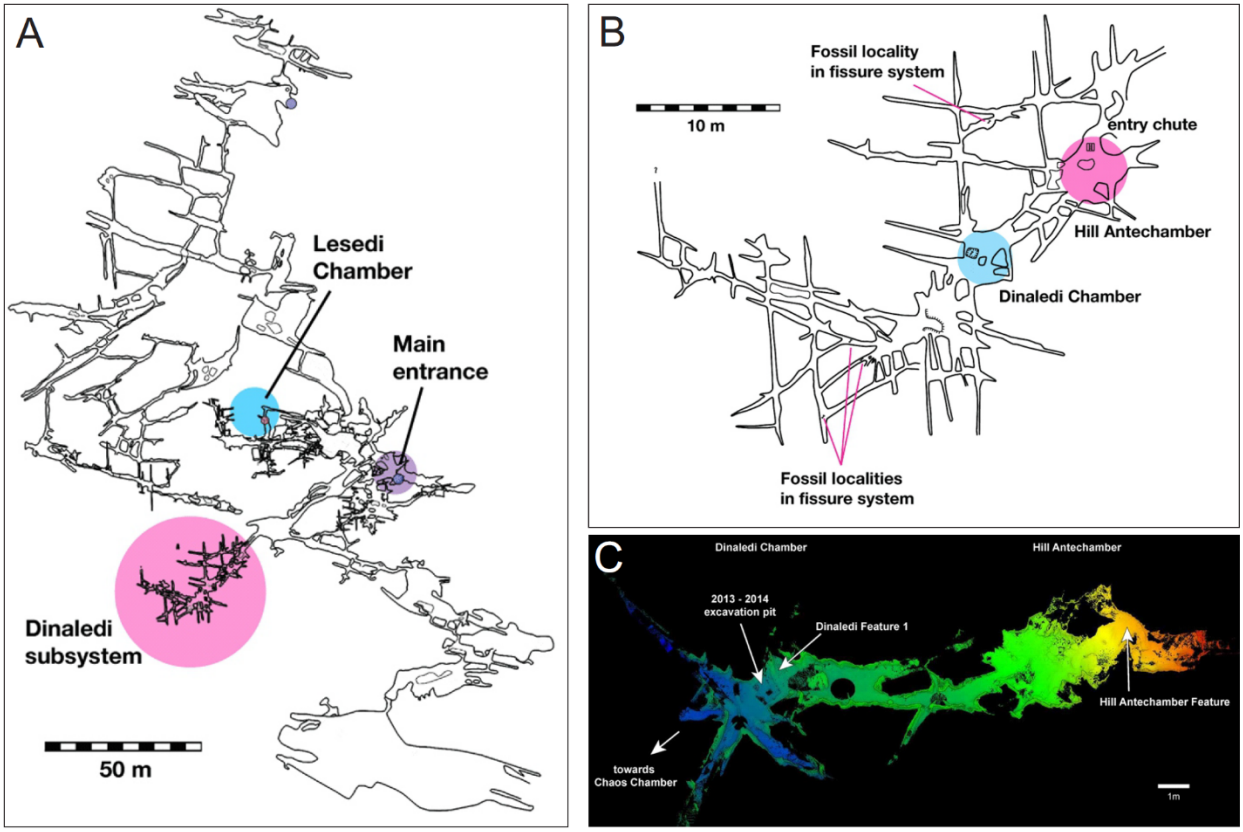

Figure 1. Maps of the study locality. (A) Rising Star cave system. The locations of the Dinaledi subsystem (enlarged in B), Lesedi Chamber, and main cave entrance are indicated. (B) Location of Hill Antechamber within the Dinaledi Subsystem. (C) Floor profile of Hill Antechamber and Dinaledi Chamber showing height and angle of grade, and excavation areas.

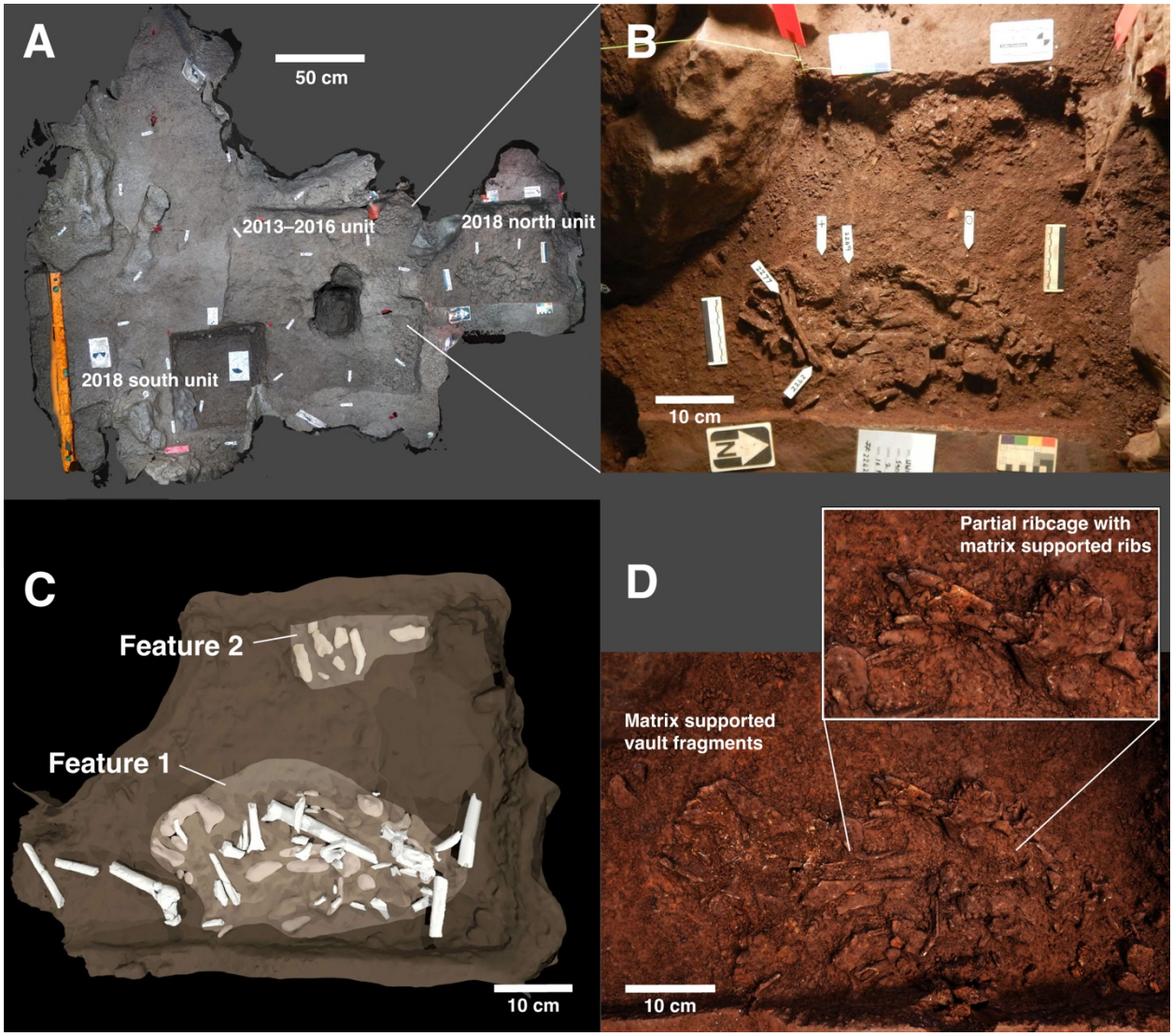

Figure 2. Dinaledi Chamber burial features. (A) Photogrammetry model of the Dinaledi Chamber floor and excavation areas. Locations of 2013–2016 excavation area and two 2018 excavation units are labelled. The rectangle indicates the area of the other panels. (B) Photograph of excavation area including Feature 1 and Feature 2. (C) Three-dimensional reconstruction of excavation area including both the excavated skeletal material and the unexcavated material in spatial position. The oval area of Feature 1 corresponds to the sediment contrast and outline of skeletal material remaining *in situ*. Three excavated bones at left and one at right were stratigraphically higher and outside the feature. (D) Three-

dimensional reconstruction from photogrammetry of Feature 1, indicating evidence of matrix-supported elements.

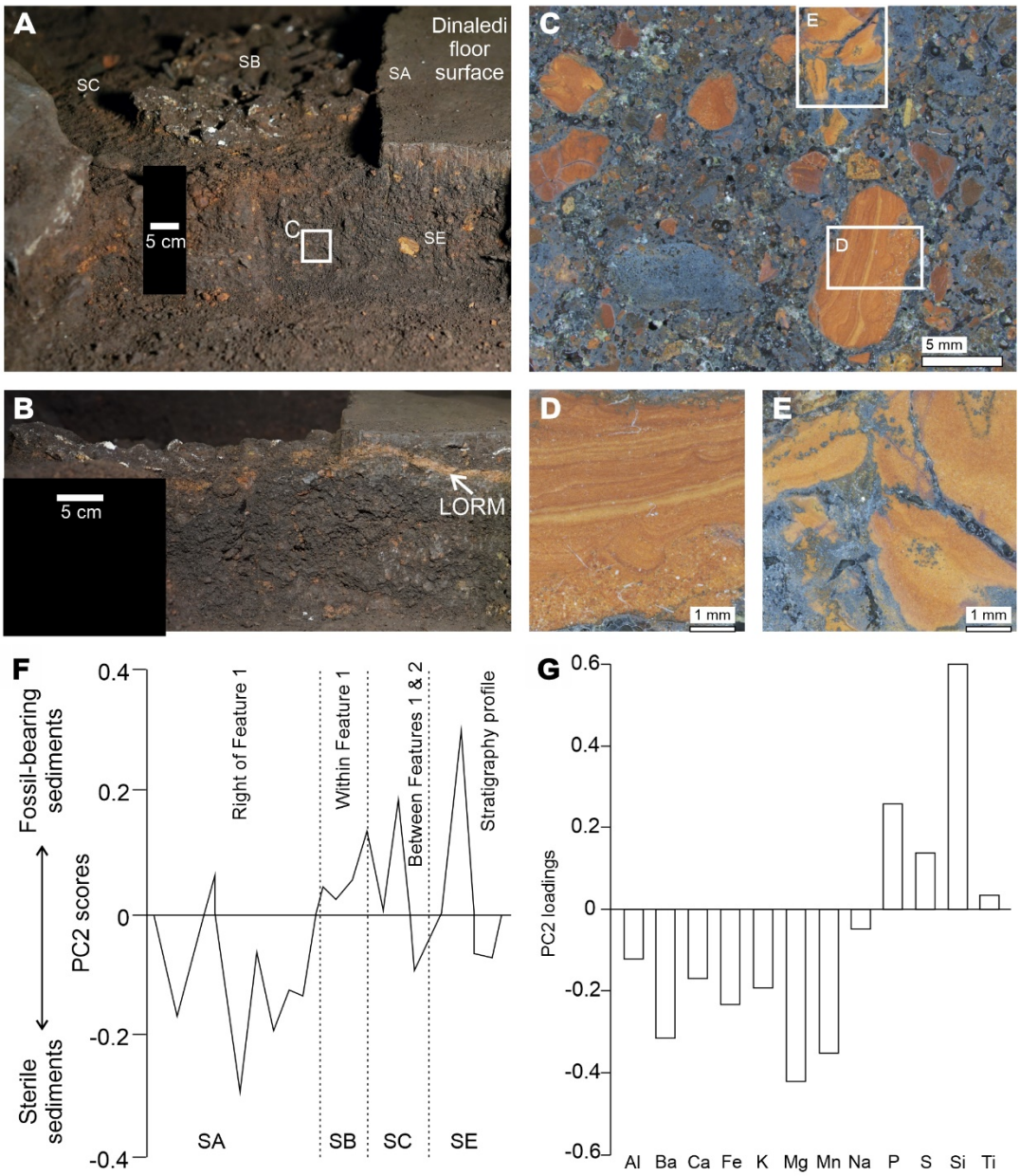

870

Figure 3. Sedimentology and stratigraphy of unlithified mud clast breccia and laminated orange-red mud clasts surrounding the burial Feature 1 on the Dinaledi floor. (A) North-facing overview of Feature 1 showing the relation of the sediments around the fossils and height of profile. (B) Profile view. Feature 1 occurs within unlithified mud clast breccia rich
875 in orange-red clasts. A continuous laminated orange-red mud layer beneath unexcavated floor surface dips near the feature, where it becomes fragmented and muddled. (C)

Photomicrograph of sediment beneath the burial feature showing the *in situ* poorly sorted fabric of the unlithified mud clast breccia. (D) Close-up photomicrograph of a laminated orange-red mud clast. The clast contains up to 30% sand and has mm-scale laminations. (E) Close-up photomicrograph of laminated orange-red mud clasts coated and impregnated with secondary Mn- and Fe-oxyhydroxides in brown-grey silt and clay matrix of the unlithified mud clast breccia. (E) Principal component 2 (PC2) yields positive scores for fossil-bearing sediments and negative scores for sterile sediments (see Fig. 7). (G) PC2 loadings showing that elements with positive scores are phosphorus, sulfur, silicon and titanium.

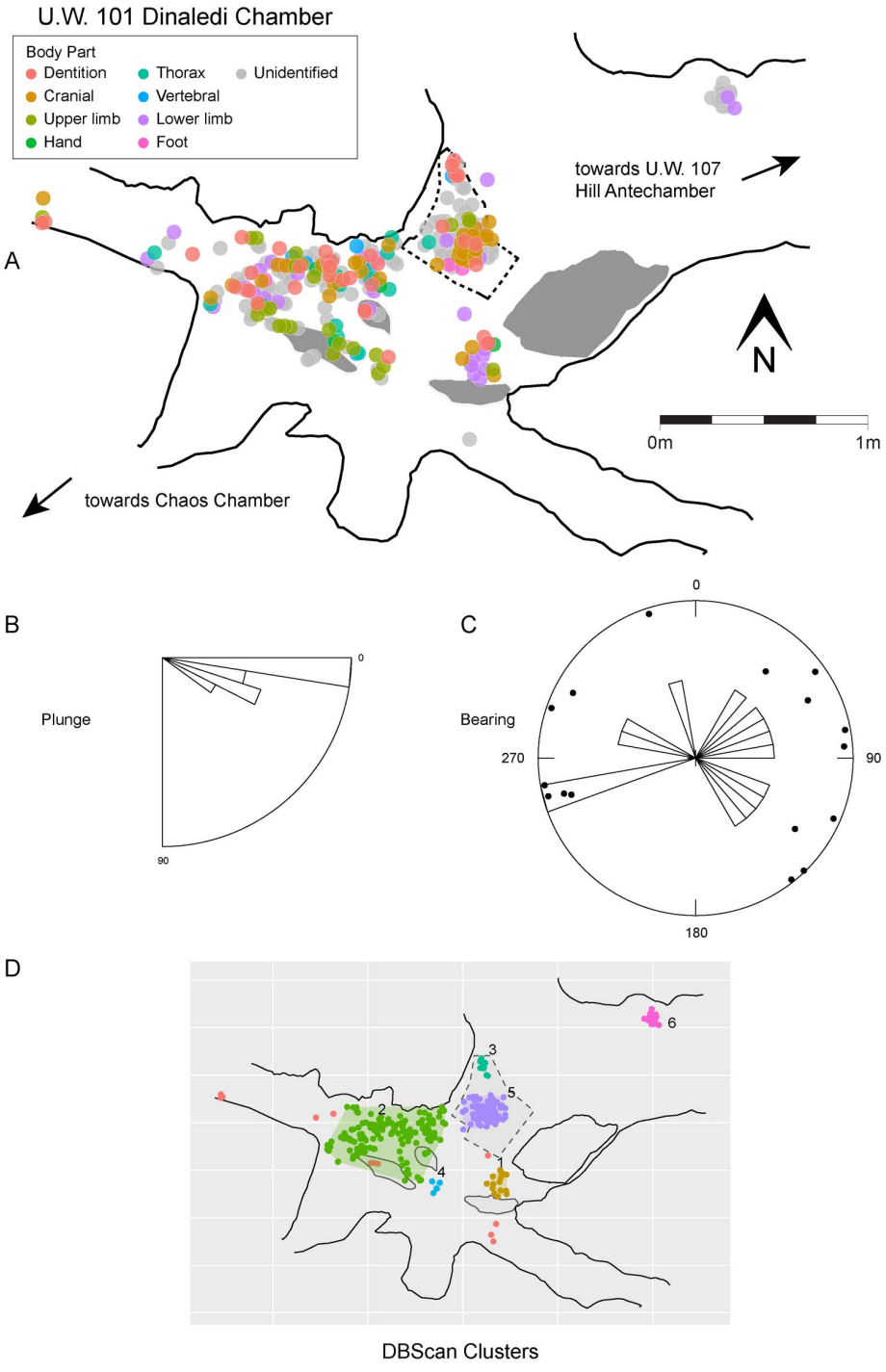

885

Figure 4. Spatial data for Dinaledi Chamber surface collected specimens in relation to excavation area. (A) Position and skeletal element identifications of surface specimens including the 2013–2014 excavation unit. For fossil fragments large enough to be mapped as with two end points (n = 16), we calculated (B) plunge angle and (C) planar orientation

890 following Brophy et al. (2021). Length of bars represent frequency of "two-shot" fossils with

a given angle. (D) Density-based cluster analysis (*7*) identified six areas of higher-density surface specimen accumulations. These six areas are indicated with different colors here (arbitrarily chosen) with outliers in red.

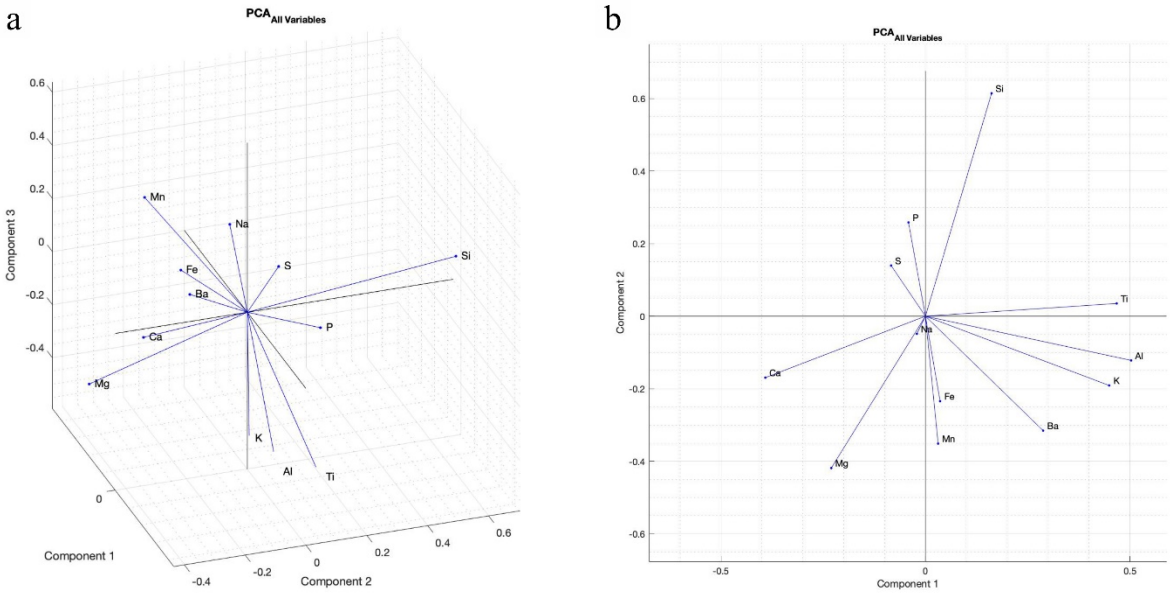

Figure 5. Principal Component Analysis (PCA) of XRF major element chemistry of fossil-bearing and sterile sediments around Feature 1 on the Dinaledi floor, the Lesedi chamber and the Dinaledi Subsystem. (a) Three-dimensional (3D) biplot showing the three components that apply to all the variables (major elements). (b) Two-dimensional (2D) biplot showing component 1 vs component 2 for all the variables. Component 1 shows the dominance of Ti, Al, K and Ba vs Ca and Mg, which is consistent with the clay-rich mudstone sediments and their uncalcified nature. Component 2 shows the dominance of Si, P and S vs all other elements, but mainly Mn and Fe. It is useful for delineating fossil-bearing sediments from sterile sediments.

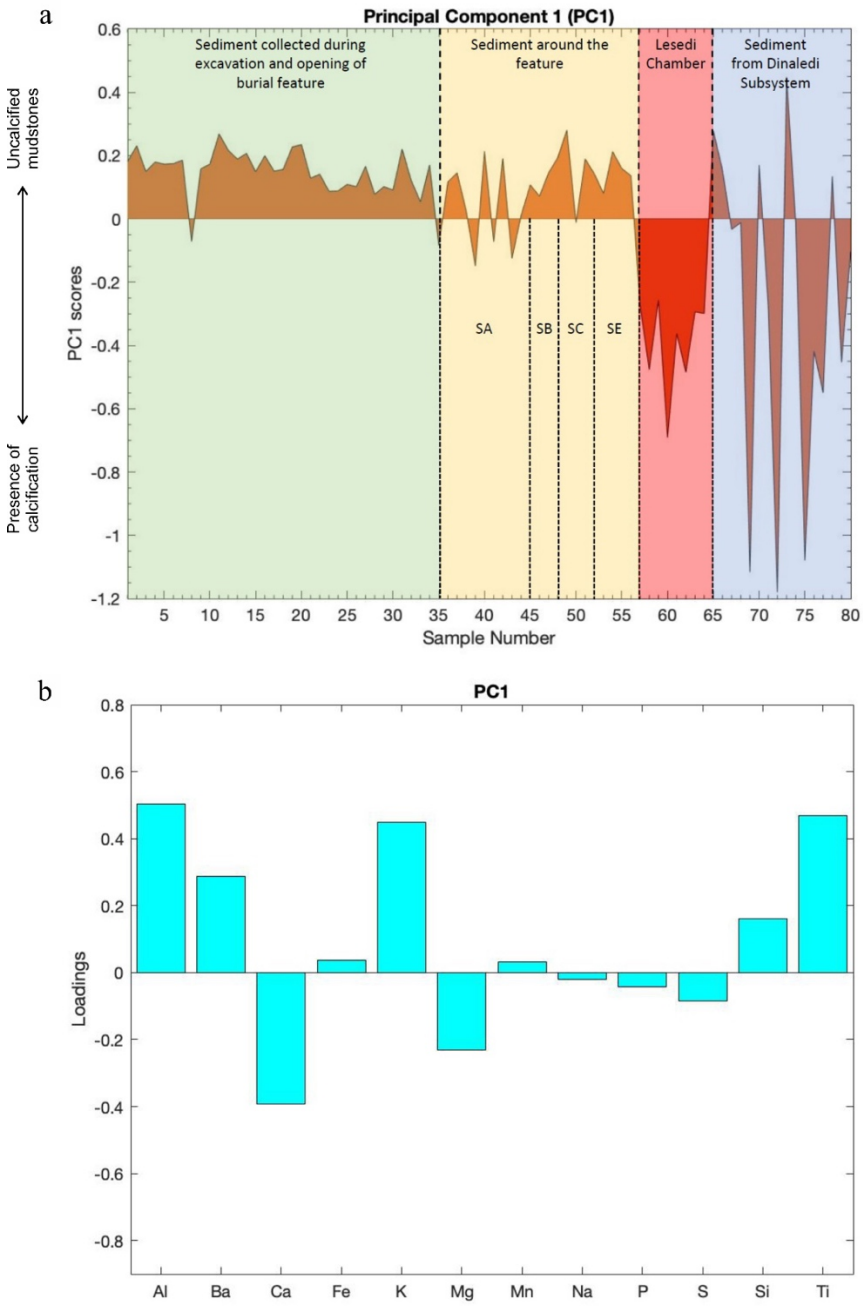

Figure 6. Principal Component 1 (PC1) scores and loadings. (a) Scores showing that almost all the samples from the Dinaledi floor have positive PC1 scores (uncalcified) compared to all the Lesedi Chamber samples and some samples from the Dinaledi Subsystem. The samples that have negative scores are calcified. Different colours represent different areas/chambers of the Rising Star cave system as annotated. (b) The positive and negative loadings of the elements on PC1 showing that Ca, Mg, S, P and Na have negative loadings and their

915 composition and controls are different from all the other elements, which have positive loadings.

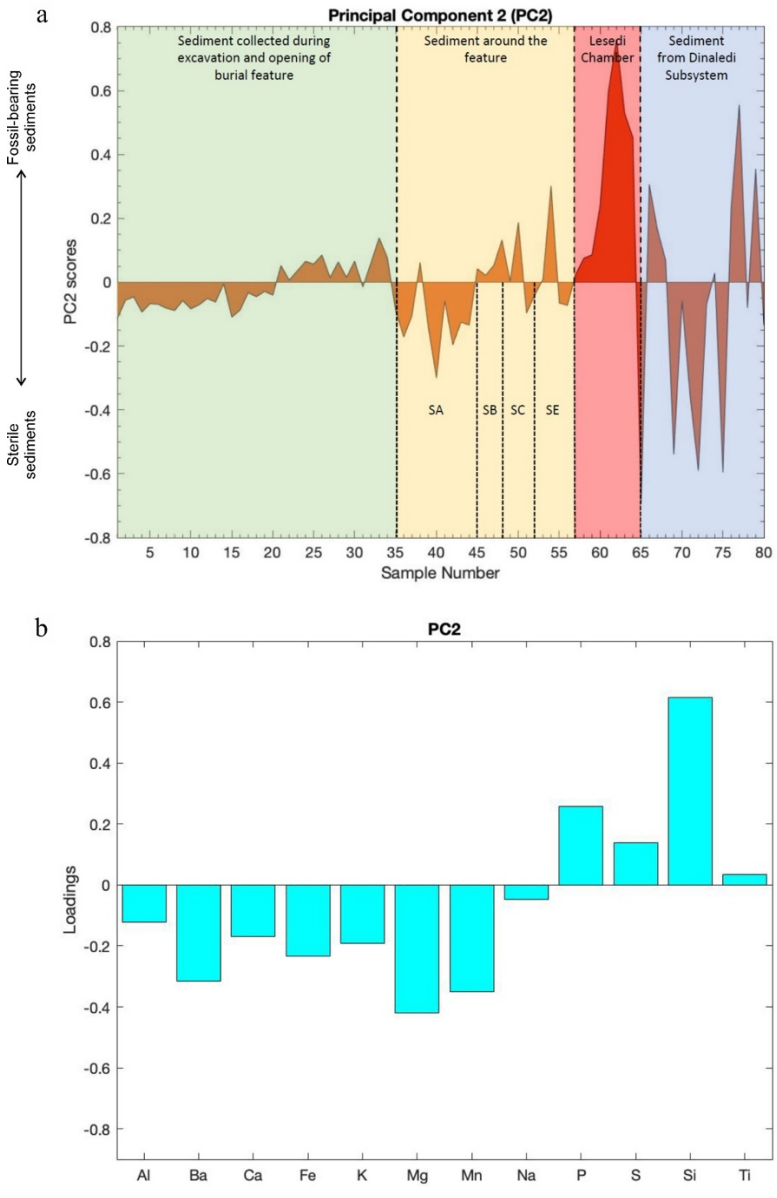

Figure 7. Principal Component 2 (PC2) scores and loadings. (a) Scores showing samples that come from sediments that contain fossils vs those that are sterile. The results are consistent with field observations and excavation results. For example, only one of the SA group samples from sterile areas around Feature 1 shows a positive score (presence of fossils) unlike all the SB group samples from inside Feature 1. Further, some samples of sediments (SC group) between features 1 and 2 and those from vertical profile on the side of Feature 1

(SE group) show a mixture of negative and positive scores. Different colours represent different areas/chambers of the Rising Star cave system as annotated. (b) The positive and negative loadings of the elements on PC2 showing that Si, P, S and Ti have positive loadings suggesting different controls of these elements compared to all the other elements, which have negative loadings.

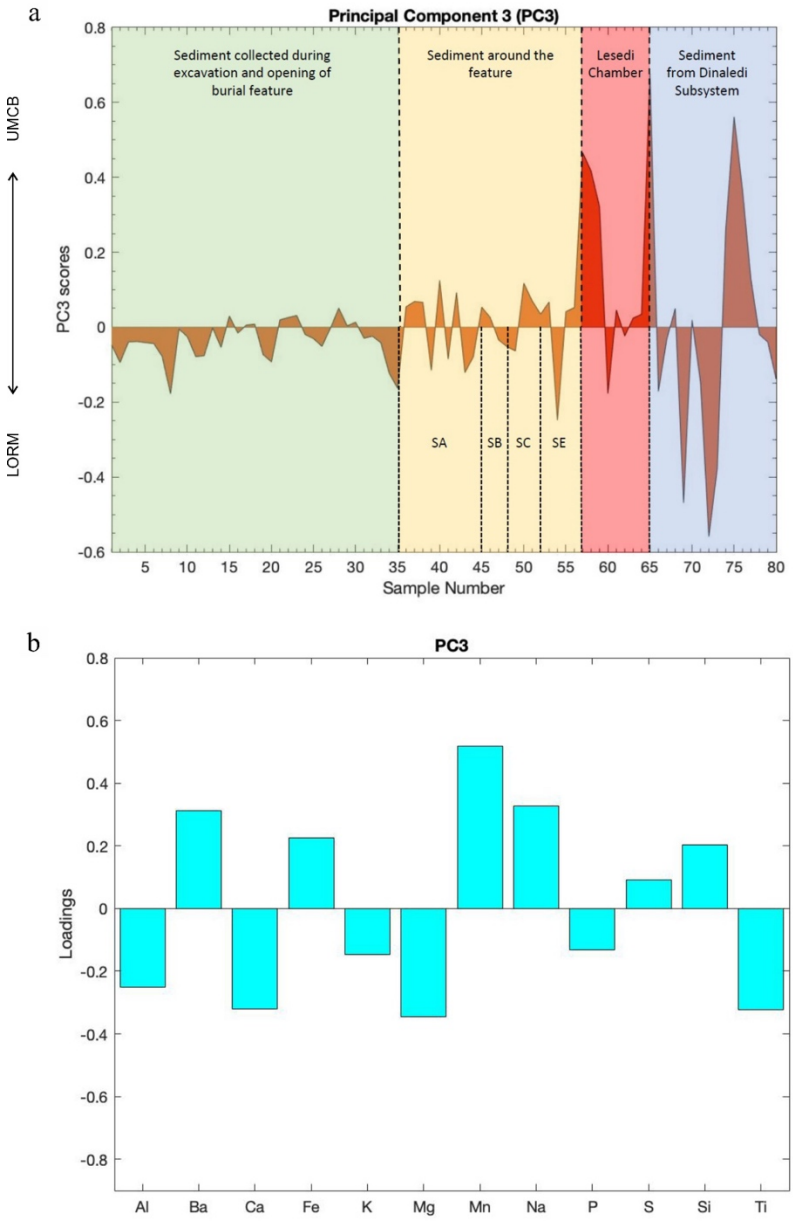

Figure 8. Principal Component 3 (PC3) scores and loadings. (a) Positive scores show samples that are dominated by UMCB vs those with negative scores and are dominated by LORM. The samples from the sediments collected during excavation and opening of the features were sieved and not collected *in situ*, so their scores are probably biased towards LORM because of the abundance of LORM in the floor sediments. Different colours represent different areas/chambers of the Rising Star cave system as annotated. (b) The positive loadings of Mn,Ba and Fe on PC3 are consistent with LORM mud clasts that have been altered to UMCB vs the LORM mud clasts that are still unaltered and dominated by elements showing the negative loadings of mainly Al, Mg, K (see Figure S7).

945

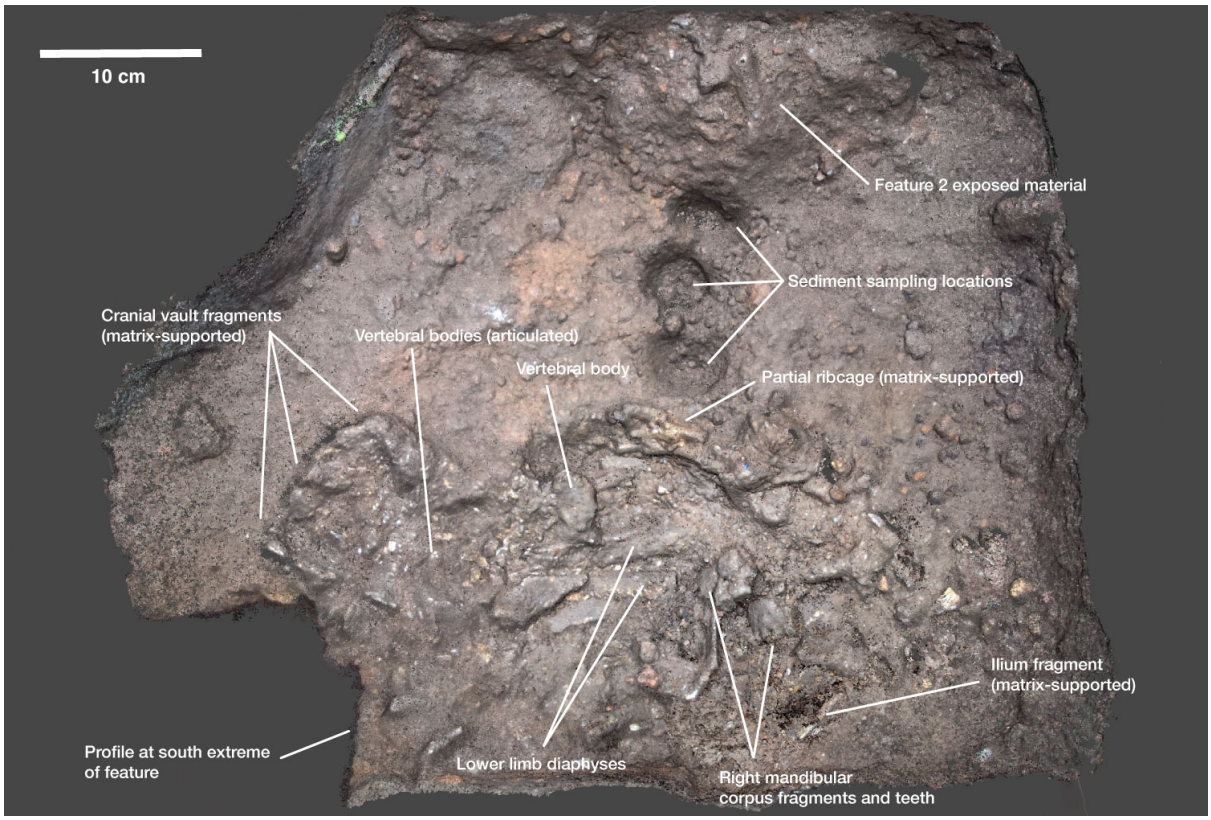

Figure 9. Surface of Dinaledi Feature 1 remaining *in situ* with identifiable elements indicated.

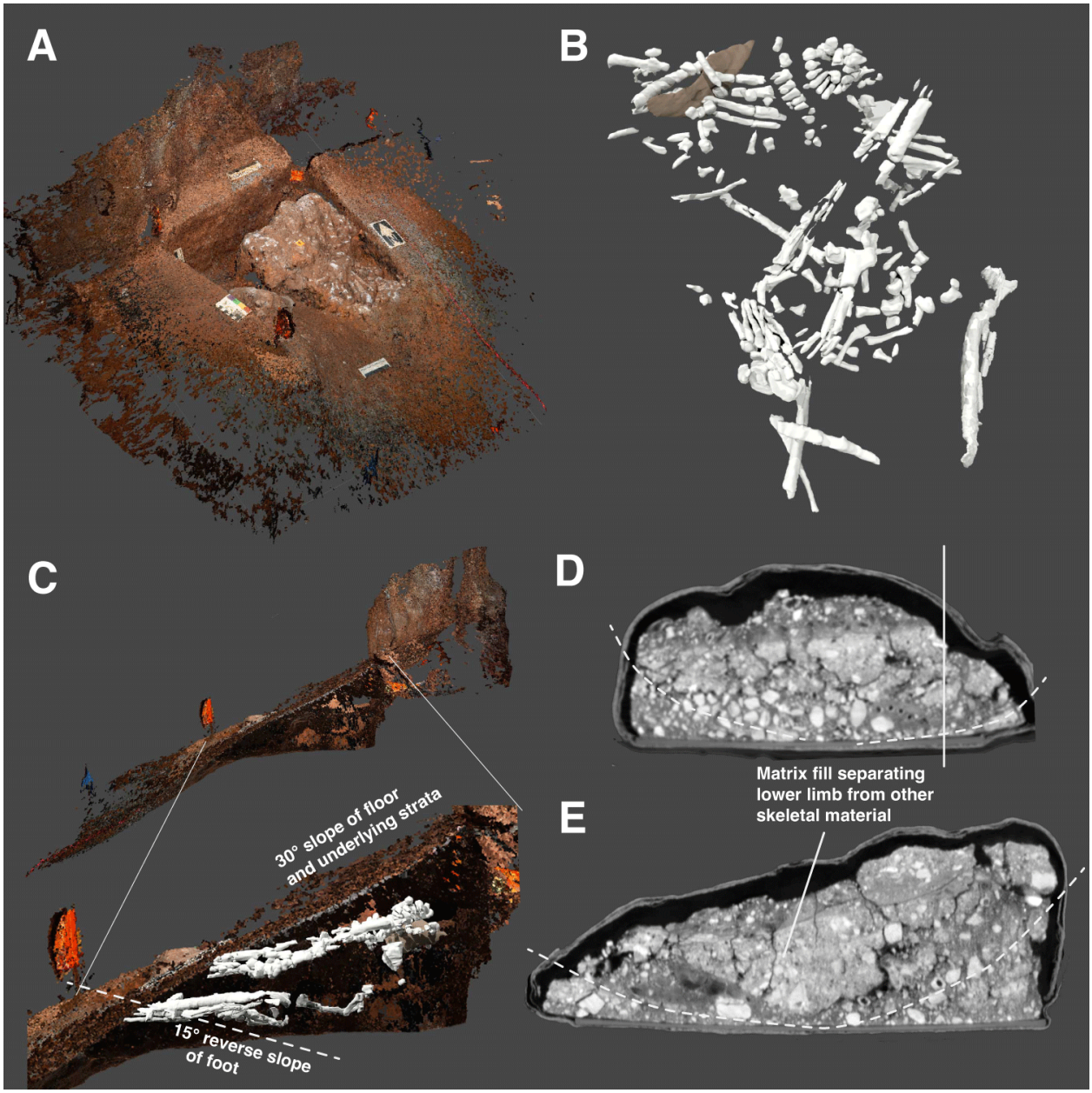

Figure 10. Hill Antechamber feature. (A) Three-dimensional rendering of Hill Antechamber feature *in situ* prior to jacketing and extraction from the cave. Bone fragments and skeletal material are exposed on the excavation surface, and the feature is pillared with adjacent sediment profiles visible. (B) Overhead view of segmented skeletal material and teeth within the feature. The complete dentition is at top of frame, and the articulated foot is visible near the bottom of the frame. The artifact is at top left, colored in a tan color, with articulated hand elements above it. (C) Three-dimensional rendering of Hill Antechamber surface slope and

profile, view from eastern side. At top, approximately 2 meters of slope and adjacent cave wall are visible, with the excavation unit at center. At bottom, the excavation unit is shown at larger scale with the skeletal material within the feature rendered. In the lowest portion of the feature, the articulated foot and leg material are emplaced at an angle opposite to the slope of the floor. Sedimentary layers here parallel the floor slope, and the leg, foot, and adjacent material cut across stratigraphy. The thoracic, upper limb, and cranial material along the top of the feature have been compressed into a plane at a shallower angle compared to surrounding stratigraphy. (D and E) Sections of CT data from Hill Antechamber feature. (D) Transverse (E-W) section, east at left. In this section the articulated foot is clearly visible near the bottom left with loose homogeneous sediment approximating the soft tissue. The dashed line delineates an internal fill, bounded by clasts and frequent voids that lie above a cut separating the fill from underlying sediment. The vertical line indicates position of section shown in E. (E) Sagittal (S-N) section, south at left. Here the longitudinal axis of the foot is visible at left, with additional skeletal material trending north. The dashed line follows the cut separating the foot and other skeletal material surrounded and supported by clasts, with some voids visible.

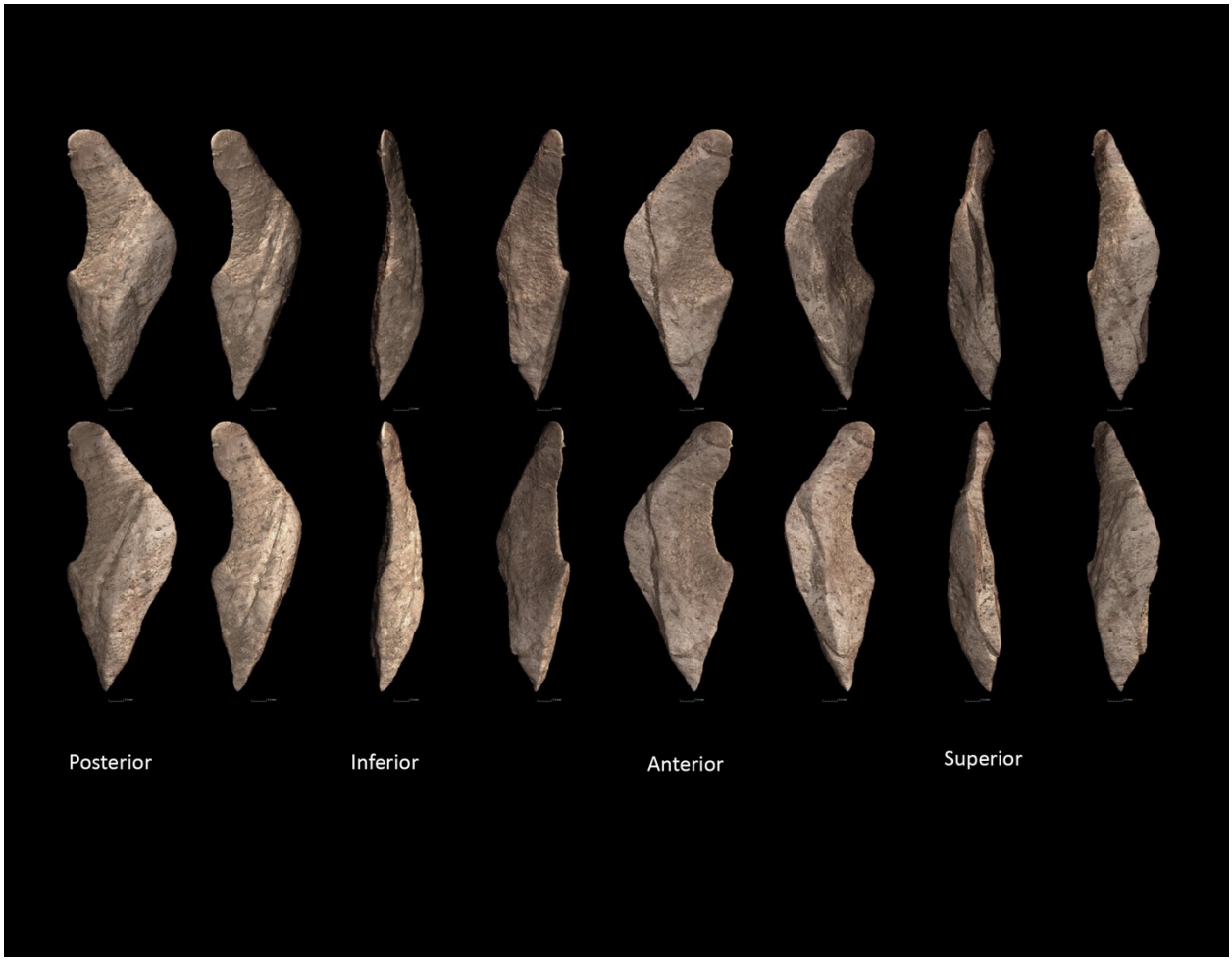

Figure 11. Hill Antechamber Artifact 1 (HAA1) showing surface from 8 different angles with 2 different lighting directions. The 3D model results from the segmentation of the synchrotron scan at 16.22um, the artifact being still *in situ* in the paster jacket.

980

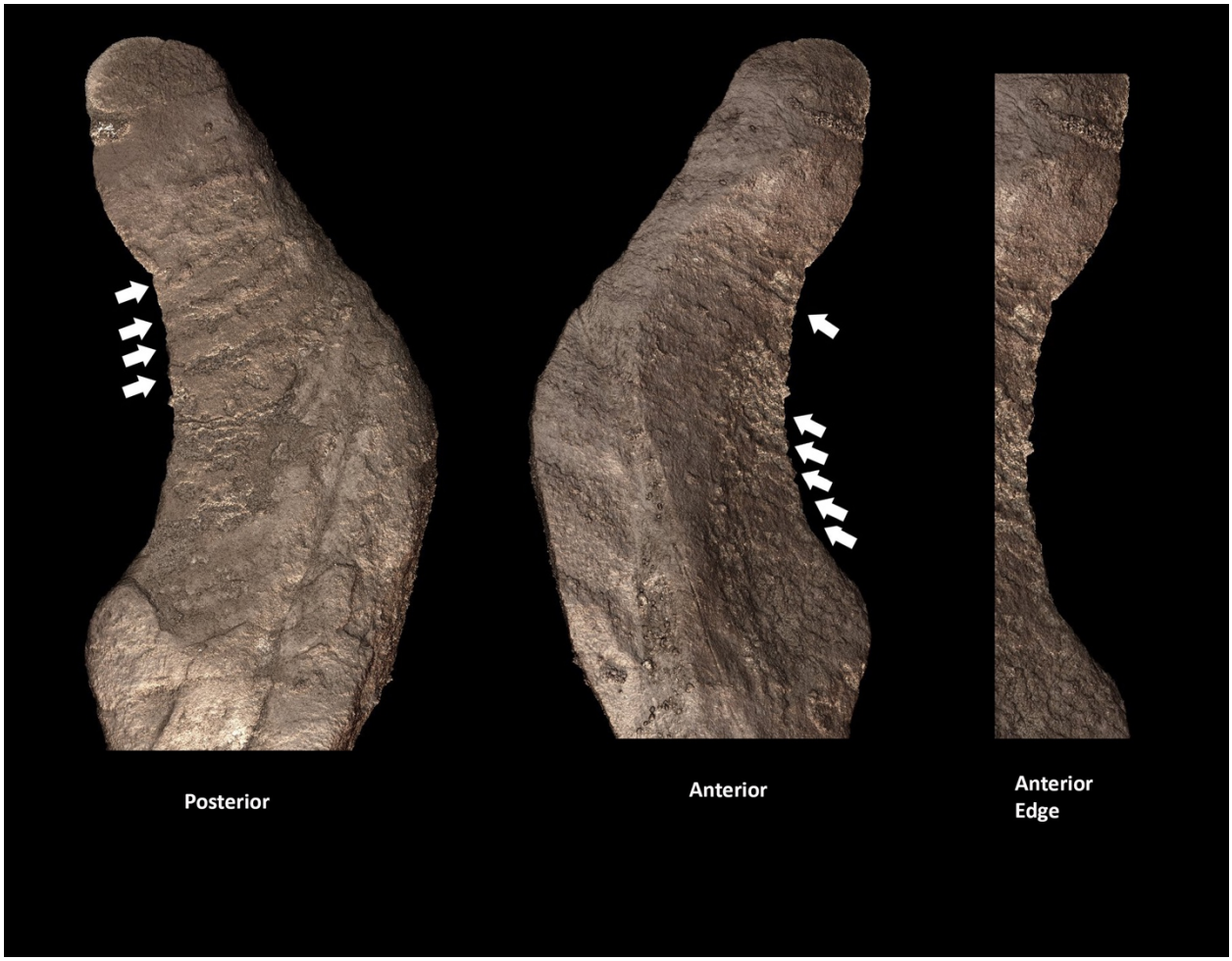

Figure 12. Hill Antechamber Artifact 1 (HAA1) close-up from the previous figure with detail showing striations visible on both faces and intersection of these striations with sharp edge of artifact showing appearance of serrations.

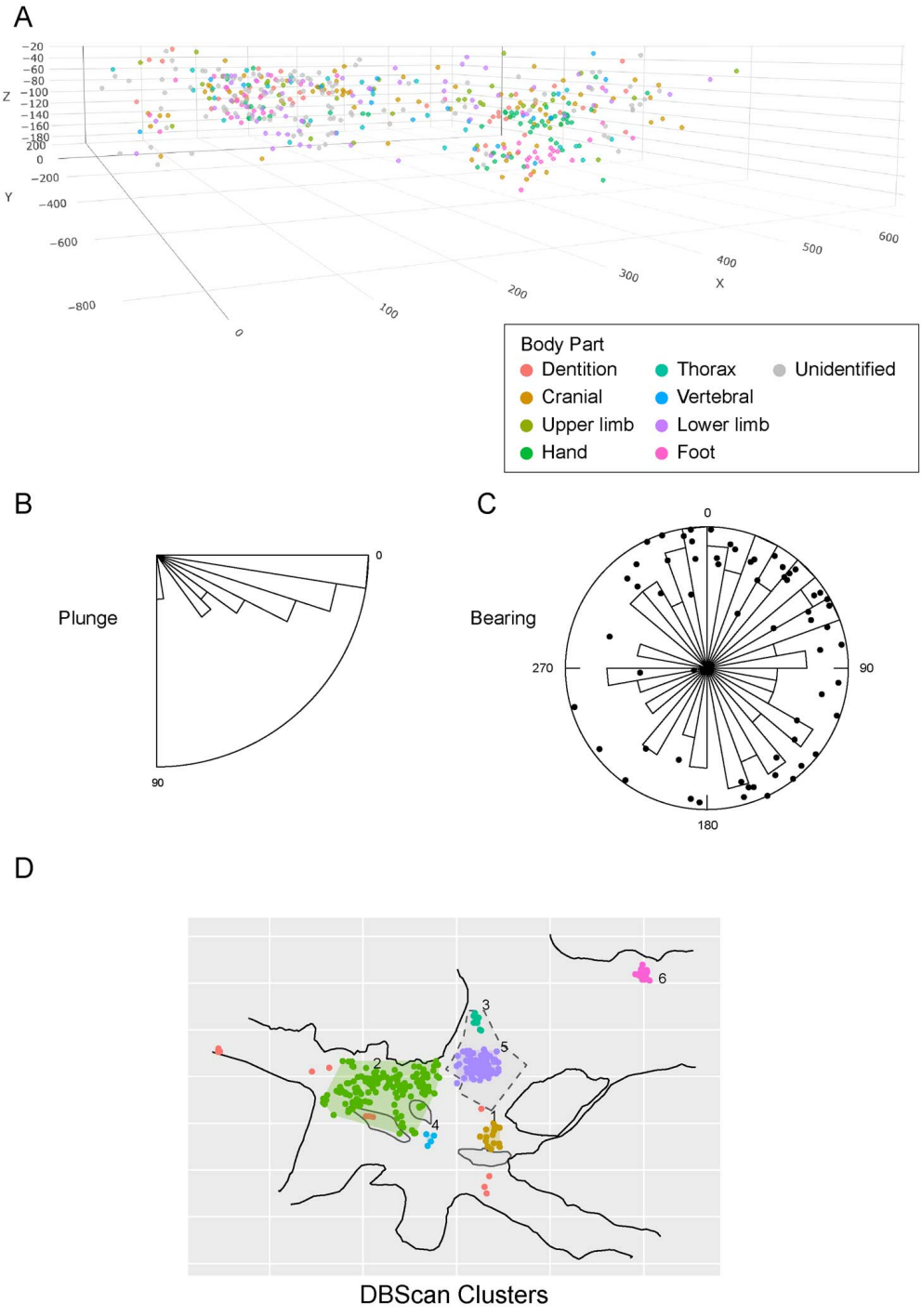

985

Figure 13. (A) Dinaledi Chamber 2013-2014 excavation data with skeletal element identifications in oblique 2.5D view. For larger specimens able to be mapped with two end points (n = 79), we calculate (B) their plunge angle and (C) planar orientation frequencies (*16*). (D) 3D density-based cluster analysis (*7*) finds that a single high density cluster comprises the majority of excavated fossils (green)

990 with two smaller peripheral clusters (purple, gold) and outliers (red points).

995

1000

1005

1010

1015

Supplementary Information: Evidence for deliberate burial of the dead by *Homo naledi*

Lee R Berger[1,2,3]*,Tebogo Makhubela[2,4]*, Keneiloe Molopyane[2], Ashley Krüger[5], Patrick Randolph-Quinney[2,6], Marina Elliott, [2,7], Becca Peixotto[2,8], Agustín Fuentes[9], Paul Tafforeau[10], Vincent Beyrand[2,10], Kathleen Dollman[10], Zubair Jinnah[2,11], Angharad Brewer Gillham[12], Kenneth Broad[13], Juliet Brophy[2, 14], Gideon Chinamatira[15], Paul H. M. Dirks[2,16], Elen Feuerriegel[2,17], Alia Gurtov[18], Nompumelelo Hlophe[19], Lindsay Hunter[20], Rick Hunter[2], Kudakwashe Jakata[14], Corey Jaskolski[21], Hannah Morris[2,22], Ellie Pryor[23], Maropeng Ramaphela[2], Eric Roberts[2,15], Jacqueline S. Smilg[2], Mathabela Tsikoane[2], Steven Tucker[2], Dirk van Rooyen[2], Kerryn Warren[24], Colin D. Wren[25], Marc Kissel[26], Penny Spikins[27], John Hawks[2,18]*

[1]The National Geographic Society, 1145 17th St NW, Washington DC, 20036

[2]Centre for the Exploration of the Deep Human Journey, School of Anatomical Sciences, University of the Witwatersrand; Private Bag 3, Wits 2050, South Africa

[3] The Carnegie Institution for Science, 5241 Broad Branch Road NW Washington D.C. 20015

[4]Department of Geology, University of Johannesburg, Johannesburg, PO Box 524, Auckland Park, 2006

[5]Department of Palaeobiology, Swedish Museum of Natural History, Box 50007, SE-104 05, Stockholm, Sweden

[6] Department of Applied Sciences, Faculty of Health and Life Sciences, Northumbria University, UK

[7]Department of Archaeology, Simon Fraser University, 8888 University Drive, Burnaby, BC, V5A 1S6, Canada

[8]The American University, 4400 Massachusetts Ave NW, Washington, D.C., DC 20016, USA

[9]Department of Anthropology, Princeton University; 123 Aaron Burr Hall, Princeton USA 08455

[10]European Synchrotron Radiation Facility, 71 Avenue des Martyrs, CS-40220 38043 Grenoble cedex 09, France

[11]School of GeoSciences, University of the Witwatersrand, Private Bag 3, Wits 2050, South Africa

[12]Frontiers Media Limited, New Broad Street House, 35 New Broad St, London EC2M 1NH, United Kingdom

[13]Rosenstiel School of Marine, Atmospheric, and Earth Science, 4600 Rickenbacker Causeway Miami, FL 33149

[14]Department of Geography and Anthropology, Louisiana State University, Baton Rouge, LA 70803, USA

[15]Evolutionary Studies Institute, University of the Witwatersrand, Private Bag 3, Wits 2050, South Africa

[16]Department of Geoscience, James Cook University, Townsville, Qld 4811, Australia

[17]Primate Evolutionary Biomechanics Laboratory, Department of Anthropology, Box 353100, University of Washington, Seattle, WA 98195-3100, USA

[18]Department of Anthropology, University of Wisconsin-Madison, Madison, WI 53593, USA

[19]Department of Anthropology, 4352 TAMU College Station, TX 77843-4352, USA

[20]Center for Academic Research & Training in Anthropogeny, UC San Diego, 9500 Gilman Drive #0140, La Jolla, CA 92093-0140, USA

[21]Synthetaic, 1309 Milwaukee St, Delafield, WI, USA

[22]ICON & Warnell School of Forestry, University of Georgia, Athens, GA 30602, USA

[23]School of Earth and Environmental Sciences, Main Building, Park Place, Cardiff, CF10 3AT, United Kingdom

[24]Human Evolution Research Institute, 3rd Floor Beattie Building, University of Cape Town, Cape Town, South Africa

[25]Department of Anthropology, University of Colorado Colorado Springs; Colorado Springs, 80918, USA

[26]Department of Anthropology, Appalachian State University; 348 Anne Belk Hall 224 Boone, NC, USA 28608

[27]Department of Archaeology, University of York; The King's Manor, York, UK, YO1 7EP

* Corresponding Authors

This file contains:

Supplementary Information 1: Petrography and geochemistry of sediments 59

Supplementary Information 1.1: Unlithified Mud Clast Breccia (UMCB) in passages of the Dinaledi Subsystem compared to UMCB on the Dinaledi floor 59

Supplementary Information 1.2. Grain size analysis of sediments around Feature 1 and the Lesedi Chamber 63

Supplementary Information 2: Hominin skeletal material and element representation 64

Supplementary Information 2.1: Identification and assessment of skeletal remains from Dinaledi Feature 1 66

Specimen list 68

Supplementary Information 2.2. Identification and assessment of skeletal remains from Dinaledi Feature 2 86

Supplementary Information 3: Hill Antechamber Feature and Artefact 87

Supplementary Information 3.1. Stratigraphic situation of the Hill Antechamber feature 87

Supplementary Information 3.2: Description of the Hill Antechamber Artefact 1 associated with the Hill Antechamber Feature 91

Supplementary Information 4: Materials and Methods 93

Supplementary Information 4.1: Previous Excavations in the Dinaledi Chamber 93

Supplementary Information 4.2. Previous work in other parts of the cave system 96

References 97

Supplementary Information: Tables 99

Supplementary Table 1. 99

Supplementary Table 2. 102

Supplementary Information: Figures 105

Supplementary Information 1: Petrography and geochemistry of sediments

Supplementary Information 1.1: Unlithified Mud Clast Breccia (UMCB) in passages of the Dinaledi Subsystem compared to UMCB on the Dinaledi floor

The petrography, specifically the mineralogy, chemistry and textures, of the *Homo naledi*-bearing unlithified mud clast breccia (UMCB) on the Dinaledi Chamber (UW101) floor was reported by Dirks et al. (2015), Makhubela et al. (2017) and Wiersma et al. (2020). Here we supplemented those results by carrying out particle-size distribution (PSD) and x-ray fluorescence (XRF) of 57 samples of the UMCB sediments collected during excavations (DF group in Supplementary Tables 1 and 1), and 22 *in situ* samples of the UMCB that is still spatially around Dinaledi Feature 1 on the Dinaledi floor (see Figure S1 and SI 4.2). The DF group samples were subsampled from bags of sediments above the burial Features 1 and 2, after sieving for recovery of fossils not recognized at the time of excavation. Each bag of sediment corresponds to a particular area and depth level of the gridded excavation pit (Figure S2). Further, we report the mineralogy, textures and geochemistry of 16 sediment samples from four fossil-bearing narrow passages of the Dinaledi Subsystem formed from W-NW, N and NW trending fracture systems (Elliott et al., 2021). These passages, namely: UW108, UW109, UW110 and UW111, are isolated locations and extremely difficult to access, and here we compare their sediments with the UMCB on the Dinaledi floor (Figure

S3). The mineralogy and chemistry were studied using x-ray diffraction (XRD) and XRF, respectively. To study the textures, we used scanning electron microscopy (SEM). The petrography of the sediments in the other fossil-bearing chambers of the Dinaledi Subsystem, namely Hill Antechamber and Chaos Chamber, have not yet been studied. But for the Lesedi Chamber we have done XRF and PSD on 3 samples of UMCB sediments on a ledge and 5 samples of UMCB sediments from the floor.

The UMCB of the Dinaledi floor is dark and uncalcified, but it is heavily cemented and does not disintegrate easily because of the very high MnO and Fe_2O_3 content, which can be more than 10 wt.% for each of these two oxides (Supplementary Table 1) (Dirks et al., 2015). The bulk geochemistry of the 57 Dinaledi floor UMCB analyzed here is consistent with the three samples analyzed by (Dirks et al., 2015). The average MnO and Fe_2O_3 contents are 4.36 wt.% and 9.88 wt.%, respectively. A sample (2280 on Supplementary Table 1) of UMCB shows the pervasive nature and abundance of MnO and Fe_2O_3 in different forms of Mn- and Fe-oxides and -hydroxides (Mn-Fe-oxihydroxide) concretionary infilling or impregnation and coatings (Figure S4). The CaO content of the Dinaledi UMCB ranges from 0.33 to 6.90 wt.%, and the element map of CaO shows that there is little CaO compared to MnO and Fe_2O_3. The average CaO content is 1.41 wt.% and it is lower than the averages of the samples from the Lesedi Chamber and the four passages of the Dinaledi Subsystem, which have 4.49 wt.% and 5.18 wt.%, respectively (see below and Supplementary Table 1).

The UW108 passage is 20-35 m wide and 5-6 m long (Figure S3), but has three varied UMCB sediments on the floor and unaltered LORM sediments on a ledge about 1.5 m above the floor. The first type of UMCB (L01) is identical to the Dinaledi floor UMCB, but shows less MnO and Fe_2O_3 content under the SEM (Figure S5). The second type of UMCB (L02) in this passage has abundant Mn-oxihydroxide occurring as discrete grains and as infilling and

coating on mud clasts (Figure S6). In addition, this UMCB contains abundant fragmentary grains of dolomite (Figure S6). In some aspects, L01 and L02 are visually different under the SEM, but chemically similar on XRF bulk chemistry (Supplementary Table 1). For example, L01 shows a high Fe_2O_3 content in the mud clasts while L02 does not, but they both have similar Fe_2O_3 content of 9.96 wt.% and 9.14 wt.%, respectively (Supplementary Table 1). The differences in the dolomite fragments can also be seen chemically where L01 has CaO and MgO of 0.62 wt.% and 2.36 wt.%, respectively, but L02 CaO and MgO of 6.10 wt.% and 7.03 wt.%, respectively (Supplementary Table 1). The third type of UMCB (L03) is a highly calcified version of L02 due to a thin (<5 mm) flowstone that partially covers the floor (Figure S7) (Elliott et al., 2021). L03 contains less mud clasts than dolomite fragments cemented by calcite, and this can also be seen chemically where MnO and Fe_2O_3 content are low (2.15 wt.% and 4.14 wt.%, respectively) but CaO and MgO are much higher (25.24 wt.% and 9.70 wt.%, respectively). The unaltered LORM mudstone from the ledge has a very fine-grained texture of clay particles that contain abundant K, Mg and Fe content but does not contain any observable Mn and Ca content under the SEM (Figure S8) (Dirks et al., 2015). The bulk chemistry of L04 is consistent with the textures (Supplementary Table 1).

The UW110 locality is parallel to UW109 in an E-W trending fracture that connects to the Chaos Chamber and is the locality where 28 cranial fragments of a juvenile *Homo naledi* were found (Figure S3) (Elliott et al., 2021, Brophy et al., 2021). At UW110 there are five observable chert horizons that are broken up and form ledges along the walls. On the floor and the ledge of the first chert unit about 0.7 m from the floor there is UMCB sediments that contain abundant metallic luster. PF01 is from the floor and contains less metallic luster than PF02 from the ledges, and this is also reflected in the bulk chemistry of these samples

(Supplementary Table 1). PF02 has the highest combination of MnO and Fe_2O_3 content of all samples analyzed, but texturally does not look different from the other UMCB sediments from the other passages and chambers (Figure S9; Supplementary Table 1). A lot of the Fe and Mn in this sample seems to be within the clay fraction of the mud clasts and not as Mn-Fe-oxihydroxide (Figure S9). On the second ledge about 1.5 m from the floor the sediments are a muddy sandstone (PFL01) unique to this area alone (Figure S10). This unit composed of mostly quartz sand with very little mud clasts, Fe and Mn (Figure S10). Interestingly, it contains abundant gypsum grains ($CaSO_4$) not seen in any other samples, making PFL01 to have a very high SO_3 content of 6.86 wt.% while in other samples it is less than 1 wt.% or undetectable (Figure S10).

The UW111 locality is almost 16 m SW of the Dinaledi Chamber where a NE-SW fracture terminates at intersection with a N-S fracture (Figure S3) (Elliott et al., 2021). In the N-S fracture passage we use to access UW111, the sediments are unaltered LORM mudstones (sample HAP1) similar to those of L04 from UW108 and they contain considerable very-fine quartz sand (Figure S11). There is no observable Mn under the SEM and in the bulk chemistry it is low at 0.95 wt.%, but Fe is noticeable in the mud clasts and is represented by 8.67 wt.% Fe_2O_3 content (Supplementary Table 1). On the floor of the UW111 locality is UMCB (HD01-03) that is partially covered by a thin flowstone like in UW108. Only HD03 has considerable CaO content of 16.79 wt.% but under the SEM it does not look calcified as the Ca seems to be in discrete grains of dolomite, and this is consistent with MgO content of 12.66 wt.% (Figure S12). The mud clasts have abundant Fe and Mn incorporated into their very fine-grained nature and not as Mn-Fe-oxihydroxide infilling (Figure S12).

There are no characteristic differences with all the major elements and loss on ignition (LOI) in terms of concentration range and averages in the geochemistry of the sediments sampled from inside Feature 1, the sterile area around Feature 1, and the sediments removed above Feature 1 (Supplementary Table 1). For example, even an element such as P_2O_5 closely linked with the fossil bone shows similar averages of 0.36 wt.% and 0.38 wt.% for the sterile sediments (SA group) around Feature 1 and the sediments removed above the Feature 1 (DF group), respectively. These two groups of samples have higher average P_2O_5 content than the sediments inside Feature 1 (SB group), between features 1 and 2 (SC group) and those from the vertical profile (SE group), which have 0.23 wt.%, 0.17 wt.% and 0.16 wt.%, respectively (Supplementary Table 1).

Supplementary Information 1.2. Grain size analysis of sediments around Feature 1 and the Lesedi Chamber

The sediments in the Dinaledi and Lesedi Chambers have similar mean grain-size centered around 350 µm and variable between 200 µm and 600 µm (Figure S13, Supplementary Table 2). The deviations from 350 µm seem to be related to the percentage sand or silt proportion of the samples, which may be linked to the proportion of the LORM mud clasts vs silt matrix of the UMCB (Supplementary Table 2). The SA and SE groups were sampled *in situ* at various depths and so their mean grain sizes show patterns of upward fining sequences (Figure S13). The DF group of samples are also from various depths of 0 to 15 cm, but the sediments of each sample were mixed during sieving. They show a mixture of upward and downward fining sequences.

Supplementary Information 2: Hominin skeletal material and element representation

In this section we present a preliminary identification of skeletal elements within the burial features, with an assessment of skeletal part representation. We note the presence of articulated or spatially contiguous elements where this has been observed.

In both the Dinaledi and Hill Antechamber, we have left much of the evidence described here *in situ* or *en bloc* without unnecessary destructive excavation or preparation. The skeletal material that has been excavated from Dinaledi Features 1 and 2 has not been subjected to solvents or consolidants at this time. The Hill Antechamber feature rests within three plaster-jacketed blocks at the present time. These decisions limit the number of observations that we can gather on the skeletal remains from these features. Here it is worth a brief comment to clarify these protocols and discuss their relevance to the study of the burials.

Archaeological controlled excavation is a fundamentally destructive process (*17*), one in which the spatial relationships between buried objects (including hominin fossils) is lost once the matrix surrounding such remains is disturbed and the buried objects lifted. Spatial relationships are necessary to determine temporal relationships in archaeological settings; they are also fundamental to understanding the processes of alteration that assemblages may have undergone after burial. Article 5 of the International Charter for Archaeological Heritage Management states that archaeological investigations can be carried out using a wide array of methods from non-destructive remote sensing, through sampling, to total excavation. It is widely recognized that total excavation is a recourse that should be adopted after consideration of other less destructive means of study (*18*).

3D modeling or non-invasive imaging is the preferred method for recording and understanding fragile, friable buried contexts where the precise spatial relationships between clastic components is considered more important rather than the necessity to view the surface morphology of such remainsi. Such a spatially-based approach has been used and advocated in recording of mainstream archaeology (*19*), cremains (*20*), bone taphonomy (*21*, *22*), 4D documentation of pit burials (*23*), virtual autopsy (*24*), recording fragile funerary goods and human remains (*25, 26*), through to whole burial chambers (*27*), where information derived from the spatial relationships within the burial environment outweighs that from direct analysis of the bones or artefacts themselves (*28*).

In the Rising Star cave system we have employed study protocols that minimize the extent of excavation areas and maximize the collection of spatial data by multiple modalities (*1, 5, 9, 11*). The total excavation surface in the Dinaledi Chamber to date is 1.55 m^2 and in the Hill Antechamber is 0.75 m^2. *Homo naledi* skeletal and dental material has come from these excavated areas and from collection of skeletal remains from the floor surfaces of these chambers. That material now numbers more than 2500 pieces, many of them small fragments but including a large number of complete and well-preserved elements. Nonetheless much of this skeletal material is highly fragile with loss of elements with thin cortical bone or substantially trabecular bone content. Our excavations in 2013 and 2014 in the Dinaledi Chamber identified buried skeletal material with articulated limb, cranial, and vertebral elements (*5, 6, 11*) including portions that could be attributed based on spatial and developmental data to a partial juvenile skeleton (*8*). This extensive evidence of skeletal morphology and spatial positioning of material has informed our more recent work in the system in a variety of ways (*1*).

In many paleoanthropological contexts, the recovery of morphological or developmental observations on hominin skeletal material is a very high research priority. Additionally, some settings pose taphonomic questions that can be addressed only through collection of data from bone surfaces. To recover such data, hominin skeletal material has often been subjected to intensive preparation, cleaning, and consolidation. Much *Homo naledi* skeletal material from our earlier work has been treated with conventional methods of skeletal conservation and analysis, which has included microscopic examination of bone surfaces (5). Having this published evidence in hand gives us the possibility of taking a less destructive approach to studying the burial features that we identified in subsequent work. For these reasons, once we identified a high probability that the Dinaledi Feature 1 and Hill Antechamber Feature were burial contexts, we planned for non-destructive methods to record and preserve the spatial relationships between any remains entombed within these features. In the Hill Antechamber case, this involved lifting the feature en bloc for study, scanning, and possible preparation in the laboratory. In the case of Dinaledi Feature 1, the prior recovery of a similar burial feature from the Hill Antechamber argued for leaving this feature in situ within the cave system and recording data on its spatial and sedimentary context noninvasively.

Supplementary Information 2.1: Identification and assessment of skeletal remains from Dinaledi Feature 1

Here we list brief anatomical identification of all catalogued skeletal elements and fragments excavated within and above the area of Feature 1. These specimens all come from grid units S950W550 and S900W550. Some other material excavated from unit S900W550 is associated with Feature 2 and these are listed separately below.

These brief identifications do not focus on comparative morphology beyond the identification to element where possible. Many of the remains are small fragments that are not identifiable to element and these are included here to present a complete record. In the few cases where diagnostic morphology of *H. naledi* is present, this is indicated. Where evidence for developmental stage is present, this is indicated.

We have not fully cleaned sediment from this skeletal material or applied fixatives or other chemicals, in anticipation of possible analysis of biochemicals or trace evidence. This precludes a full examination of possible surface modifications or other surface taphonomy.

Nearly all elements identified in this list are compatible with belonging to a single adult individual. All identifiable adult elements are size-compatible; they do not appear to represent a mixture of individuals of different sizes. None of the adult elements duplicate each other; nor is there any duplication with identifiable elements that remain *in situ* within Feature 1 in the Dinaledi Chamber.

There are three notable exceptions that are immature elements and inconsistent with the single adult represented by the rest of this material. Two of these are fragments of juvenile femur, including the right proximal femur fragment included in U.W. 101-2250 and a fragment of femur shaft U.W. 101-2260. These two elements were excavated overlying and in physical contact with the bone concentration of Feature 1, both within 5 cm of each other near the center of the feature. The proximal right immature femur duplicates the proximal right adult femur fragment, also included within U.W. 101-2250. These two elements were excavated in immediate contact with each other with the immature femur fragment overlying the adult fragment. The other inconsistent element is an immature proximal left humerus fragment, U.W. 101-2243. This element duplicates another proximal left humerus within Feature 1, U.W. 101-2231. These two elements contrast in developmental status, with U.W.

101-2243 having evidence of an unfused proximal epiphysis and U.W. 101-2231 compatible with adult status. The two elements are also in different situations relative to the feature: U.W. 101-2231 is near other compatible humerus and upper limb material at the south end of the feature, while U.W. 101-2243 was out of anatomical placement overlying the uppermost part of the north side of the feature. We interpret these three fragments of immature elements as bone fragments that were on the surface or within pre-existing deposit that comprised the sediment fill of Feature 1.

Specimen list

U.W. 101-2114

Thin plate-like bone fragment, broken on all edges, less than 15 mm.

U.W. 101-2115

Two cranial bone fragments. One is possibly zygomatic or root of zygomatic arch on temporal, length 23.8. The other is possibly zygomatic at orbit, or frontal above orbit, bone surface is concave and slightly wavy. Preserved size 16.5 x 16.5.

U.W. 101-2116

Phalanx fragment with adhering clump of sediment. Fragment size is 18.9 x 9.0

U.W. 101-2117

Right proximal radius fragment. The head is present but broken around the visible edge, and one side is still obscured by sediment. The bone is very comparable in size with U.W. 101-2246 and they may be antimeres. 38.8 mm length

U.W. 101-2118

Two bone fragments less than 15 mm

U.W. 101-2119

Bone fragment less than 15 mm

U.W. 101-2120

Two cranial bone fragments less than 20 mm

U.W. 101-2121

Right proximal radius fragment, representing nearly the entire circumference of the bone. The head is not present. The distal break on this fragment is consistent with the break at one end of U.W. 101-2240 and may be the same bone. Preserved length 49.6. Shaft diameter 10.0 x 9.4.

U.W. 101-2136

Cranial or mandibular fragment, possibly zygomatic arch. Length 20.4

U.W. 101-2137

Three large clumps of sediment with spongy bone fragments embedded within them. Possibly distal femur or pelvic.

U.W. 101-2138

Sediment clump with embedded bone fragments. ca. 15 mm

U.W. 101-2139

Sediment clump with embedded fragments of cortical bone. ca. 15 mm

U.W. 101-2140

Tooth root. 11.5 mm

U.W. 101-2141

Tooth root. 13.2 mm.

U.W. 101-2142

Cortical bone fragment, 16.0 mm.

U.W. 101-2143

Three bone fragments less than 15 mm.

U.W. 101-2144

Mandibular incisor. Probably left I1, possibly I2. Occlusal wear is extensive and remaining crown height above cervix on distal face is only 2.2 mm. The wear is at an angle of approximately 60 degrees compared to labial face. The wear has exposed dentin with MD 2.0 mm, LL 1.3 mm. LL breadth 5.9, MD 4.6. Root is nearly complete with small section of distal tip missing due to fracture.

U.W. 101-2145

Bone or dentin fragments, less than 5 mm, with some sediment.

U.W. 101-2146

Bone fragments in sediment clump, less than 10 mm.

U.W. 101-2147

Bone fragment with large cancellous structure in sediment clump. Less than 20 mm.

U.W 101-2148

Two bone fragments with sediment adhering. Smaller fragment 13.0, larger 21.3.

U.W. 101-2168

Sediment with bone fragments less than 5 mm.

U.W. 101-2170

Tibia shaft portion, 121 mm in length, represents midshaft. Consistent with adult. Diameter at point where posterior shaft flattens is 21.4 x 17.2. Other small shaft fragments, all less than 20 mm.

U.W. 101-2171

Long bone shaft fragment, 34.3 x 10.4

U.W. 101-2172

Fourteen long bone shaft fragments. Most represent a part of the bone circumference and are between 30 and 40 mm in length, 10-15 in width. Additional fragments in bag.

U.W. 101-2173

Two bone fragments less than 15 mm.

U.W. 101-2174

Mandibular fragments. Two tooth crowns are present with their roots, and three additional root fragments. The two crowns are both left mandibular molars. One is markedly more worn, with large dentin pools at protoconid and endoconid, and metaconid is entirely fragmented away. The rest of the enamel rim has large fragments missing. BL 11.1 MD 12.1. This tooth has a distal interproximal facet, I interpret it as an M2. The other tooth is worn approximately flat with dentin exposed on mesial four cusps. BL 10.8 MD 12.1. This tooth is more triangular in shape distally and does not have an interproximal facet distally; I interpret it as an M3. One of the broken root fragments is a molar root, the others appear likely to be premolar roots. The morphology and dimensions of these teeth are compatible with *H. naledi*.

U.W. 101-2175

Lower left fourth premolar. Root is largely intact, broken at tip. Single root. Enamel is worn flat with large dentin pools for both buccal and lingual cusps. BL 10.7, MD 9.2. The morphology and size of this tooth are compatible with *H. naledi*.

U.W. 101-2176

Lower left third premolar. Two roots, both intact. BL 10.6, MD 9.4. Crown is worn flat, dentin exposed at protoconid and metaconid. This tooth possesses diagnostic anatomy for *H. naledi*.

U.W. 101-2177

Ulna shaft portion, 48 mm.

U.W. 101-2178

Two fragments. One is fibula shaft, 37.5 mm. The other is a flat fragment less than 20 mm.

U.W. 101-2179.

Bone fragment, possibly tarsal, maybe medial cuneiform fragment. Two additional pieces are bone fragments less than 10 mm.

U.W. 101-2180

Distal ulna shaft fragment, 44.6 mm.

U.W. 101-2181

Cranial fragment consistent with right zygomatic bone including orbital border. 34.8 x 24.7 mm.

U.W. 101-2182

Fibula or metacarpal shaft portion, 27 mm

U.W. 101-2183

Radius or humerus shaft portion 43.6 mm. Additional fragments of shaft.

U.W. 101-2184

Base of right mandibular corpus. 52.5 mm.

U.W. 101-2185

Enamel fragment, 5 mm.

U.W. 101-2186

Enamel fragment, corresponding to rim of molar, 8.9 mm

U.W. 101-2187

Tooth root fragment, 10.1 mm

U.W. 101-2188

Cranial vault fragment. One side is obscured by sediment. 21.4 x 15.4 mm, 5.4 thick.

U.W. 101-2189

Mesial part of mandibular molar, with mesial root complete. Very little enamel on this crown. This looks like a mirror image of the U.W. 101-2174 M3 mesial root. Several additional cranial or mandibular fragments, mostly less than 20 mm.

U.W. 101-2190

Fragment of humerus head, with small slice of surface 22.0 x 8.3 mm.

U.W. 101-2191

Partial phalanx, probably manual intermediate phalanx. Proximal articular surface is eroded but present, shaft 16.5. Embedded in sediment chunk.

U.W. 101-2199

Phalanx shaft portion, or possibly fibula shaft portion. 23.5 mm.

U.W. 101-2200

Fibula shaft or metatarsal shaft portion, triangular cross section. 22.6 mm

U.W. 101-2201

Three bone fragments, with some articular surfaces.

U.W. 101-2202

Bone fragment, shaped like possibly zygomatic or mandibular fragment, seems too thick to be vertebral or rib. 22.7 mm length.

U.W. 101-2203

Shaft fragment consistent with metacarpal. Length 28.5, diameter 5.9 x 5.2.

U.W. 101-2204

Bone fragment. 25.8 long, 14.8 broad, 6.8 thick.

U.W. 101-2205

Long bone shaft fragment, based on size and curvature consistent with humerus, representing approximately 40% of the circumference. Length 43.5, width 13.3.

U.W. 101-2206

Bone fragment, one side exposed trabeculae, the other rough cortical surface. Possibly distal femur or ilium. 24.5 x 17.9

U.W. 101-2207

Metatarsal or manual phalanx shaft fragment. 23.6 long, 7.9 x 5.3 near base.

U.W. 101-2208

Long bone shaft fragment, based on size and curvature probably humerus, representing 30% of the circumference. 25.4 x 13.9.

U.W. 101-2209

Long bone shaft fragment, based on size and curvature probably humerus, representing 30% of the circumference. 29.1 x 11.4.

U.W. 101-2210

Bone fragments, probably cranial, less than 30 mm.

U.W. 101-2211

Rib fragment. 34.3 long, diameter 8.6 x 6.1

U.W. 101-2221

Bone fragments.

U.W. 101-2222

Cranial vault fragment. 22.4 x 14.8.

U.W. 101-2223

Long bone fragment. 38.7 x 13.0

U.W. 101-2224

Left distal humerus fragment. The lateral supracondylar crest is well preserved and evident. Length 54.4.

U.W. 101-2225

Long bone shaft fragment with rounded circumference compatible with humerus or radius, including 50% of shaft circumference. 29.9 long, 12.0 wide.

U.W. 101-2226

Flat long bone shaft fragment. Consistent with distal humerus or proximal tibia. 38.5 x 15.8.

U.W. 101-2227

Long bone shaft fragment consistent with humerus. 29.1 x 15.1

U.W. 101-2228

Shaft fragment consistent with small long bone, metacarpal or metatarsal. 21.3 x 9.5

U.W. 101-2229

Long bone shaft fragment consistent with radius, ulna, or fibula. 27.4 x 10.2

U.W. 101-2230

Bone fragments in sediment.

U.W. 101-2231

Proximal left humerus shaft. Length 53. Diameter at surgical neck 18.2 x 15.8. A chip of enamel is adhering within the sediment that fills the proximal end of this fragment. The

enamel chip is approximately 3 mm x 5 mm and could be molar or incisor. A second fragment refits the distal end of the first. Length 24.8 x 13.7.

U.W. 101-2232

Bone fragment 19 x 9 mm.

U.W. 101-2233

Bone fragment 18.7 x 12.8.

U.W. 101-2234

Bone fragment 20.6 x 8.4.

U.W. 101-2235

Tooth root, slightly bilobate toward crown. 15.1 mm.

U.W. 101-2236

Bone fragment with concave surface exposed on one side, other side trabecular fragments with sediment obscuring detail. 21 x 17.

U.W. 101-2237

Maxillary left molar. BL 12.3, MD 11.6. All roots are present and intact, all three curve distally, and the buccal two roots curve into each other strongly distally. Based on roots and crown morphology this resembles an M3 more than either other molar. The crown is bigger

than any of the M1s and those teeth do not have the posteriorly directed lingual root that this one has. Occlusal surface has slight wear, no dentin exposure and all cusps are salient.

U.W. 101-2238

Mandibular ramus fragment of right coronoid process. 35.9 x 14.8.

U.W. 101-2239

Shaft fragment of femur or tibia, relatively flat, consistent in size and thickness with U.W. 101-2259 femur. Length 48.3, width 19.4.

U.W. 101-2240

Shaft portion of radius or ulna. 43.1 long, diameter obscured by sediment. This fragment is consistent with the break at the distal end of the U.W. 101-2121 radius fragment and may be the same bone. A small thin and slightly rounded bone fragment was adhering to one end, not in anatomical position. This is thinner than the shaft fragment and probably belongs to some other bone.

U.W. 101-2241

Bone fragment, thin with adhering sediment on one side. 19.9 x 13.6

U.W. 101-2242

Proximal right ulna, lacking olecranon process. Length 50.2, diameter below coronoid process 12.9 x 12.4. Two additional shaft portions refit the larger fragment.

U.W. 101-2243

Proximal left humerus shaft. The proximal end of this includes a small portion of metaphyseal surface across the lateral 25% of this end of the bone. There is additionally a small (10 mm) piece of epiphysis that was adhering in position to part of this lateral edge of the proximal end. This is now detached and its surface does correspond to the opposing surface of the diaphysis. Length 46.7. Shaft diameters at surgical neck 18.5 x 15.5.

U.W. 101-2244

Proximal end of a rib with the articular part of the head missing but the tubercle present. The neck is round in cross section and the break just lateral to the tubercle has a rib-like cross section. I tend to think this is left mid- to upper thorax. Length 25.9, diameter 6.3.

U.W. 101-2245

Bone fragment consistent with vertebral lamina. 13.3 x 9.3 x 5.6 thick at thickest point.

U.W. 101-2246

Proximal left radius, lacking head. Radial tuberosity and approximately 25% of shaft are present. The neck is broken and does not preserve an metaphyseal surface. It is size-consistent with adult material. That makes it comparable to the humerus elements nearby including U.W. 101-2243. Length 55.7, diameter of neck 10.1 x 9.2.

U.W. 101-2247

Phalanx or rib fragment. 20.6 x 8.2 x 4.9.

U.W. 101-2248

Rib fragments less than 20 mm.

U.W. 101-2249

Right distal humerus, lacking trochlea and capitulum. Length 88. Diameter above epicondylar ridges 14.1 x 15.7.

U.W. 101-2250

Long bone remains that represent at least two different elements. One of these is a right proximal femur, including base of neck, lesser trochanter, broken below greater trochanter. Subtrochanteric diameters AP 20.9, ML 28.5. Length of fragment 68.4. A second large fragment is a portion of long bone shaft, 62.5 long, 16.0 in diameter. The cortical bone is thin relative to the shaft diameter, suggesting that it is more consistent with juvenile femur or tibia rather than adult humerus. In size, this shaft fragment may be compatible with the immature proximal femur fragment U.W. 101-2260 but there is no refit between these pieces. This bone is highly dark stained with iridescent sheen and edge, it has the appearance of burned bone. Smaller additional fragment of same 27.3 x 14.0. Additional bag contains bone fragments in sediment.

U.W. 101-2258

Rib fragment 23.1 long.

U.W. 101-2259

Femur shaft. Refits right proximal femur in U.W. 101-2250. Fracture is stained, not fresh. Length 152.9. Diameter same as 101-2250.

U.W. 101-2260

Immature proximal right femur. Includes neck, head is missing. It is possible that the metaphyseal surface for head is present here but sediment and possible erosion mask whether this is the case. The metaphyseal surface for the greater trochanter is partially present. None of the head is present, and the broken portion of the neck does not retain any of its metaphyseal surface. Lesser trochanter is projecting, shaft is broken away irregularly and lateral border of shaft missing. Fragment 41 mm, neck 19.6 x 15.1.

U.W. 101-2261

Fragment with concave surface on one side, convex obscured by sediment on the other. Fragment 19.7 x 15.2 x 6.6 thick.

U.W. 101-2262

Long bone shaft fragment, ulna. 39 x 13.4.

U.W. 101-2263

First metacarpal head and 40% of shaft. Includes diagnostic morphology of *H. naledi.* 28.5 mm.

U.W. 101-2264

Shaft fragment of phalanx or metacarpal. 25 mm x 8.1 mm.

U.W. 101-2265

Bone fragment, possibly carpal fragment less than 15 mm.

U.W. 101-2266

Bone fragment, less than 20 mm.

U.W. 101-2267

Bone fragments within clump of sediment, possibly rib fragments, 32.7 mm.

U.W. 101-2268

Bone fragment, possibly rib fragment, 25.4 x 9.4.

U.W. 101-2269

Bone fragment with morphology and possible metaphyseal surfaces, possibly immature long bone fragment? 18.4 mm.

U.W. 101-2270

Bone fragments

U.W. 101-2271

Bone fragment less than 20 mm.

U.W. 101-2272

Long bone fragment 25.2 x 16.6 x 6.9 thick.

U.W. 101-2273

Shaft fragment of long bone, 28.5 x 17.4. Other associated fragments.

U.W. 101-2274

Manual phalanx. Head is eroded, base is missing. Probably proximal phalanx based on length. 28.0 mm long, diameters at midshaft 8.8 x 4.9.

U.W. 101-2275

Ischium fragment including lunate surface of acetabulum, broken superior to ischial tuberosity. 25.0 x 13.0 mm of lunate surface present. Fragment length 21.1 from acetabular border to inferior edge. Subacetabular sulcus 6.9 mm.

U.W. 101-2276

Mandibular corpus fragment, including the angulation between the base of the corpus and either the external or internal surfaces. Based on curvature this seems likely to be external. This fragment is possibly consistent with U.W. 101-2184, which is clearly right mandibular

corpus including the base and the swelling at the base of the ramus. Fragment dimensions 36.5 x 13.5.

U.W. 101-2277

Shaft portion of ulna or fibula. Length 37.3, diameter 9.9 x 9.4.

U.W. 101-2278

Left proximal ulna with shaft fragments. Olecranon process is present but eroded, coronoid process appears to be broken or missing. The coronoid process is certainly missing because of a break. This is consistent with adult ulna due to the extent of the olecranon process that remains without evidence of metaphysis, but its most proximal extent is abraded. Measurements below coronoid 11.9 x 11.5. Length 47.6.

Supplementary Information 2.2. Identification and assessment of skeletal remains from Dinaledi Feature 2

Very little skeletal material has been excavated from or above Dinaledi Feature 2. The feature remains largely undisturbed, with only a small semi-circular concentration of bone visible and an unknown portion remaining within the unexcavated S950W600 grid square. The identifiable elements are consistent with a single adult individual but very little evidence has been recovered to date.

U.W. 101-2134

Bone fragment, thin cortical flake, 13.9 mm

U.W. 101-2135

Bone fragment consistent with cranium or mandible, 12.7 mm

U.W. 101-2166

Bone fragment consistent with cranium or mandible, 34.9 x 20.9 mm.

U.W. 101-2167

Bone fragment in sediment, possibly phalanx shaft. Less than 20 mm.

U.W. 101-2198

Flat thin fragment consistent with zygomatic arch or vertebral lamina. 15.2 x 7.4.

U.W. 101-2220

Femur or tibia shaft portion. Surface morphology and cross-section obscured by sediment. Length 80.7, diameter 24.9 x

Supplementary Information 3: Hill Antechamber Feature and Artefact

Supplementary Information 3.1. Stratigraphic situation of the Hill Antechamber feature

During the course of excavation, it was possible to make a number of observations about the sediments and stratigraphy of the units surrounding the feature. The sediment is a brown color with a fine texture similar to that encountered in the Dinaledi Chamber (*5*)

(Figure S24), with laminated orange-red mud (LORM) clasts present within the sediment. The sediments along the north wall of the N50W50 and N50W100 units were loose in texture and with few large clay clasts. Around 5 cm from this north wall, LORM clasts became more frequent, and sediment is more indurated. Toward the south within these units, this LORM forms layers, from a thin veneer to 2 cm in thickness. This layering is visible in profile on the east wall of the present excavation (Figure S25). The layers are roughly parallel with the north-south slope of the floor surface of the chamber. The west wall of the excavation is dominated by a large dolomite boulder that remains in place. South of this boulder the layering is present and similar in orientation to the east wall, although not exhibiting as prominent contrasts in coloration. To the north of the boulder, clay clasts are less frequent, and the profile is similar to the north wall of the excavation area. Finally, the sediments to the south of the feature extend downslope from the feature itself. Our excavation of the S50W100 and S50W50 grid squares identified the southern boundary of the feature and excavated downward approximately 15 cm to leave a vertical wall representing the sediment profile immediately against the feature itself. This wall revealed a layered profile with alternating reddish clay layers, similar to the east wall of the excavated area (Figure S25). The upper 10 cm of this wall exhibited horizontal layering, and in the lowest 5 cm this layering transitioned into a subhorizontal slope becoming a 20 to 30 degree slope running downward from east to west. These lower layers were continuous further to the south where they are visible in the excavated horizontal surface at the base of the S50W100 and S50W50 units.

The stratigraphic situation of the feature itself can be examined directly from CT data as well as from the excavation record (Figure S26). LORM clasts are highly visible in the CT images due to their higher density than surrounding sediment; their near-uniform density and

irregular shapes make them easily distinguished from fossil material. Clay clasts occur sporadically throughout the feature. More of these clasts occur in the lower half of the feature on the eastern edge. Here they are arranged in layers that have a slope similar in orientation that seen in the surrounding sediments. These layers do not characterize the rest of the feature. Instead, most of the volume of the feature is poor in clasts and rich in fossil material and sediment. This fill has a shallow bowl-shaped bottom that is marked by clay clasts and frequent voids. For example, a jumble of clasts and voids is evident in east-west transverse sections at 50% and 60% of the feature's length (Figure S27), which contrast with the homogeneous, higher density sediment above this bowl-shaped bottom. Excavation records show that voids were also noted during the excavation at the bottom of the feature, as we worked to define the edge of the feature. These voids were air-filled, not filled with lower-density sediment. With this fill, we face the key question of whether the fill is stratigraphically above an existing layer or whether it cuts through layers, interrupting them . In the transverse CT sections from 10% to 20%, the layering is indistinct due to the relative lack of LORM clasts. In the section at 30%, a well-defined layer slopes from the east edge of the block continuously down to the bottom without interruption. Further to the south, from 40% up through 60% of the feature's length it is evident that the bowl-shaped bottom of the feature fill interrupts the more layering that is seen at the easternmost part of the feature. The layering near the lower east side of the feature is less easily visible in the north-south sagittal sections, but also appears to be interrupted by a jumble of clasts and voids in the sections from 30% to 60% where the layering no longer appears.

This bowl-shaped interface of the feature lies immediately below several fossil specimens including an articulated right foot and ankle. It is notable that these articulated elements are surrounded by a halo of sediment with lower density than the surrounding fill;

additionally, some small voids occur immediately above this articulated foot (Figure S29). The lower boundary of this fill is less clearly defined near the north edge of the feature, due to the lower number of clay clasts, however this fill still contains fossil material including a partial articulated hand and upper limb material, as well as the stone artifact. In north-south sagittal sections, the bowl-shaped lower border of the fill is also evident. Near the center of the U.W. 101-2076 block, the bowl reaches the bottom of the block itself and the orientation of the articulated foot suggests that the volume of fill likely extended slightly below the excavation boundary of this block. The excavation records provide additional context for this observation. After the removal of the feature, a short remnant of the sediment pillar remained, which the team excavated to bring to the same level as the surrounding excavation units. Near the center of the feature was an oval of bright orange LORM (Figure S30). This bright orange LORM patch was also evident within the bottom surface of the feature after inverting it, prior to jacketing (Supplementary Figure S30), and the portion remaining in the site was less than 1 cm in thickness. Further excavation revealed a very dark layer of sediment, looser and with a less compact texture, of 0.5–1 cm thickness, giving way to more typical brown sediment below. A small number of fossil fragments were recovered from this area after the removal of the jacketed blocks. These areas suggesting a textural and color contrast were localized beneath the lowest portion of the bowl-shaped contrast within the feature itself.

While this fossil-containing sediment fill makes up the majority of the feature's volume, the uppermost aspect of the feature is a sub-horizontal layer that follows a northeast-southwest slope of approximately 10 degrees. This slope is at variance with the slope of the layering present around the feature, which is principally east-west and a steeper northeast-southwest slope. It does not correspond to the bowl-shaped bottom of the fill within the feature, and it does not correspond to the orientation of the articulated foot, stone artifact, or

other material present within this fill. This sub-horizontal layer is composed entirely of fossil material. This material includes complete elements in articulation, in near-articulation, or in anatomical positioning relative to each other. It is this layer that defined our excavation of the feature, and it therefore extends to the edges of the blocks we recovered. The skeletal material itself is described below. From the perspective of stratigraphy, this uppermost portion of the feature was clearly defined relative to overlying sediment. The undistorted and complete elements within this layer are small compact elements including the upper and lower dentition of a single individual, carpals, metacarpals, and phalanges. Ribs and upper limb long bones are present within this layer, in relative anatomical order, and all exhibit crushing and flattening. The demi-mandible containing part of the lower dentition also is crushed with small bone fragments separated from each other by matrix-filled gaps. A large mass of undifferentiable bone material occurs near the north end of the feature; the proximity of this large mass near the upper and lower dentition and partial mandible suggests that this is the crushed remains of a calvaria. It is evident from the crushing of cortical bone of long bone shafts and mandible, and the complete flattening of a calvaria, that this upper body was subject to gravity and possibly additional mechanical forces that flattened it, distorting its original depositional situation into a sub-horizontal layer.

Supplementary Information 3.2: Description of the Hill Antechamber Artefact 1 associated with the Hill Antechamber Feature

The Hill Antechamber Artifact 1 (HAA1) is a stone located near articulated hand bones in the feature. This is the only stone greater than centimeter size evident within the feature. HAA1 still remains within the larger plaster jacket containing most of the Hill Antechamber feature. Examination of the CT data revealed this stone in close contact with the articulated bones of a *Homo naledi* hand, and we prioritized obtaining higher-resolution

scan data of the stone to evaluate its morphology, as described in SI 1.3. This section presents a description of the artifact. Orientation is described based on an arbitrarily defined position of features illustrated in Figure 11. All measurements and descriptions are taken from both 3D images produced from the synchrotron scans or from examination of high-resolution 3D prints of HAA1. Both scans and 3D shape files of HAA1 are available for download on https://Morphosource.org . A high resolution movie of HAA1 is available as Supplementary Movie 2.

The shape of HAA1 is distinctive in comparison to other rocks on the surface or encountered during excavation of the Hill Antechamber or Dinaledi Chamber. HAA1 is 138.5 mm in total length. Its greatest supero-inferior height is 49mm just left of the middle of center. Its greatest width is 26.3mm. HAA1 is roughly crescent-shaped coming to a sharp point laterally left and a more rounded but antero posteriorly sharp edge right laterally. It presents a large flake scar of ca. 80mm in length on the anterior-inferior surface from approximately 10mm left laterally of its midline that travels to within 12mm of the right lateral end. The lunate area of this flake scar occupies approximately three quarters of the body of the artifact for most of its extent. A 6-7mm wide ledge is observed in the superior one third of the artifact that is created from the removal of rock flake ca. 84.5mm in length that leaves a prominent hump occupying the middle 65mm of the artifact. We cannot determine the type of stone unambiguously from scan data but we hypothesize based on its surface characteristics that it is likely composed of dolomite.

Within the area of the lunate flake scar on the anterior surface, and opposite this area on the posterior surface, striations are visible that appear to be use wear or erosional marks (Figure 12). Some of these lines are as much as 1.5mm wide but most are sub-millimeter in width and are 20 to 25mm in length. They travel predominantly in an lower-left to upper-right

direction across this surface. These lines do not pass outside of the lunate flake scar area and are not visible in synchrotron segments of the rock below the surface, indicating that they are surface features confined to the area of the flake scar (Figure 12).

The posterior surface of HAA1 is dominated by a prominent ridge that runs from the left lateral point supero-laterally at an approximate 15 degree angle, reaching the superior edge about 50mm from the right lateral edge. The peak of the ridge forms the greatest width of the artifact and this occurs approximately 55mm from the left lateral end. Supero-inferiorly oriented erosional or wear lines are found on the right lateral half of the artifact roughly mirroring those on the anterior surface. There is a depressed area that may represent a worn flake removal in this same region that is not as large nor prominent as that found on the anterior surface.

The inferior edge of the artifact along the area of the anterior lunate flake scar is very sharp and under high resolution imaging by synchrotron (6µm), irregular serration is visible across the whole of the surface (Figure 12). No other serration is obvious along the edges of other sharp areas.

Supplementary Information 4: Materials and Methods

Supplementary Information 4.1: Previous Excavations in the Dinaledi Chamber

During the first two excavations undertaken in the Dinaledi Chamber (November 2013 and March 2014), a combination of structured white-light surface scans and high-resolution laser point cloud scans were used to collect 3D data on the spatial position of fossils, from which relative location and orientation of specimens could be derived (Figure S22). Most specimens, both on the surface of the chamber and in the excavation unit, were

scanned *in situ* once uncovered and prior to collection. These spatial data were compiled and form the basis of this study. Work by Kruger and colleagues (*11*) details the workflow for the scanning process and resulting geo-referencing.

By combining scans from the surface of the chamber, as well as the main excavation pit, a 3D record of all collected and excavated fossil material was created. Individual white-light source photogrammetry scans, taken during excavations, were converted to the E57 point cloud File Format for 3D Imaging Data Exchange (*12*). These E57 point cloud data structures were aligned to the broader context of the Dinaledi Chamber (*11*) using CloudCompare (*13*). Each scan was aligned in CloudCompare by manually picking three or more reference points which were common to both the individual scan and the georeferenced Terrestrial Laser Scan (TLS) data collected from the Dinaledi Chamber. Reference points were a combination of fixed survey pins (15 in total) in the Dinaledi Chamber, together with permanent geological features of the chamber walls and floor that can be repeatedly identified in multiple scans. It is often convenient to refer to the locations of objects in terms of these reference points. As excavation had only been conducted in one area of the chamber, the remaining pin locations are useful in the present study only in reference to the material recorded and collected from the chamber surface.

Reference points were a combination of fixed survey pins (15 in total) in the Dinaledi Chamber, together with permanent geological features of the chamber walls and floor that can be repeatedly identified in multiple scans. It is often convenient to refer to the locations of objects in terms of these reference points. As excavation has only been conducted in one area of the chamber, the remaining pin locations are useful in the present study only in reference to the material recorded and collected from the chamber surface.

Scans were aligned from the most recent (from the excavation during March 2014) to the oldest (November 2013). Once the scans were rotated, aligned and scaled, fine registration was applied, to provide an optimum alignment. Once scans were accurately aligned, the 3D transformation was then applied and the individual scan's coordinate system was then updated to the global coordinates of the chamber, and thus any other scan's coordinates within the broader framework of the Dinaledi Chamber. This method of data collection provides a virtual snapshot of the excavations at any one point in time.

Individual bones and fossil fragments were then plotted, and their coordinates recorded by visualizing the transformed E57 point clouds in Autodesk's Recap 360 software. This was accomplished by using high-resolution white-light source photogrammetry scans, visualized in Artec Studio 10 Professional (and later Artec Studio 11 Professional), in conjunction with the point cloud data, as a guide for placement of coordinate data. A surface resolution of approximately 0.5 mm and a three-dimensional point accuracy of approximately 0.1 mm ensured accurate placement of bone material into the global coordinate system. A centroid datum of these data, in the form of 3D points (x, y and z), were recorded for individual teeth, fragments and other small elements. In the case of long bones, a coordinate for the distal, centroid and proximal end of each bone or portion was recorded. Thus, when possible, three coordinates were recorded for each long bone, allowing for the directionality (strike and dip) of these bones to be attributed in spatial analysis in relation to the rest of the fossil assemblage. For long bone material for which it was not possible to record 3 coordinates ("distal", "proximal" and "center"), a centroid was calculated based on the coordinates of endpoints ("distal" and "proximal" points).

Supplementary Information 4.2. Previous work in other parts of the cave system

The evidence from the Lesedi Chamber (*2*) we now recognize may represent a situation of possible mortuary practice by *H. naledi*. The LES1 partial skeleton was excavated from the 102a locality, which is within a blind tunnel approximately 1.8 m in length, with a tapering width of c50 cm and a floor located above the current floor of the Lesedi Chamber. Portions of this skeleton were exposed on the sediment surface at the time of discovery, and a few elements were discovered up to 6 m away on the surface, but most were contained within a 10cm layer of weakly stratified, unlithified mud clast breccia beneath a 2 cm-thick lighter brown colored mudstone, like that found in the Dinaledi Chamber. Some volume of the sediment containing skeletal remains had slumped downward from this alcove onto the cave floor (*2*). The recovered material includes anatomically contiguous elements, with a small number found in articulation. Sediment from the Lesedi Chamber excavation is similar in chemical content to that associated with Dinaledi Feature 1, including the significant positive loadings of P and S on PC2 (Figure 7). The combined evidence suggests that the LES1 individual was also buried with soft tissue present, with later surface exposure of some elements due to sediment slumping from the alcove. Although we cannot rule out that other features may occur within the floor of the Lesedi Chamber, the location of the LES1 individual in this blind tunnel or alcove clearly placed it in a different situation from the chamber floor.

We have described elsewhere (*1, 3*) the occurrence of isolated remains of a *H. naledi* juvenile individual within the U.W. 110 locality, which lies within the Dinaledi Subsystem approximately 10m beyond the Dinaledi Chamber within a narrow (< 20cm) fissure passage. The bones comprise parts of a skull with some teeth, absent the mandible or any postcranial remains. The material presents no signs of bone surface modifications indicative of mechanical damage caused by postdepositional transport, nor are the sedimentary and

stratigraphic situation in the subsystem compatible with flooding or other conditions that would enable water transport (*5*). It is plausible that *H. naledi* placed the skull in this location and this may reflect a mortuary practice different from the graves seen in the other chambers. We have located three other occurrences of *H. naledi* fossils in similarly remote situations. Though analyses of these remains and their situations have not been concluded, each is challenging to explain without the involvement of *H. naledi* in their placement.

References

Brophy, J. K., Elliott, M. C., De Ruiter, D. J., Bolter, D. R., Churchill, S. E., Walker, C. S., ... & Berger, L. R. (2021). Immature hominin craniodental remains from a new locality in the Rising Star Cave System, South Africa. *PaleoAnthropology*, 2021 (1) 1-14.

Dirks, P. H., Berger, L. R., Roberts, E. M., Kramers, J. D., Hawks, J., Randolph-Quinney, P. S., ... & Tucker, S. (2015). Geological and taphonomic context for the new hominin species Homo naledi from the Dinaledi Chamber, South Africa. *Elife*, *4*, e09561.

Elliott, M., Makhubela, T., Brophy, J., Churchill, S., Peixotto, B., Feuerriegel, E., ... & Berger, L. (2021). Expanded Explorations of the Dinaledi Subsystem, Rising Star Cave System, South Africa. *Paleoanthropology*, 2021(1), 15-22.

Makhubela, T. V., Kramers, J. D., Belyanin, G. A., Dirks, P. H. G. M., & Roberts, E. M. (2017). Proterozoic $^{40}Ar/^{39}Ar$ ages from cave deposits of the Malapa, Sterkfontein and Dinaledi fossil sites, Cradle of Humankind, *South Africa. South African Journal of Geology* 2017, 120(1), 21-44.

Wiersma, J. P., Roberts, E. M., & Dirks, P. H. (2020). Formation of mud clast breccias and the process of sedimentary autobrecciation in the hominin-bearing (Homo naledi)

Rising Star Cave system, South Africa. *Sedimentology*, *67*(2), 897-919.

Supplementary Information: Tables

Supplementary Table 1. Bulk chemistry obtained from x-ray fluorescence (XRF) in weight percentage (wt.%).

Sample number on PCA	Sample name	Sample locality within Rising Star cave	Al_2O_3	BaO	CaO	Fe_2O_3	K_2O	MgO	MnO	Na_2O	P_2O_5	SiO_2	SO_3	TiO_2	LOI	Sum
1	DF1	Dinaledi floor (DF group) sediments from above Features 1 and 2 collected during excavation and opening of features	16.39	0.08	1.55	10.69	1.72	2.79	4.41	-	0.27	52.67	-	0.75	9.10	100.42
2	DF2		16.97	0.07	1.18	10.15	1.75	2.42	3.66	-	0.19	54.23	-	0.81	8.51	99.93
3	DF3		15.65	0.07	1.22	10.49	1.61	2.66	4.25	-	0.37	54.69	-	0.75	8.33	100.10
4	DF4		16.09	0.08	1.17	10.33	1.68	2.67	4.32	-	0.27	53.11	-	0.76	8.66	99.13
5	DF5		16.23	0.07	1.21	10.51	1.68	2.51	4.30	-	0.29	53.89	-	0.75	8.55	99.98
6	DF6		16.02	0.07	1.21	10.46	1.67	2.59	4.29	-	0.25	54.10	-	0.77	8.61	100.03
7	DF7		16.47	0.07	1.58	10.09	1.71	2.73	3.98	-	0.27	53.34	-	0.77	9.10	100.11
8	DF8		14.38	0.06	6.90	8.95	1.52	3.08	3.45	-	0.57	48.09	-	0.69	12.31	99.99
9	DF9		15.63	0.08	1.04	10.42	1.62	2.51	4.51	-	0.34	54.90	-	0.73	8.14	99.93
10	DF10		16.09	0.08	1.17	10.66	1.67	2.56	4.53	-	0.35	53.33	-	0.74	8.90	100.08
11	DF11		17.45	0.07	0.86	10.38	1.80	2.13	3.70	-	0.18	53.75	-	0.81	8.74	99.88
12	DF12		16.91	0.07	1.30	10.42	1.74	2.20	4.09	-	0.48	52.89	-	0.78	9.03	99.92
13	DF13		15.82	0.08	0.92	10.70	1.68	2.31	4.52	-	0.27	55.15	-	0.75	8.04	100.24
14	DF14		16.45	0.06	0.76	10.08	1.68	2.08	3.70	-	0.21	56.30	-	0.78	7.84	99.94
15	DF15		15.15	0.08	1.00	10.79	1.70	2.61	5.28	-	0.23	53.78	-	0.71	8.44	99.76
16	DF16		16.09	0.08	0.88	10.69	1.71	2.39	4.60	-	0.23	53.82	-	0.76	8.33	99.57
17	DF17		15.35	0.07	0.88	10.36	1.60	2.33	4.35	-	0.25	56.10	-	0.73	7.93	99.96
18	DF18		15.48	0.08	0.95	10.46	1.61	2.27	4.41	-	0.27	55.39	-	0.73	8.29	99.93
19	DF19		16.73	0.06	0.80	10.07	1.71	2.25	3.62	-	0.16	55.60	-	0.81	8.25	100.06
20	DF20		17.30	0.06	0.97	10.13	1.72	2.22	3.49	-	0.20	54.30	-	0.80	8.69	99.88
21	DF21		14.57	0.08	0.89	9.55	1.49	2.00	3.59	-	0.33	59.28	-	0.72	7.62	100.11
22	DF22		14.85	0.08	0.89	10.22	1.54	2.07	4.13	-	0.32	57.61	-	0.72	7.86	100.29
23	DF23		14.13	0.08	0.96	9.78	1.42	2.32	3.86	-	0.34	58.71	-	0.70	7.65	99.94
24	DF24		14.69	0.07	1.00	9.50	1.42	2.33	3.45	-	0.39	58.44	-	0.72	7.60	99.60
25	DF25		15.02	0.06	0.91	9.51	1.44	2.36	3.50	-	0.29	58.57	-	0.74	7.67	100.07

26	DF26		14.78	0.06	1.08	9.28	1.43	2.32	3.20	-	0.40	58.76	-	0.76	7.61	99.68
27	DF27		15.18	0.09	0.98	9.54	1.52	2.12	3.74	-	0.36	57.51	-	0.76	7.73	99.52
28	DF28		13.71	0.08	1.01	9.31	1.35	2.18	3.78	-	0.31	60.38	-	0.70	7.27	100.07
29	DF29		14.80	0.08	1.55	9.96	1.52	2.22	4.60	-	0.75	55.51	-	0.70	8.05	99.74
30	DF30		14.26	0.07	1.18	9.64	1.47	2.02	4.02	-	0.51	58.44	-	0.71	7.50	99.81
31	DF31		16.19	0.08	0.88	10.10	1.69	1.95	3.88	-	0.30	56.21	-	0.78	7.96	100.02
32	DF32		14.88	0.07	1.36	9.80	1.53	1.94	3.90	-	0.63	57.03	-	0.73	7.70	99.58
33	DF33		14.10	0.07	2.11	9.45	1.49	1.91	3.92	-	1.16	57.55	-	0.69	7.49	99.94
34	DF34		16.09	0.07	2.03	10.19	1.68	2.01	3.54	-	1.14	54.58	-	0.78	8.05	100.18
		Average	**15.59**	**0.07**	**1.30**	**10.08**	**1.60**	**2.33**	**4.02**	**-**	**0.38**	**55.53**	**-**	**0.75**	**8.28**	**99.92**
		***In situ* sediments around Feature 1 on the Dinaledi floor**														
35	A1a	SA group samples sterile areas around Feature 1 on floor	14.02	0.06	4.70	9.12	1.44	4.29	3.60	-	0.75	48.99	-	0.67	11.89	99.54
36	A1b		17.95	0.06	1.18	10.77	1.44	2.08	6.57	-	0.12	48.76	-	0.65	10.09	99.67
37	A2a		15.12	0.09	0.81	10.52	1.56	2.48	5.14	-	0.16	54.71	-	0.70	8.34	99.63
38	A2b		15.69	0.05	0.82	8.53	1.35	1.69	4.34	-	0.09	59.01	-	0.55	7.85	99.98
39	A3		13.00	0.07	5.05	9.03	1.36	4.67	4.19	-	0.68	47.76	-	0.62	12.47	98.91
40	A4		15.46	0.11	0.88	12.84	2.01	2.59	7.06	-	0.19	48.44	-	0.65	9.18	99.41
41	A5		13.34	0.07	3.71	8.88	1.37	3.94	3.75	-	0.47	52.66	-	0.66	10.71	99.55
42	A6		15.32	0.10	0.81	10.99	1.76	2.45	6.24	-	0.14	51.72	-	0.70	9.05	99.29
43	A7		13.19	0.07	4.85	8.99	1.37	4.52	3.94	-	0.55	48.99	-	0.64	12.32	99.42
44	A8		14.29	0.07	3.16	10.22	1.52	3.75	4.40	-	0.41	49.87	-	0.71	10.82	99.21
		Average	**14.74**	**0.08**	**2.60**	**9.99**	**1.52**	**3.25**	**4.92**	**-**	**0.36**	**51.09**	**-**	**0.65**	**10.27**	**99.46**
45	B1a	SB group of samples from Feature 1	14.85	0.06	0.82	8.99	1.58	1.52	4.53	-	0.14	58.77	-	0.65	7.41	99.31
46	B1b		14.49	0.08	1.20	9.92	1.42	2.18	4.31	-	0.46	56.52	-	0.68	7.80	99.06
47	B2		16.65	0.05	0.72	8.83	1.50	1.68	3.48	-	0.09	57.65	-	0.71	7.97	99.33
		Average	**15.33**	**0.06**	**0.91**	**9.24**	**1.50**	**1.79**	**4.11**		**0.23**	**57.65**		**0.68**	**7.73**	**99.23**
48	C1	SC group samples between Features 1 and 2	15.32	0.05	0.76	8.25	1.69	1.38	2.68	-	0.14	61.98	-	0.77	6.80	99.82
49	C2a		17.10	0.07	0.54	9.30	1.74	1.59	3.24	-	0.10	56.77	-	0.83	8.24	99.52
50	C2b		12.03	0.06	0.69	7.45	1.42	1.37	3.72	-	0.10	65.79	-	0.56	6.18	99.36
51	C3		15.43	0.10	0.95	10.57	1.64	1.86	5.24	-	0.35	53.63	-	0.72	9.16	99.65
		Average	**14.97**	**0.07**	**0.73**	**8.89**	**1.62**	**1.55**	**3.72**		**0.17**	**59.54**		**0.72**	**7.60**	**99.58**
52	E1		15.03	0.07	0.86	10.31	1.59	2.11	4.83	-	0.23	55.68	-	0.72	7.91	99.34
53	E2		14.17	0.07	0.76	10.03	1.47	2.08	4.50	-	0.17	58.16	-	0.67	7.54	99.62

54	E3	SE group samples from vertical wall south of Feature 1	16.01	-	0.33	7.35	1.54	1.58	0.50	-	0.10	65.01	-	0.96	6.25	99.62
55	E4		15.30	0.08	0.73	10.36	1.55	2.28	4.70	-	0.15	55.66	-	0.73	8.05	99.60
56	E5		15.00	0.08	0.69	10.27	1.55	2.39	4.88	-	0.15	55.38	-	0.71	8.12	99.21
		Average	**15.10**	**0.08**	**0.68**	**9.66**	**1.54**	**2.09**	**3.88**		**0.16**	**57.98**		**0.76**	**7.57**	**99.48**
Lesedi Chamber																
57	LBL1	Lesedi Chamber sediments from fossil-bearing ledge and cavern floor sediments with *Homo naledi* fossils	9.87	0.05	4.33	7.16	1.25	2.14	4.89	0.21	0.10	58.93	0.79	0.44	9.00	99.15
58	LBL2		6.15	0.05	6.22	6.51	1.05	1.59	6.16	0.09	0.09	60.83	0.19	0.25	9.53	98.70
59	LBL3		7.66	0.06	1.62	7.42	1.35	2.08	7.13	-	0.11	64.47	-	0.33	7.19	99.41
60	LFP1a		6.84	-	14.10	4.18	0.68	1.61	1.43	-	0.76	51.82	0.07	0.40	17.17	99.06
61	LFP1b		7.53	-	2.01	4.75	0.66	0.72	1.35	-	0.77	72.56	-	0.50	8.41	99.25
62	LFP2		6.49	-	3.61	4.19	0.56	0.63	1.35	-	2.05	71.92	0.10	0.44	7.92	99.27
63	LFP3		8.57	-	1.76	5.49	0.76	0.78	1.63	-	0.65	70.14	-	0.56	8.81	99.15
64	LFP-cmp		8.97	-	2.29	5.84	0.96	1.13	2.46	-	0.67	68.20	0.10	0.49	8.11	99.21
		Average	**7.76**	**0.05**	**4.49**	**5.69**	**0.91**	**1.34**	**3.30**	**0.15**	**0.65**	**64.86**	**0.25**	**0.43**	**9.52**	**99.15**
Dinaledi Subsystem																
65	2280	Dinaledi floor	15.16	0.23	1.17	9.07	1.60	2.17	16.05	0.07	0.17	41.21	-	0.66	10.66	98.23
66	HAP1	Sediments from fossil-bearing and sterile sediments in the Dinaledi Subsystem: UW108 to UW111	16.57	-	0.28	8.67	1.23	0.68	0.95	-	0.08	63.08	-	0.90	6.23	98.65
67	HD01		12.82	0.06	0.54	9.07	0.88	3.20	1.89	-	0.07	63.48	-	0.77	6.43	99.21
68	HD02		12.74	0.06	0.87	9.88	1.24	2.45	3.59	-	0.12	59.79	-	0.67	7.07	98.48
69	HD03		5.47	-	16.79	5.05	0.56	12.66	2.48	-	0.08	28.41	-	0.27	27.32	99.07
70	LO1		15.38	0.08	0.62	9.96	1.65	2.36	4.48	-	0.11	55.96	-	0.73	7.98	99.30
71	LO2		12.11	0.07	6.10	9.14	1.35	7.03	4.45	-	0.11	42.52	-	0.55	14.92	98.35
72	LO3		5.93	-	25.27	4.14	0.68	9.70	2.15	-	0.06	20.22	-	0.28	30.46	98.89
73	LO4		21.90	-	0.31	7.35	2.53	4.75	0.13	0.10	0.06	53.66	-	1.01	8.02	99.83
74	PF01		13.23	0.06	0.89	10.52	1.20	2.10	3.81	0.12	0.10	58.25	0.43	0.68	7.36	98.75
75	PF02		0.39	-	5.09	32.71	0.07	5.61	11.38	-	0.05	27.46	-	-	15.18	97.94
76	PF03		6.46	0.05	1.23	8.36	0.74	1.97	5.58	-	0.10	68.11	0.56	0.28	5.90	99.33
77	PFL01		7.24	-	5.67	4.94	0.53	0.70	1.07	-	-	66.18	6.86	0.47	4.99	98.64
78	PRG01		16.06	0.07	0.88	10.61	1.51	2.66	4.16	-	0.13	53.40	-	0.73	8.67	98.88
79	PRG02		8.44	-	7.65	5.53	0.57	0.96	1.03	-	0.06	63.33	-	0.52	10.04	98.12
80	TC01		14.27	0.06	5.44	9.65	1.44	3.69	3.59	-	0.46	46.83	-	0.63	11.99	98.06

Supplementary Table 2. Particle size distribution (PSD) of sediments from the Dinaledi Chamber floor and the Lesedi Chamber represented using the Folk and Ward Method.

Sample number on grain size plot	Sample name	Sample type	Texture	Sediment name	Folk and Ward Method (µm)			
					Mean grain size	Sorting	Skewness	Kurtosis
1	DF1	Polymodal, Poorly Sorted	Sand	Poorly Sorted Coarse Sand	372.21	2.60	-0.07	0.78
2	DF2	Polymodal, Poorly Sorted	Muddy Sand	Very Coarse Silty Fine Sand	279.24	3.22	-0.07	0.85
3	DF3	Polymodal, Poorly Sorted	Sand	Poorly Sorted Coarse Sand	442.02	2.28	-0.06	0.75
4	DF4	Trimodal, Poorly Sorted	Sand	Poorly Sorted Coarse Sand	373.84	2.90	-0.23	0.91
5	DF5	Polymodal, Poorly Sorted	Sand	Poorly Sorted Medium Sand	356.86	2.61	-0.03	0.76
6	DF6	Trimodal, Poorly Sorted	Sand	Poorly Sorted Coarse Sand	444.55	2.28	-0.08	0.75
7	DF7	Polymodal, Poorly Sorted	Sand	Poorly Sorted Medium Sand	375.33	2.54	-0.05	0.77
8	DF8	Polymodal, Poorly Sorted	Sand	Poorly Sorted Medium Sand	433.52	2.29	-0.05	0.74
9	DF9	Polymodal, Poorly Sorted	Sand	Poorly Sorted Coarse Sand	379.40	2.49	-0.03	0.74
10	DF10	Polymodal, Poorly Sorted	Sand	Poorly Sorted Coarse Sand	443.43	2.27	-0.06	0.74
11	DF11	Trimodal, Poorly Sorted	Sand	Poorly Sorted Coarse Sand	351.16	2.81	-0.12	0.83
12	DF12	Polymodal, Poorly Sorted	Sand	Poorly Sorted Fine Sand	336.17	2.68	-0.02	0.74
13	DF13	Polymodal, Poorly Sorted	Sand	Poorly Sorted Medium Sand	369.75	2.51	-0.02	0.73
14	DF14	Polymodal, Poorly Sorted	Sand	Poorly Sorted Coarse Sand	416.46	2.34	-0.04	0.73
15	DF15	Polymodal, Poorly Sorted	Sand	Poorly Sorted Medium Sand	334.22	2.79	-0.05	0.80
16	DF16	Polymodal, Poorly Sorted	Sand	Poorly Sorted Fine Sand	306.38	2.89	-0.02	0.77
17	DF17	Polymodal, Poorly Sorted	Sand	Poorly Sorted Medium Sand	362.50	2.55	-0.02	0.74
18	DF18	Polymodal, Poorly Sorted	Sand	Poorly Sorted Coarse Sand	369.84	2.52	-0.02	0.73
19	DF19	Trimodal, Poorly Sorted	Sand	Poorly Sorted Coarse Sand	533.93	2.31	-0.28	1.01
20	DF20	Polymodal, Poorly Sorted	Sand	Poorly Sorted Medium Sand	385.75	2.46	-0.03	0.74
21	DF21	Polymodal, Poorly Sorted	Muddy Sand	Very Coarse Silty Fine Sand	261.64	3.29	-0.05	0.82

22	DF22	Polymodal, Poorly Sorted	Sand	Poorly Sorted Fine Sand	305.33	2.87	-0.01	0.75
23	DF23	Polymodal, Poorly Sorted	Muddy Sand	Very Coarse Silty Medium Sand	270.15	3.34	-0.08	0.86
24	DF24	Polymodal, Poorly Sorted	Sand	Poorly Sorted Fine Sand	302.06	2.90	-0.02	0.76
25	DF25	Polymodal, Poorly Sorted	Sand	Poorly Sorted Medium Sand	340.90	2.82	-0.08	0.84
26	DF26	Trimodal, Poorly Sorted	Sand	Poorly Sorted Coarse Sand	331.13	2.97	-0.14	0.84
27	DF27	Polymodal, Poorly Sorted	Muddy Sand	Very Coarse Silty Fine Sand	208.47	3.89	-0.07	0.84
28	DF28	Trimodal, Poorly Sorted	Muddy Sand	Very Coarse Silty Coarse Sand	288.48	3.21	-0.09	0.85
29	DF29	Polymodal, Poorly Sorted	Sand	Poorly Sorted Medium Sand	317.93	2.87	-0.05	0.80
30	DF30	Polymodal, Poorly Sorted	Sand	Poorly Sorted Coarse Sand	442.62	2.28	-0.07	0.75
31	DF31	Polymodal, Poorly Sorted	Muddy Sand	Very Coarse Silty Fine Sand	268.14	3.32	-0.07	0.85
32	DF32	Polymodal, Poorly Sorted	Muddy Sand	Very Coarse Silty Fine Sand	222.71	3.69	-0.06	0.83
33	DF33	Polymodal, Poorly Sorted	Sand	Poorly Sorted Medium Sand	337.60	2.71	-0.03	0.76
34	DF34	Bimodal, Poorly Sorted	Sand	Poorly Sorted Coarse Sand	442.46	2.63	-0.28	0.94
35	A1a	Polymodal, Poorly Sorted	Sand	Poorly Sorted Medium Sand	323.81	2.84	-0.05	0.80
36	A1b	Polymodal, Poorly Sorted	Sand	Poorly Sorted Fine Sand	329.55	2.73	-0.02	0.75
37	A2a	Trimodal, Poorly Sorted	Sand	Poorly Sorted Coarse Sand	468.58	2.42	-0.21	0.92
38	A2b	Polymodal, Poorly Sorted	Sand	Poorly Sorted Coarse Sand	330.95	2.76	-0.03	0.77
39	A3	Trimodal, Poorly Sorted	Muddy Sand	Very Coarse Silty Coarse Sand	277.86	3.27	-0.09	0.85
40	A4	Trimodal, Poorly Sorted	Sand	Poorly Sorted Coarse Sand	370.36	2.64	-0.08	0.81
41	A5	Polymodal, Poorly Sorted	Sand	Poorly Sorted Medium Sand	345.26	2.66	-0.03	0.76
42	A6	Polymodal, Poorly Sorted	Sand	Poorly Sorted Fine Sand	332.60	2.72	-0.02	0.75
43	A7	Polymodal, Poorly Sorted	Sand	Poorly Sorted Fine Sand	308.77	2.84	-0.01	0.75
44	A8	Bimodal, Poorly Sorted	Sand	Poorly Sorted Coarse Sand	354.38	2.95	-0.16	0.91
45	B1a	Polymodal, Poorly Sorted	Muddy Sand	Very Coarse Silty Fine Sand	237.81	3.51	-0.05	0.82
46	B1b	Polymodal, Poorly Sorted	Sand	Poorly Sorted Medium Sand	360.13	2.58	-0.03	0.75
47	B2	Trimodal, Poorly Sorted	Sand	Poorly Sorted Medium Sand	358.12	2.67	-0.06	0.80
48	C1	Polymodal, Poorly Sorted	Sand	Poorly Sorted Medium Sand	362.99	2.58	-0.03	0.75
49	C2a	Polymodal, Poorly Sorted	Sand	Poorly Sorted Medium Sand	328.85	2.81	-0.05	0.80
50	C2b	Polymodal, Poorly Sorted	Sand	Poorly Sorted Medium Sand	383.76	2.48	-0.04	0.75

51	C3	Polymodal, Poorly Sorted	Sand	Poorly Sorted Fine Sand	332.60	2.70	-0.02	0.75
52	E1	Polymodal, Poorly Sorted	Sand	Poorly Sorted Fine Sand	329.15	2.71	-0.01	0.74
53	E2	Polymodal, Poorly Sorted	Muddy Sand	Very Coarse Silty Medium Sand	265.82	3.36	-0.09	0.84
54	E3	Trimodal, Poorly Sorted	Sand	Poorly Sorted Coarse Sand	460.70	2.21	-0.06	0.73
55	E4	Polymodal, Poorly Sorted	Sand	Poorly Sorted Coarse Sand	385.72	2.48	-0.04	0.75
56	E5	Trimodal, Poorly Sorted	Muddy Sand	Very Coarse Silty Coarse Sand	278.21	3.25	-0.08	0.84
57	LBL1	Polymodal, Poorly Sorted	Sand	Poorly Sorted Coarse Sand	343.35	2.76	-0.07	0.81
58	LBL2	Polymodal, Poorly Sorted	Sand	Poorly Sorted Coarse Sand	391.62	2.47	-0.05	0.76
59	LBL3	Polymodal, Poorly Sorted	Muddy Sand	Very Coarse Silty Coarse Sand	239.73	3.54	-0.07	0.83
60	LFP1a	Polymodal, Poorly Sorted	Sand	Poorly Sorted Medium Sand	346.40	2.69	-0.04	0.78
61	LFP1b	Polymodal, Poorly Sorted	Sand	Poorly Sorted Coarse Sand	414.74	2.35	-0.04	0.73
62	LFP2	Polymodal, Poorly Sorted	Sand	Poorly Sorted Medium Sand	346.18	2.70	-0.05	0.78
63	LFP3	Polymodal, Poorly Sorted	Sand	Poorly Sorted Fine Sand	354.76	2.58	-0.02	0.73
64	LFPcmp	Polymodal, Poorly Sorted	Sand	Poorly Sorted Coarse Sand	304.82	2.95	-0.04	0.80

Supplementary Information: Figures

Supplementary Figure S1. *In situ* sampling localities around Feature 1 on the Dinaledi Chamber floor. (a) Top view of the Dinaledi floor showing the exposed Feature 1 and the group A (SA) samples from areas outside any feature, group B (SB) samples from inside Feature 1, and group C (SC) samples between Features 1 and 2. (b) Vertical wall where profile group E (SE) samples of Feature 1 were collected.

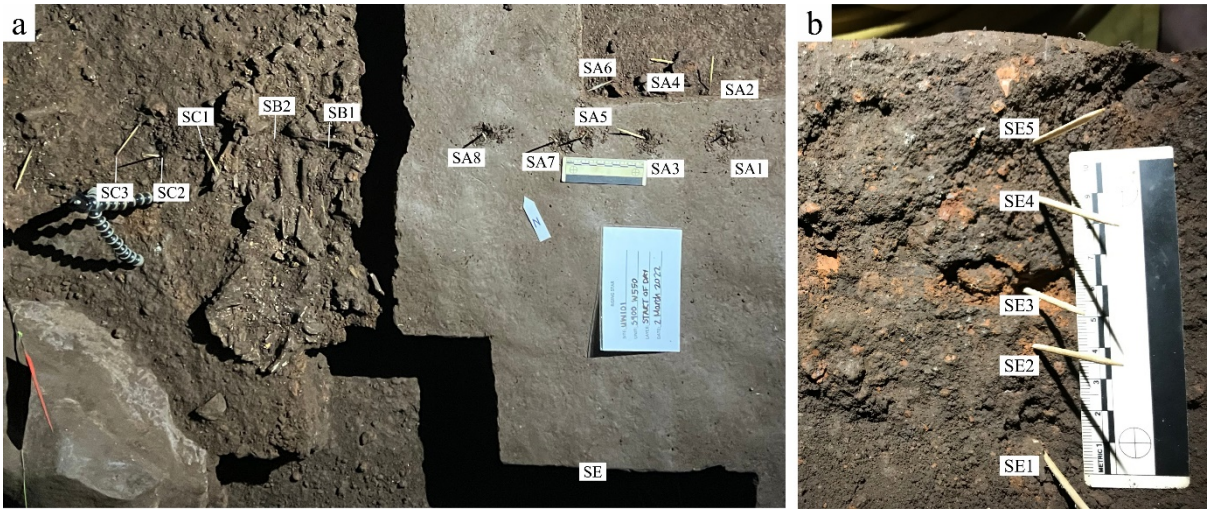

Supplementary Figure S2. Excavation grid plan for Hill Antechamber

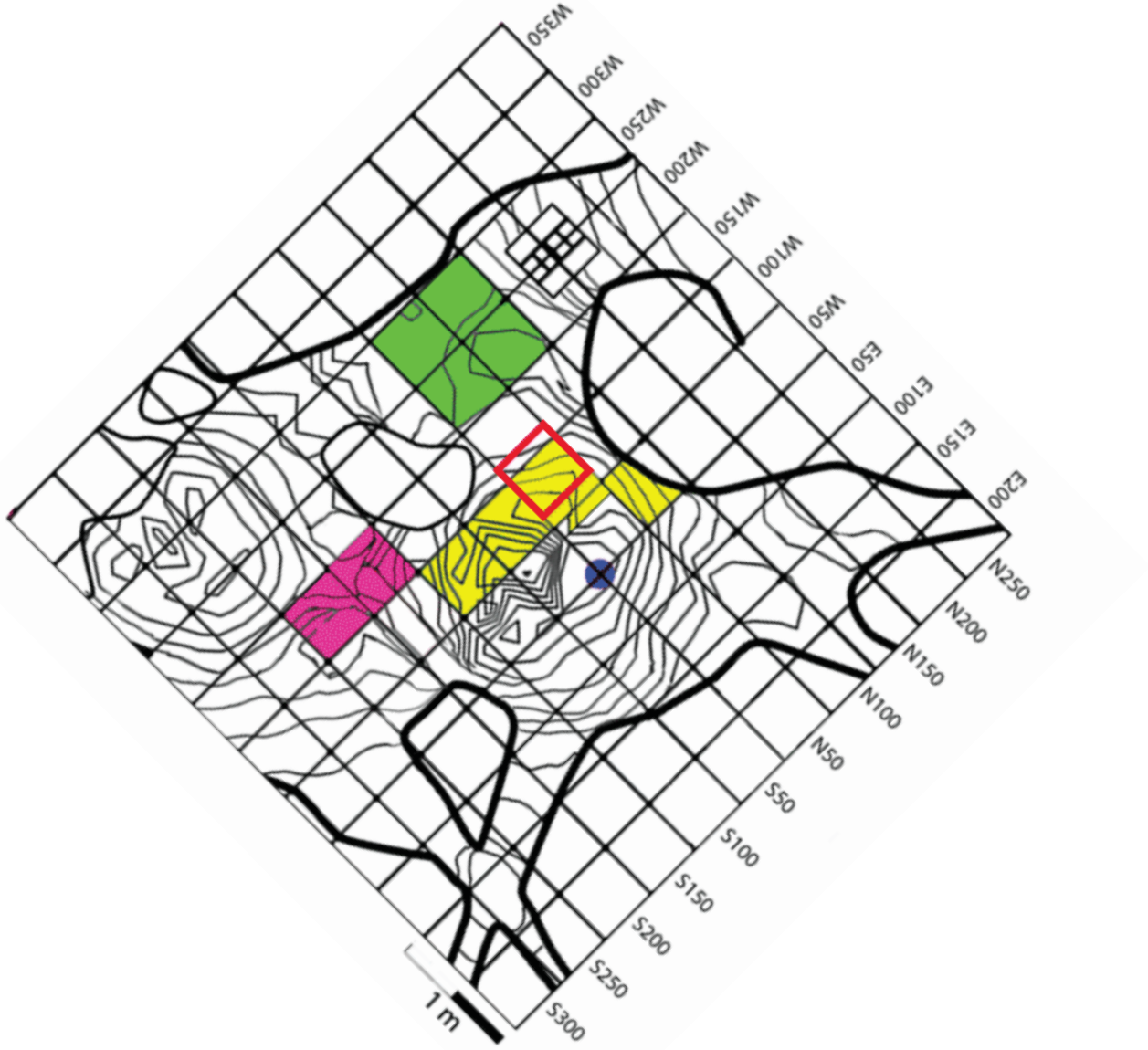

Supplementary Figure S3. Locations of U.W. 108, U.W. 109, and U.W. 110 localities within the Dinaledi Subsystem.

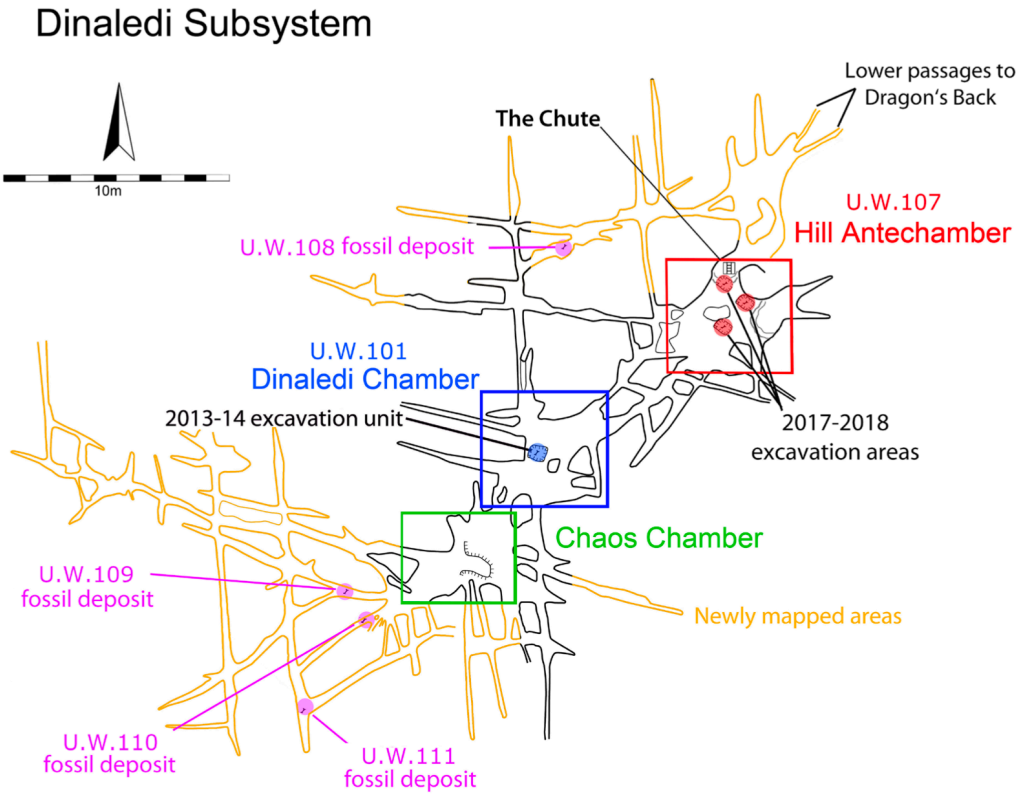

Supplementary Figure S4. SEM photomicrographs of sample 2280 from the Dinaledi floor S of the initial excavation pit. (a) Overview BSE image of the unlithified mud clast breccia (UMCB) with abundant secondary Mn- and Fe-oxyhydroxides occurring as polycrystalline infilling (b) and concretionary infilling (c). (d) EDS chemical maps showing the abundance and distribution of the major elements. Mn is more abundant and localized whereas Fe is more widespread. The mudstone contains appreciable Mg and K than Ca.

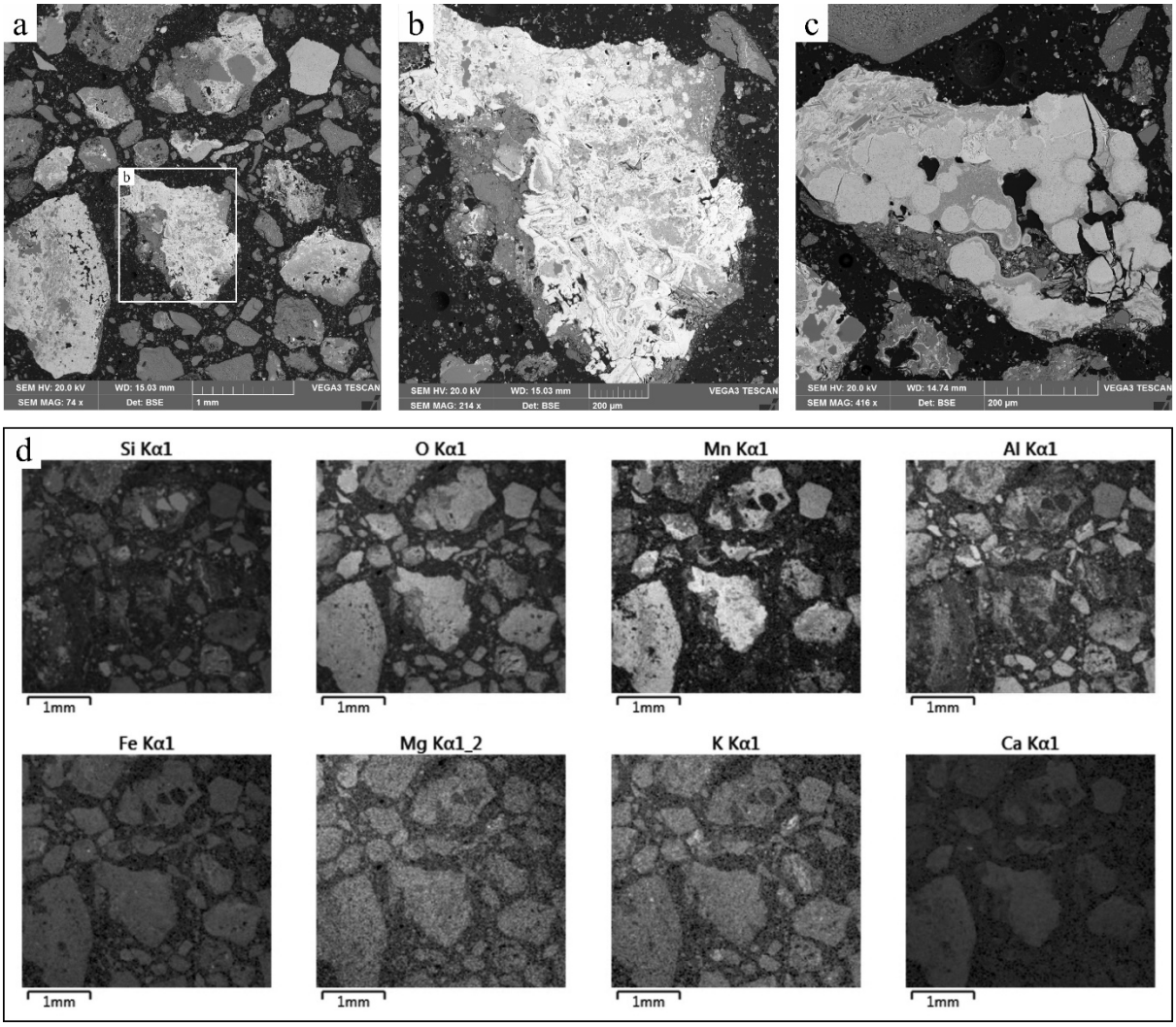

Supplementary Figure S5. SEM photomicrographs of sample L01 from the UW108 passage. (a) BSE image of the UMCB similar to the Dinaledi Chamber floor. (b) EDS chemical maps showing the mud clasts with abundant Fe but little Mn, which is different from the Dinaledi floor UMCB.

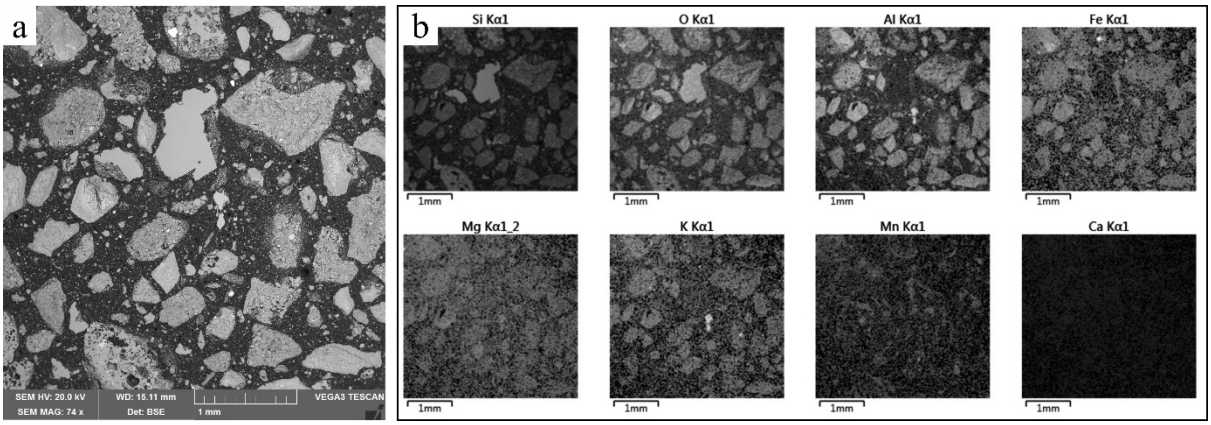

Supplementary Figure S6. SEM photomicrographs of sample L02 from the UW108 passage. (a) BSE image of the UMCB in this sample with abundant visible Mn-oxihydroxide compared to L01 in the form of discrete grains (b) and mud clast infilling (c). (d) EDS chemical maps showing the presence of fragmentary dolomite and discrete Mn-oxihydroxide grains in L02.

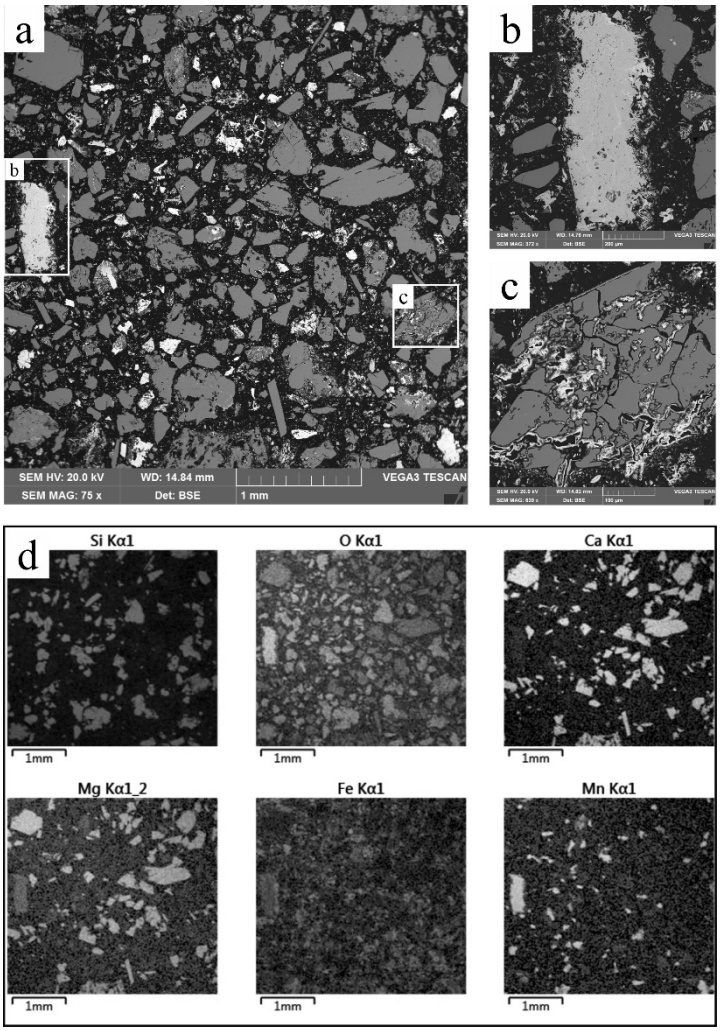

Supplementary Figure S7. SEM photomicrographs of sample L03 from the UW108 passage. (a) BSE image of the highly calcified UMCB containing dolomite clasts that are cemented with calcite. (b) EDS chemical maps showing abundant presence of CaO and MgO and the sparse Mn-oxihydroxide.

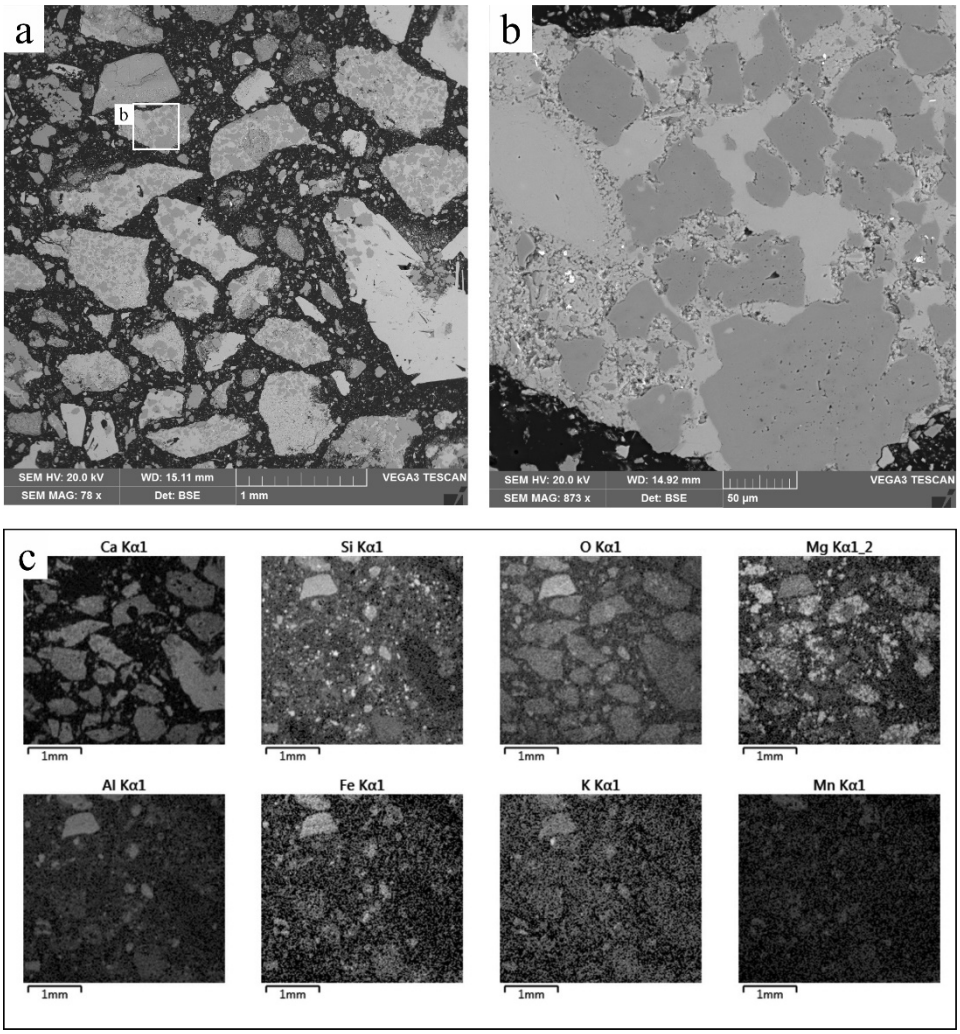

Supplementary Figure S8. SEM photomicrographs of sample L04 from the UW108 passage. (a) BSE image of the unaltered LORM mudstone with a very fine-grained texture. (b) EDS chemical maps showing the dominant clay composition of the LORM mudstone without CaO and MnO.

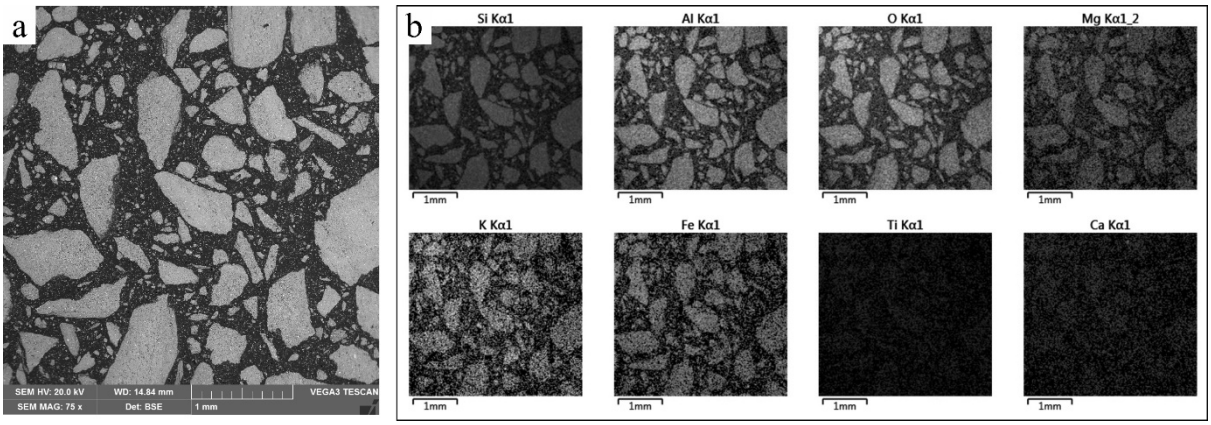

Supplementary Figure S9. SEM photomicrographs of sample PF02 from UW110 above a ledge of broken chert horizon. (a) Overview BSE image of the UMCB sediments showing Mn-Fe-oxihydroxide grains in bright grey colour. (b) Mud clast with Mn-Fe-oxihydroxide concretions. (c) Mud clast with infilling of crystalline Mn-Fe-oxihydroxide. (d) EDS chemical maps showing that the mud clasts contain abundant very fine-grained Fe and Mn not occurring as Mn-Fe-oxihydroxide.

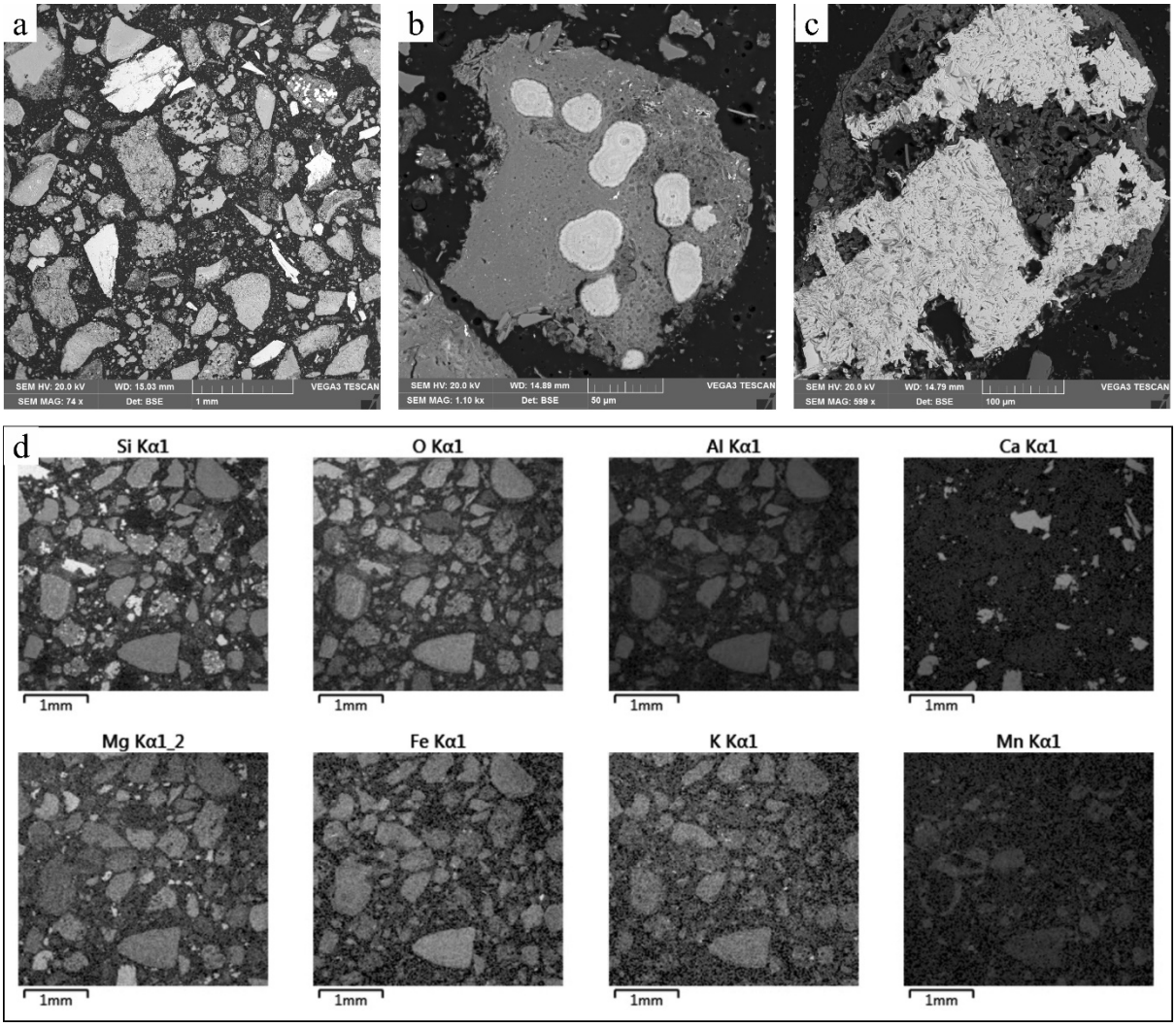

Supplementary Figure S10. SEM photomicrographs of sample PFL01 from UW110 above the second chert ledge from the floor. (a) Overview BSE image of the muddy sandstone with little to no mud clasts and Mn-Fe-oxihydroxide. (b) EDS chemical maps showing the chemistry and textures of the quartz sand and gypsum grains.

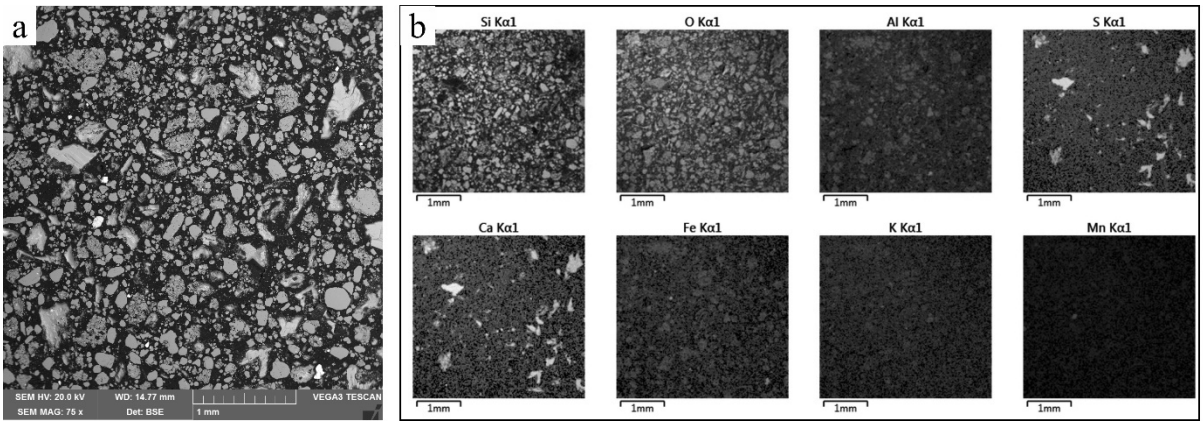

Supplementary Figure S11. SEM photomicrographs of sample HAP1 from the passage used to access UW111. (a) Overview BSE image of the LORM sediments. (b) EDS chemical maps showing the chemistry and textures of the LORM mud clasts, which contain abundant very fine-grained Fe. (c) Close up BSE image of a LORM mud clast containing very fine sand (d).

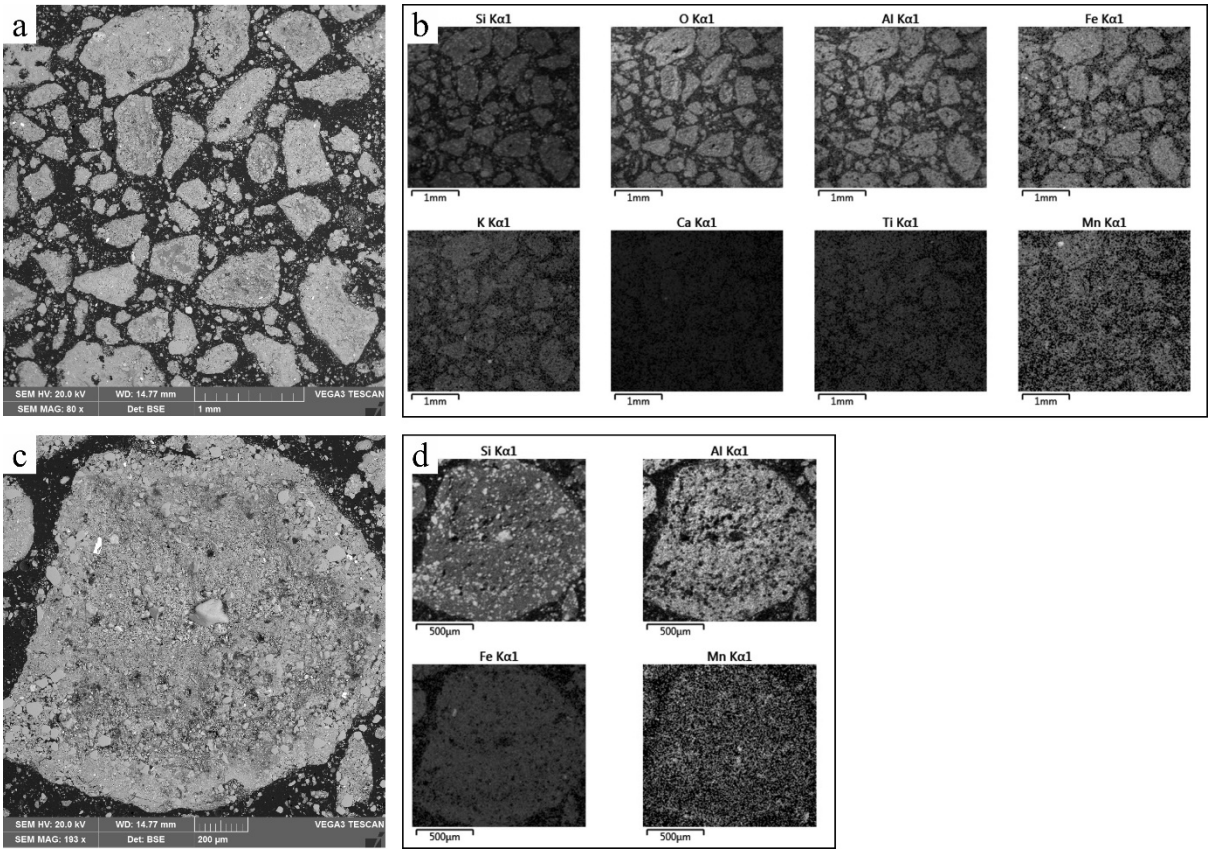

Supplementary Figure S12. SEM photomicrographs of sample HD03 from the UW111 locality. (a) Overview BSE image of the UMCB sediments from beneath a thin flowstone. (b) EDS chemical maps showing that the UMCB sediments are not cemented by calcite but contain discrete, fine-grained dolomite.

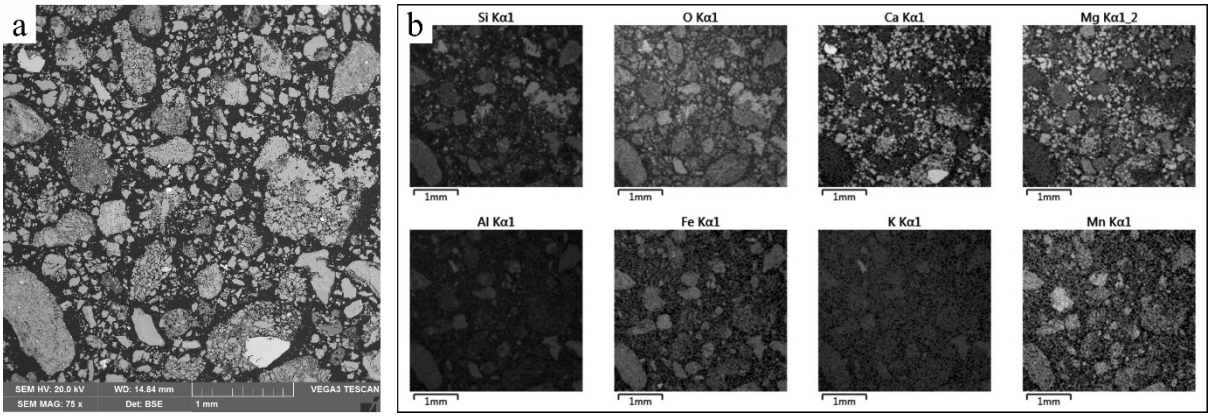

Supplementary Figure S13. Plot of samples vs their mean grain size. The mean grain sizes of half the number of samples is around 350 μm, whereas the other half are variable between 200 μm and 600 μm. The SA and SE groups of samples were sampled from *in situ* sediments at different depths, and their mean grain sizes show upward fining sequences shown by the black arrows (arrows point towards the top of sediments, see Figure S1 for relative depths of samples). The DF group of samples also include samples from different depths, and they show a mixture of upward and downward fining sequences consistent with their mixing during sieving.

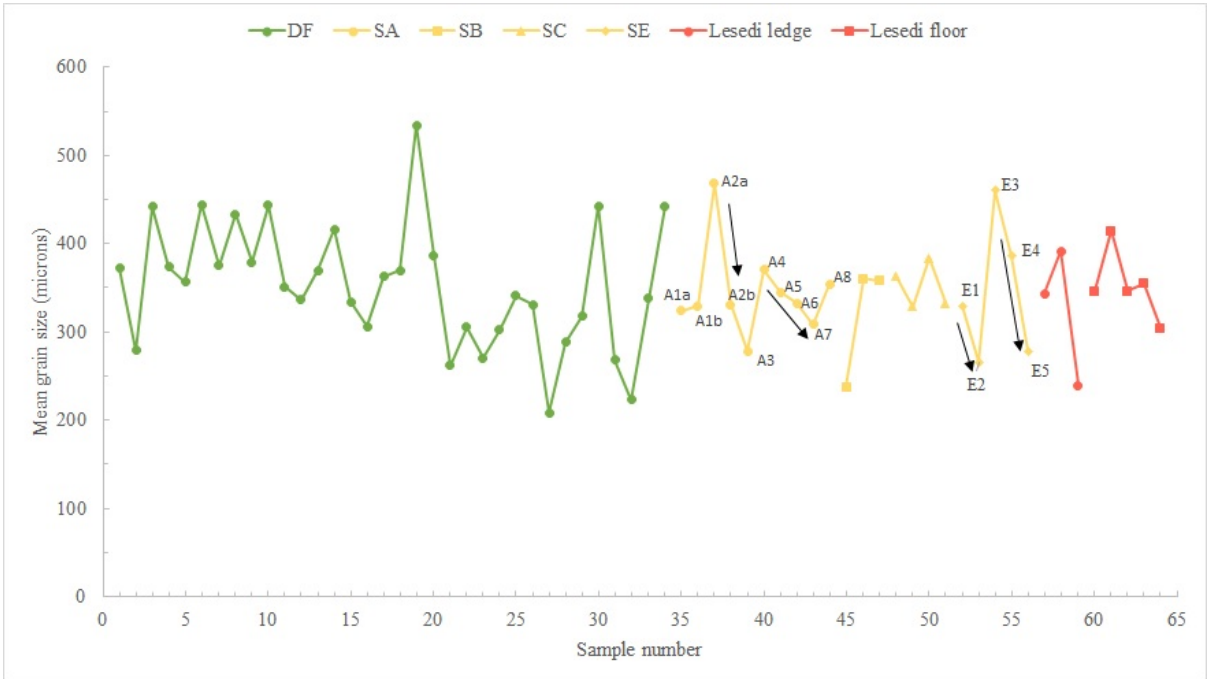

160

Supplementary Figure S14. Excavation unit in Dinaledi Chamber from original 2013–2014 excavation work and locations of 2018 excavation units plotted by photogrammetric reconstruction.

165

Supplementary Figure S15. Hill Antechamber excavation unit S150W150 prior to opening excavation. This area had a collection of non-overlapping flat stones on the surface.

Supplementary Figure S16. Top surface of the Hill Antechamber feature after full exposure. Photo (left) and 3D model based on photogrammetry (right). The bone material at the northmost extent of the feature is powdery and highly fragmented, with more complete skeletal elements visible toward the south.

Supplementary Figure S17. Hill Antechamber feature after pedestaling and separation from surrounding sediment.

Supplementary Figure S18. Sagittal (north-south) section of Hill Antechamber feature. North is at left of frame. This section is at approximately 55% of the east-west breadth of the feature. The articulated foot is visible in longitudinal section at right of frame, with cross-sections of other bones and teeth further to the left of frame. The layer that constitutes the top of the feature is packed with bone material including articulated, semi-articulated and loose material, flattened into less than 5 cm thickness.

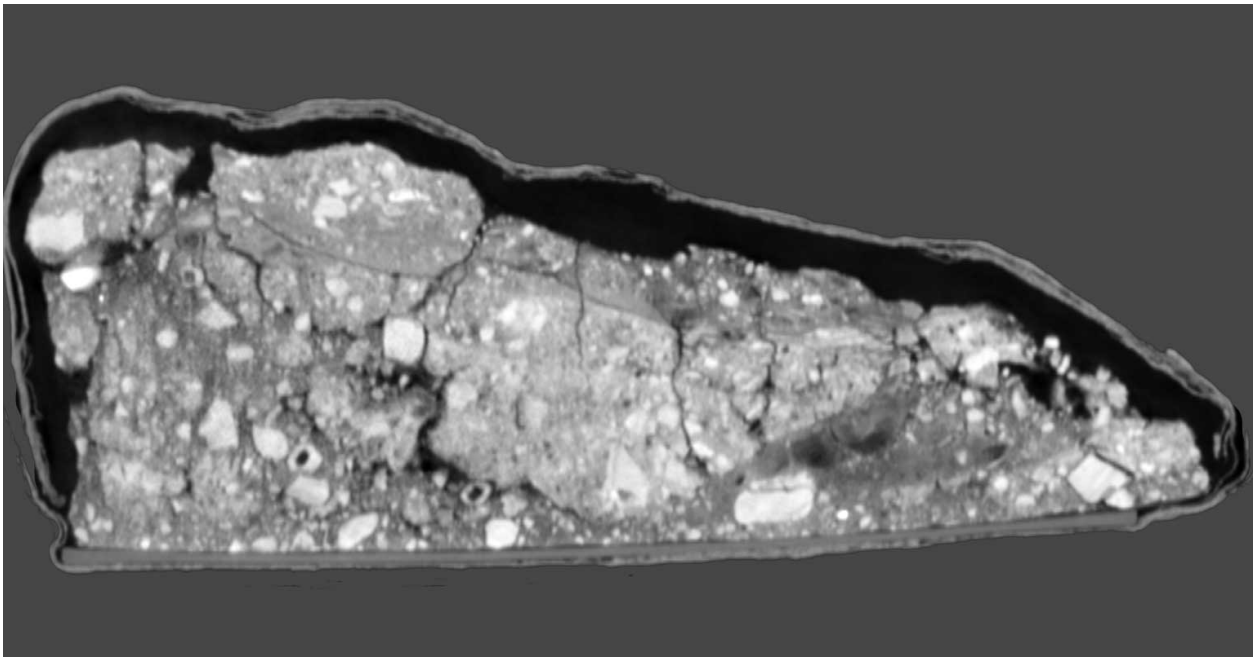

Supplementary Figure S19. Hill Antechamber feature after jacketing of largest block (U.W. 101-2076) in six layers of plaster bandages, prior to separation from sediment at its base.

Supplementary Figure S20. Fossil mass within plaster jacket after packing into waterproof caving bag for exit from the cave system.

Supplementary Figure S21. Detail of medical-resolution CT image of Hill Antechamber feature. This is a horizontal section with north at bottom of frame and west at right of frame. In this image, the bright object at lower left is a cross section of HAA1. At its left, cross sections of four rays of the articulated hand are visible; there is also a bone visible in the gap or space adjacent to the artifact that is a fragment of intermediate phalanx.

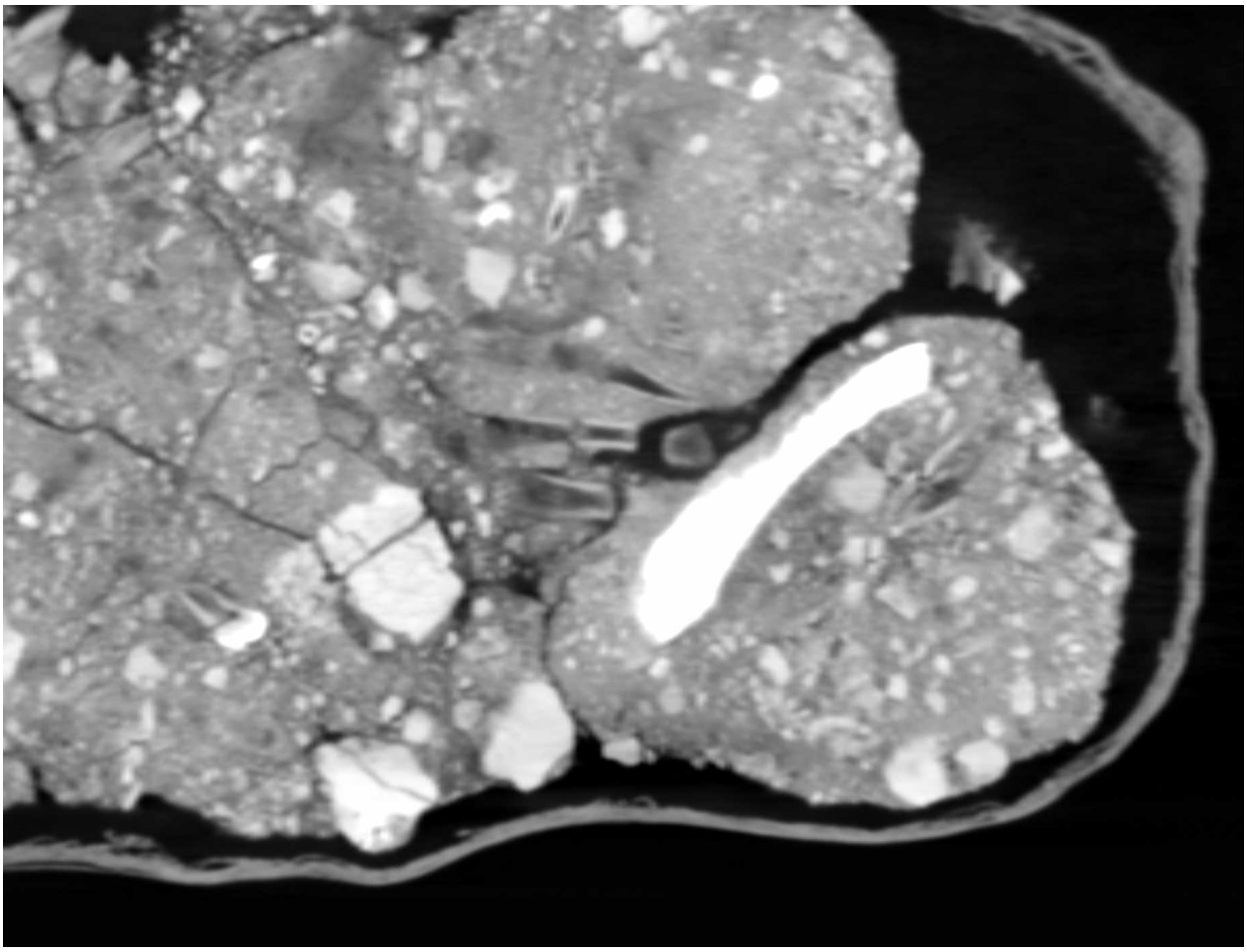

Supplementary Figure S22. 2013-2014 Dinaledi Chamber excavation area in (A) photo and the combination of white-light surface scans (B) and high-resolution laser scans (C) used to collect 3D data on the location of specimens excavated from the original Dinaledi assemblage. 3D data plotted as (D) X- and (E) Y-axis profiles of identified specimens including the articulated hand and foot.

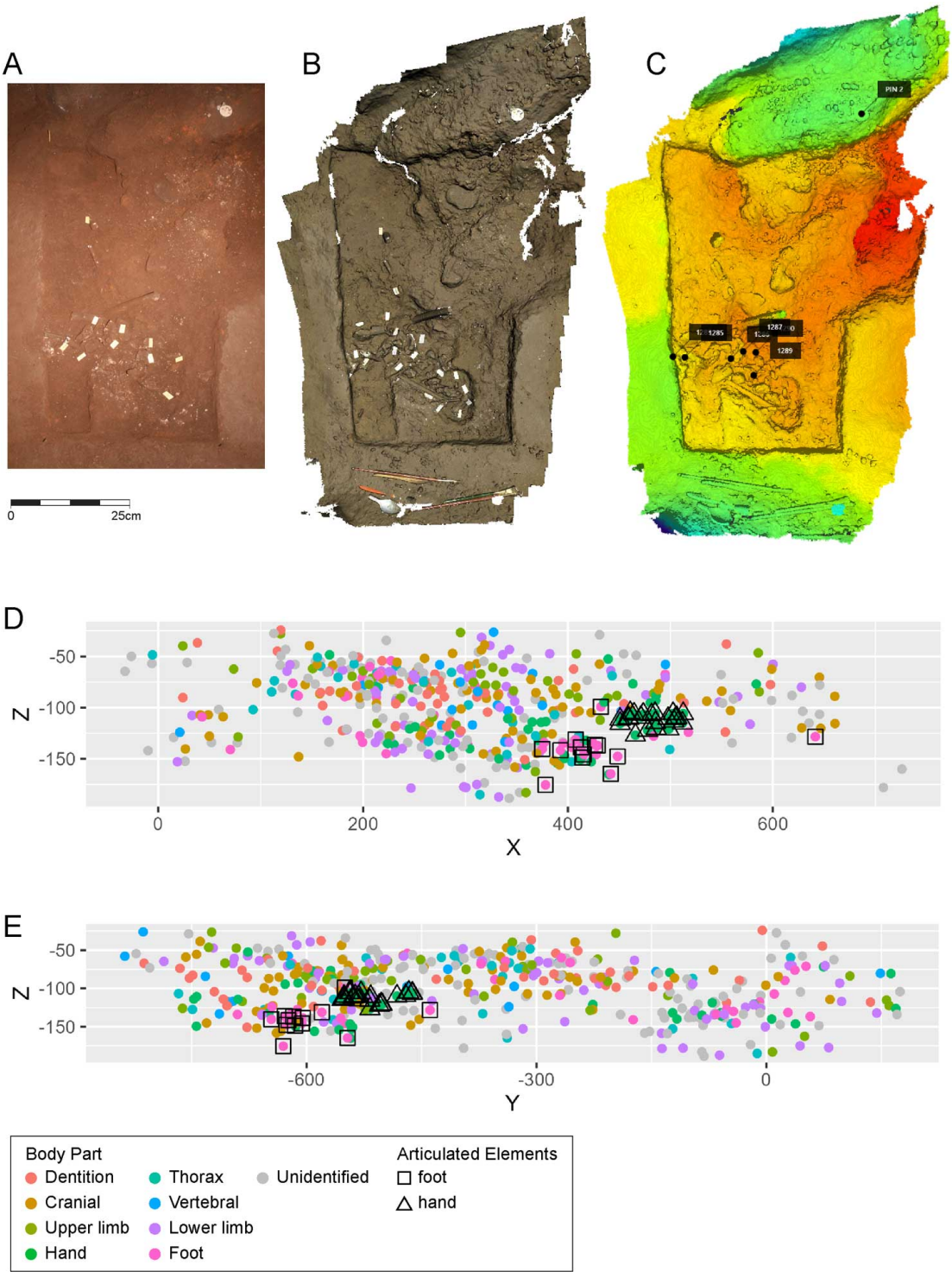

285

Supplementary Figure S23. Sediment profile showing east wall of N100W50 excavation unit in Hill Antechamber. The sediment is a dark brown unlithified breccia containing laminated orange-red mud (LORM) clasts. In this unit, the clasts make up a small fraction of the sedimentary deposit with little evidence of layering or stratigraphic differentiation.

Supplementary Figure S24. Hill Antechamber excavation east wall profile. North is at left of frame. The ellipse is drawn around a 15 cm by 10 cm by 5 cm collapse of the wall that accompanied removal of the plaster jacketed block, resulting in some distortion to the profile in this localized area. The darker patch at the right side of the ellipse is a shadow from the collapse edge, not a dark-colored inclusion in the sediment. Layering of the unlithified mud clast breccia is visible with some layers having a higher content of LORM clasts and laminae, with color variation less evident here than in the section shown in Figure S22. The layering is approximately parallel to the slope of the chamber floor. LORM content and clasts are less toward the north edge of the excavation, at left of frame.

Supplementary Figure S25. Stratigraphic profile of sediments directly adjacent to south boundary of Hill Antechamber feature. At left of image is the west side of the unit. This profile represents the sedimentary structure of the S50W100 and S50W50 units before the excavation reduced the feature to its rounded south edge. Horizontal layering of unlithified mud clast breccia (UMCB) with denser orange-red LORM-clast bearing laminae is evident for the top 10 cm of the profile. This layering becomes subhorizontal with horizontal depth with an east-west trending slope. The lowest layer visible trends into the horizontal floor of the excavation unit. This layering is not paralleled by the skeletal material, fill, or LORM clasts visible within the feature itself.

Supplementary Figure S26. Rendering of overall CT segmentation of Hill Antechamber feature. (A) View from west side; (B) view from north side; (C) view from overhead with elements labeled.

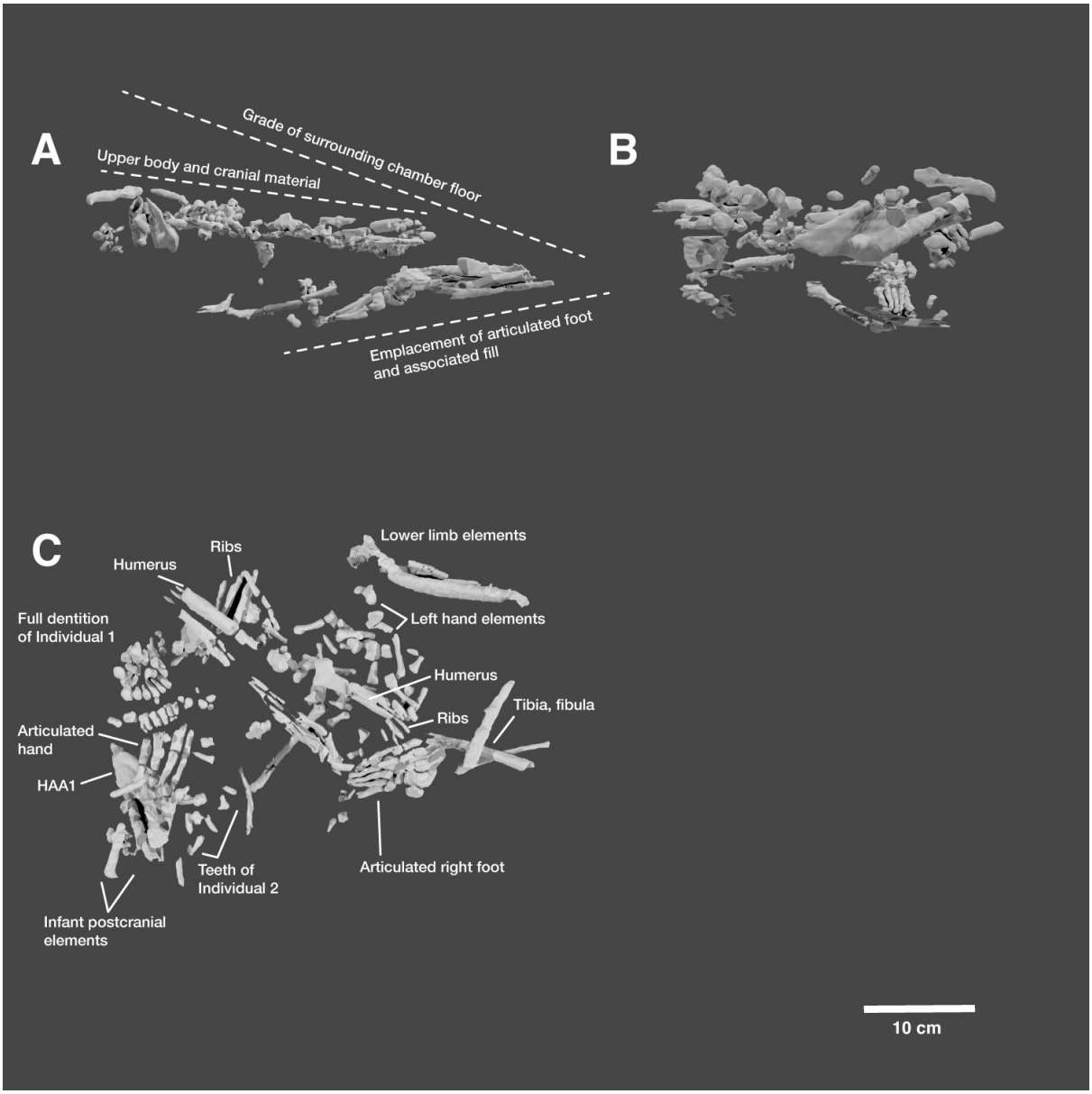

Supplementary Figure S27. CT section of Hill Antechamber feature. This east-west transverse section is at approximately 50% of north-south length of the feature. At the bottom of the section, many small LORM clasts are visible, with two notable voids taking the form of vertical cracks. The disordered array of LORM clasts continues to the right of image with frequent voids (west side of feature).

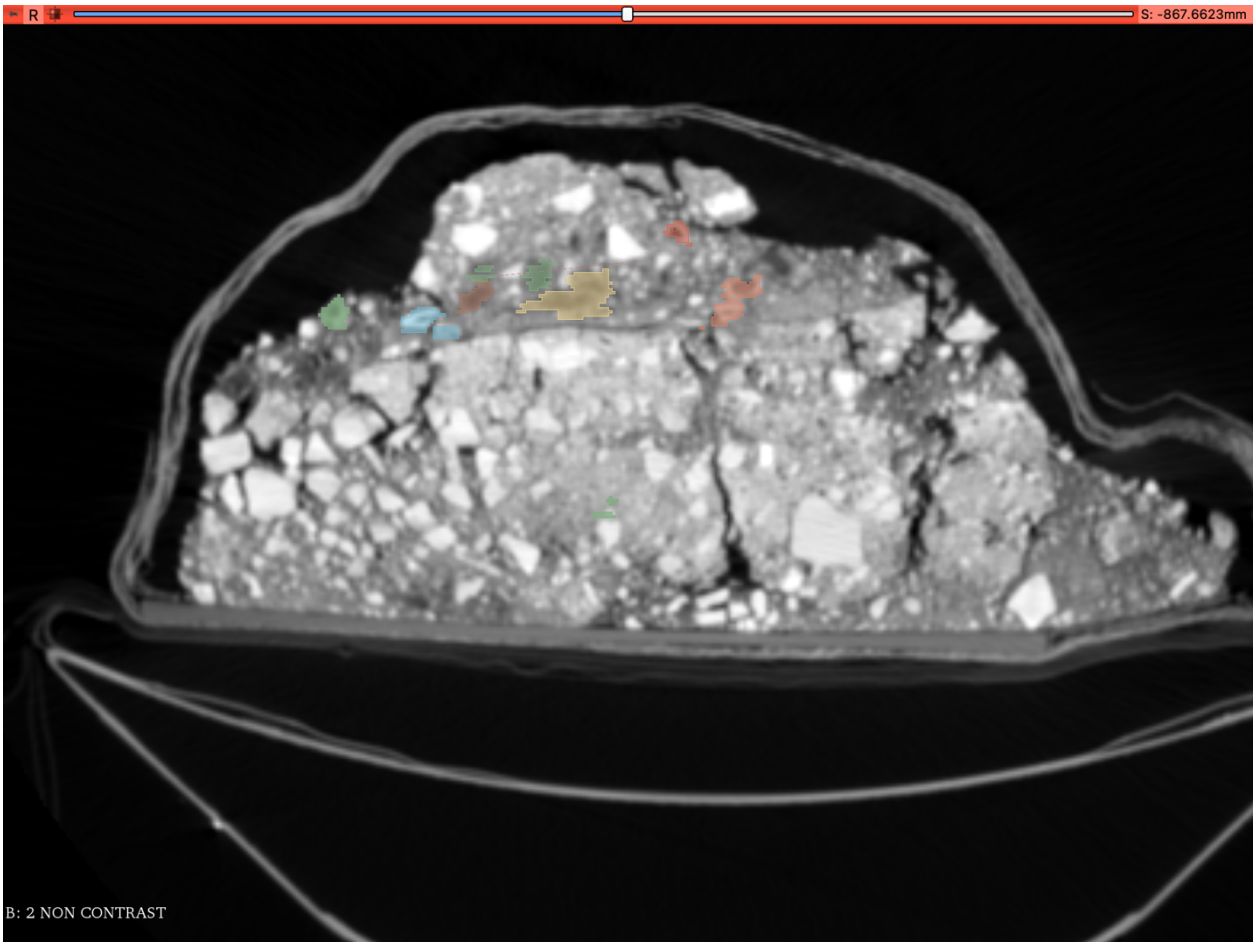

Supplementary Figure S28. Identifiable dental elements within the Hill Antechamber Feature. This view is oriented from below the feature to maximize the occlusal details of teeth other than the associated maxillary dentition of Individual 1, at top right. Enamel and dentin exhibit high contrast within the CT data. The 3D surface models generated from segmentation are the result of a smoothing algorithm after voxel selection. While this smoothing assists in visualization and identification in many cases, it creates some distortion in other cases. This resolution does not make it possible to identify all elements without ambiguity. For the teeth attributed to Individual 1, the presence of occlusal ordering within the maxilla and mandibular fragments enables a clear assignment of nearly all elements. For the teeth inferred to belong to Individuals 2 and 3 the present data leave ambiguity about the identity of some of the elements.

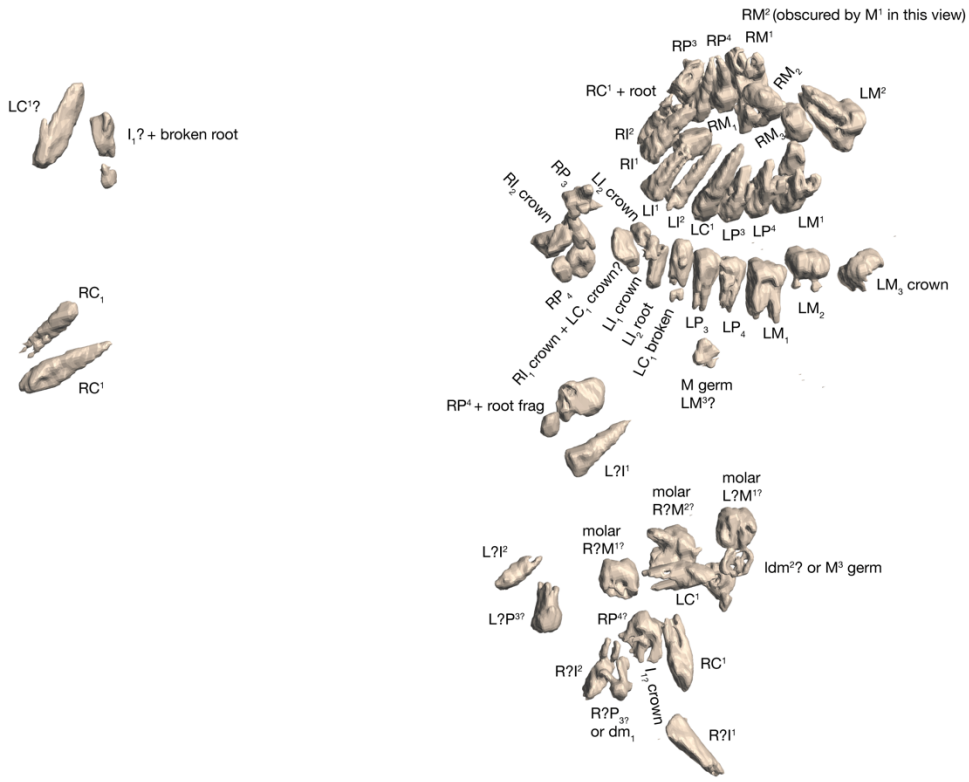

Supplementary Figure S29. CT section of Hill Antechamber feature. This is a transverse section on the east-west plane at approximately 65% of the north-south length. The five rays of the articulated foot are visible at lower left of the section. This section cuts across the metatarsals. The bones of the foot are immediately surrounded by a halo of sediment that approximates the shape of the foot's soft tissue. This lower-density sediment separates the bones of the foot from surrounding, more radio-opaque LORM clasts and sediment. Above the foot some small voids in the sediment are visible; small voids are also visible toward the left of this section directly above a disordered arrangement of LORM clasts.

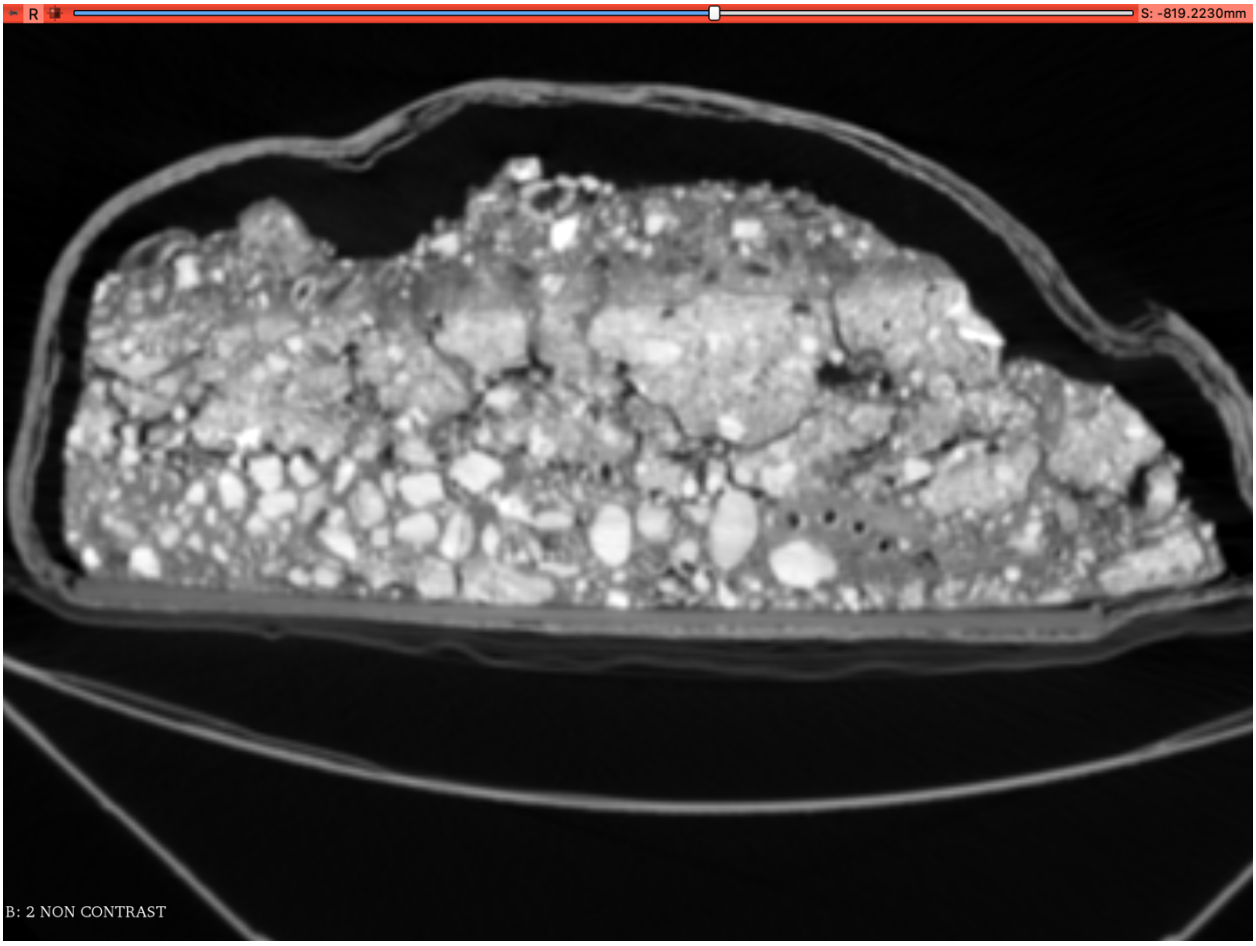

Supplementary Figure S30. Bright orange LORM patch immediately beneath Hill Antechamber feature. (A) Bottom of Hill Antechamber feature after jacketed extraction and inversion. The bright orange patch is visible centrally slightly toward the right (west) side of the inverted feature (B) Excavation unit immediately after jacketed extraction of feature and cleaning of surface. The corresponding orange patch is visible at center of unit.